ELECTROMAGNETIC IMAGING

by

Michel M. Ney

A thesis
presented to the School of Graduate Studies and Research
in partial fulfillment of the
requirements for the degree of
Doctor of Philosophy
in the
Department of Electrical Engineering

OTTAWA, Ontario, 1983
Michel M. Ney, 1983

UNIVERSITÉ D'OTTAWA
UNIVERSITY OF OTTAWA

It is by logic that we prove, but by intuition that we discover.

- Henri Poincaré (1854-1912)

AKNOWLEDGEMENTS

The author wishes to express his sincere gratitude to his thesis advisor Dr. S.S. Stuchly, for his guidance and valuable discussions held throughout this work. My sincere thanks also to Dr. A.M. Smith and Dr. M. Goldberg for their encouragement and fruitful discussions.

I wish also to express my profound gratitude, to my colleagues and graduate students who contributed to my work, for their valuable comments and discussions. Thanks are also due to all the staff of the Department of Electrical Engineering for their gracious assistance.

Finally, I wish to thank my wife Christiane and our little daughter Olivia for their patience during weekends and long evening hours while I was writing this thesis instead of being with them.

ABSTRACT

An alternative approach to the inverse scattering problem as applied to electromagnetic imaging is proposed.

An algorithm, based on the method of moments for reconstruction of the permittivity distribution of infinite cylinders with arbitrary cross-section, from scattered field measurements is derived. Computer simulations show that the problem is ill-conditioned and therefore highly noise sensitive.

A new alternative method using the pseudoinverse transformation in conjunction with image filtering techniques is presented. Computer simulations demonstrate that this technique yields good results especially in the case of slowly varying permittivity distributions.

GLOSSARY

List of symbols

Upper case		Introduced in page
$[C]$	Matrix NxN pertaining to the sampling geometry of the scatterer cross-section	29
D_j	j-th component of the [d] vector representing the polarization current density in the j-th cell (within the multiplicative factor $j\omega\varepsilon_0$)	28
E^i	Electric field z-component of the incident wave	12
E_j^i	j-th component of the vector $[e^i]$ representing the incident wave field value in the j-th cell	23
E^s	Electric field z-component of the scattered field	13
E_j^s	j-th component of the vector $[e^s]$ representing the scattered field value at the j-th observation point (detector)	26
E^t	Total electric field z-component	13
E_j^t	Total electric field unit pulse function at the position of the j-th cell	22
$H_0^{(2)}$	Hankel function of second kind and order zero	14

$H_1^{(2)}$	Hankel function of second kind and order one	25
I	Polarization filament current flowing along the cylinder axis	14
J_1	Bessel function of first order	25
L	Linear operator	17
[L]	Matrix of the operator in the moment method	18
N	Number of subareas into which the scatterer cross-section is divided	27
N_d	Number of detectors (observation points)	70
N_i	Number of column vectors of the matrix [T] which are taken as independent	62
P	Polarization current density z-component	15
S	Surface of the cylinder cross-section	15
S_e^{ε}	Signal-to-error ratio in the reconstruction expressed in dB	38
S_e^s	Signal-to-error ratio for the reconstructed scattered field relative to the noisy input data (measured values), expressed in dB	40
$\bar{S}_e^s$	Signal-to-error ratio for the reconstructed scattered field relative to the noiseless scattered field values expressed in dB	40
S_n^s	Signal-to-noise ratio in the measurements expressed in dB	38
T	Transformation from the space of vector [d] to the space of vector $[e^s]$	51
[T]	Matrix representing the transformation T	29
$\tilde{T}$	Adjoint of T	51
$[\tilde{T}]$	Matrix representing $\tilde{T}$	51
$T^{\dagger}$	Pseudoinverse operator	56
$[T]^{\dagger}$	Pseudoinverse of the matrix [T]	50

Lower case

a_j	Equivalent radius of the j-th cell of the sampled scatterer cross-section	25
b_j	Largest dimension of the j-th cell of the sampled scatterer cross-section	31
c_{ij}	Element of the matrix [C].	29
d	Distance of the detector array from the origin of the coordinate system	37
$[d]$	Polarization current density vector (within the multiplicative constant $j\omega\varepsilon_0$)	29
$[\hat{d}]$	Estimate of the vector [d]	46
$[d]_N$	Projection of [d] on nullspace(T)	55
$[d]_R$	Projection of [d] on range($\tilde{T}$)	55
$\Vert[\bar{d}]\Vert$	Norm of [d] relative to the noiseless solution	64
$[d]_s$	Smallest least-error solution generated by the pseudoinverse of [T]	54
$[e^i]$	Incident wave field vector	30
$[e^s]$	Scattered field vector	29
$[e^s]_p$	Projection of $[e^s]$ onto range(T)	53
f_j	Basis function in the moment method	17
f,g	Complex functions	17,18
h	Dimension of the cells in the y-direction	71
i,j	Subscripts	17,18
j	$\sqrt{-1}$	15
k	Wave factor or propagation constant	31
k_0	Wave factor in vacuum	14
l_{ij}	Element of the matrix [L]	20

m	Subscript	26
$[n]$	Noise vector	46
nl	Relative noise level with respect to incident wave amplitude	40
s	Spacing between detectors (observation points)	37
t_j	Vector formed by the j-th column of the matrix [T]	52
t_{ij}	Element of the matrix [T]	29
u	Input function in deterministic problems	17
u_j	j-th component of the input vector [u]	20
$[u]$	Input vector in the moment method	18
w_j	Weighting function	18
x,y,z	Cartesien coordinates	12,13

<u>Greek</u>

α_j	Coefficients of basis functions	17
$[\alpha]$	Vector of basis function coefficients	19
ΔS_j	j-th subarea of the cylinder cross-section	23
ε	Relative permittivity of the medium	15
ε'	Real part of the relative permittivity or dielectric constant	102
ε''	Relative loss factor of the medium corresponding to the imaginary part (minus sign) of ε	103
ε_j	Component of the vector $[\varepsilon]$ representing the permittivity value within the j-th cell	23
$[\varepsilon]$	permittivity vector	30
ε_0	Permittivity of vacuum	14

λ_0	Wavelength in vacuum	14
μ_0	Magnetic permeability of vacuum	102
ρ	Distance between observation points and cell location	14
σ	Conductivity of the medium	102
ω	Angular velocity	14

Miscellaneous

$C^{N\times 1}$	Nx1 complex matrix space	51
$R^{3\times 1}$	3x1 real matrix space	53
V, W, X, Y	General spaces	51,57
$[0]$	Zero vector	52
$\oplus$	Direct sum	58
$\overset{\perp}{\oplus}$	Orthogonal direct sum	55
$\Vert\ \Vert$	Norm	47
$<\ ,\ >$	Scalar inner product	18
$[\ ]^{-1}$	Matrix inversion	19
$[\ ]^{T}$	Matrix transposition	19
$*$	Complex conjuguate	18

CONTENTS

LIST OF FIGURES

LIST OF TABLES

Chapter I

INTRODUCTION

The ability to view internal structures nondestructively has long been a goal in many disciplines. Rapid advances toward this goal have been achieved in medicine with a technique known as Computerized Axial Tomography (CAT) [1]. The basic idea of this method is to reconstruct a two-dimensional image of a slice of an object from projections at different angles. Projections can be obtained with various types of radiation. In medicine, X-rays are most commonly used. Many X-ray CAT scanner machines are presently in operation and have demonstrated their usefulness as powerful diagnostic tools. The reconstructed image represents the attenuation properties (density) of the various tissues in the body. Emission Computerized Tomography (ECT) [2] utilizes γ-ray photon or positron emissions from radioisotopes which are administrated to the patient either by inhalation or by injection. The cross-sectional image yields information about the radioactive isotope distribution within the body. Intensive work is being carried out on applications of ultrasound in tomography [3,4,5]. In medical applications ultrasound creates less potential hazard to the patient and the reconstructed image yields information about acoustic properties of the tissues and may provide additional information for clinical diagnostics. Electromagnetic waves are used in geophysics to image geological structures from their propagation velocities or attenuation characteristics [6].

Reconstruction algorithms generally used in tomography are based upon the assumption of nearly straight-line propagation [7,8]. However, in the case of ultrasound and electromagnetic waves, this assumption is generally not valid. Rays undergo refraction at interfaces between media with different refractive indices. Furthermore, variations in the refractive index within the tissue result in significant ray bending. A further level of complexity, in the case of electromagnetic imaging, results from relatively long wavelengths which are employed in order to obtain adequate levels of transmission [9].

1.1 ELECTROMAGNETIC IMAGING : A REVIEW

Electromagnetic imaging refers to any noninvasive technique which allows visualization of certain parameters inherent to electric properties of the internal structure of an object, by using wave irradiations whose wavelength is of the order of magnitude of the size of the object under test.

Detection of buried objects received some attention in the past. Lytle et al. [10] attempted to locate buried mine shafts by lowering a radiofrequency (RF) source into a borehole, and a detector into another one, and by using the cross-borehole transmission data to reconstruct the conductivity distribution of the medium which was known to contain a tunnel. By selecting a proper frequency and analyzing the diffraction patterns at the receiving end, they were able to locate the tunnel. Microwave holography was also used to image buried dielectric anomalies [11]. The ground was scanned perpendicularly to the surface. An hologram was computed from the phase and intensity of waves back-scattered by the medium containing the buried object. Surface-reflected-wave components were estimated and subtracted from the original data. Satisfactory results were obtained with simple buried structures. One of the first attempts to use reconstruction algorithms used in X-ray tomography was proposed for imaging geological structures [6]. Linear arrays of transmitters and detectors were placed in two boreholes separated by a distance of several wavelengths. Straight-line propagation was assumed. Simulated reconstructions showed that ray-bending corrections were required to obtain accurate reconstructions.

In recent years, there has been a growing interest in using electromagnetic waves for medical imaging. It is generally recognized that electromagnetic imaging has several potential advantages over other imaging techniques. Of particiliar interest is the superior contrast of the electomagnetic medical diagnostic techniques, especially in applications involving organs such as lungs, where ultrasound is highly attenuated (due to the presence of air) and X-ray techniques have very low contrast. Many parameters can be imaged with electromagnetic waves such as attenuation, conductivity and dielectric constant. These parameters are generally frequency dependent and imaging over a wide range of frequencies may be possible with electromagnetic sources, to obtain more information for clinical diagnostics. Finally, continuous real-time monitoring is potentially feasible since, at the required level of radiation, electromagnetic waves are not known to represent a hazard to the patient.

Unfortunately, electromagnetic imaging is still in its preliminary stage basically because of the difficulties in developing adequate reconstruction algorithms. These difficulties occur because the paths between transmitters and receivers are object dependent, which reveals the effect of diffraction. In addition, practical difficulties arise when fields are measured because of reflections from the surroundings. Finally, reducing coupling effects between detectors and the scatterer is generally difficult. Henderson and Webster [12] designed an impedance camera to generate electrical impedance images of the thorax. One hundred spatially specific admittance measurements per frame were recorded at rates up to 32 frames per second. Data were presented in a form of isoadmittance contour maps. Difficulties arose in correlating images with lung pathologies, owing to the poor resolution of the system. Electrical Impedance Computed Tomography was proposed by several authors [13,14]. A transaxial image representing the conductivity of tissues was attempted. Reconstruction algorithms utilized in X-ray tomography were applied. In general, results turned out to be unsuccessful because current stream-lines cannot usually be forced to be straight and parallel. Gregg [16] used Algebraic Reconstruction Techniques (ART) [7] to reconstruct cross-sectional distributions of the attenuation of various objects from 10-GHz microwave transmission data. Artifacts due to scattering are clearly visible in the final reconstruction. Larsen and Jacobi [17] performed microwave imaging of a canine kidney. The organ was immersed in water to match the properties of the surrounding medium to that of the object. A scan of 64x64 sample points was performed by moving transmitting and receiving antennas correspondingly. Relative phases and amplitudes of the transmitted waves at 3.9 GHz were recorded. Images whose gray level is proportional to the relative phase or amplitude showed many artifacts due to diffraction effects.

1.2 ELECTROMAGNETIC IMAGING : DIFFRACTION EFFECTS

Despite the fact that many results indicate that diffraction effects cannot be generally neglected, many authors [18,19,20] are still proposing linear reconstruction algorithms for electromagnetic imaging. In reality, the measured transmitted or reflected waves are no longer projections, but are scattered waves generated by the object superimposed on the incident field. Consequently, the reconstruction of the electrical parameter distribution of an object, using electromagnetic waves, should rather be considered as an inverse scattering problem and this topic is addressed in this thesis.

Perturbation methods [21] were proposed in acoustic tomography to reconstruct the velocity distribution of a small disturbance from complex data taken at different observation angles. It was one of the first attempts to include diffraction effects in algorithms applied to tomography. Adams and Anderson [22] used a technique of reconstructing a three-dimensional image of an object from complex microwave field data taken in three different planes. Experimental results of independent, non-coupled point scatterers at 32 GHz are reported. It was found that when the scatterers were closely spaced or when the viewing directions were not properly chosen (which requires some a priori knowledge of the object), severe artifacts were present.

Although intensive investigations are being carried out in inverse scattering theory, very few solutions have been reported for dielectric scatterers. Among theoretical works, Borjarski [23] derived an integral equation for unknown fields and sources in the interior of a closed surface on which remotely sensed fields are known. An analytic closed form solution of this integral equation was obtained using a modified Fourier transform. Stone [24] used a similar approach to determine the scattered-field source[1] distribution by measuring fields and their normal derivative on a surface enclosing the scatterer.

There is a controversy about the uniqueness of the solution in inverse source problems. Some authors [25,26], claim that the solution of that problem is not unique due to the fact that there exist nonradiating sources [27] that do not radiate outside the volume in which they are confined. Although these sources are not physically realizable and do not satisfy the minimum energy principle [28], they however mathematically exist and it is not possible to find a unique solution to the inverse source problem if some constraints are not enforced on the sought solution. The nonuniqueness of the inverse source solution is clearly demonstrated for few simple cases in [29]. It is mentioned that the ambiguity can be alleviated by taking measurements at different angles

[1]Sources in scattering theory refer to currents (either polarization or conduction currents) induced inside an object by irradiation or other means, which generate scattered fields.

of irradiation or when some a priori information about the scatterer is available. The problem of nonuniqueness is analyzed in some detail in Sections 2.4 and 3.3.

An early theoretical attempt to reconstruct the dielectric distribution using holography was proposed by Wolf [30]. Holograms of a weakly-scattering semi-transparent object were taken at different angles of irradiation. It was shown that the three-dimensional Fourier transform of the complex dielectric distribution of the object can be approximately determined from the two-dimensional Fourier components of the scattered fields in two well specified planes. The scattered fields were determined from the holograms. It was suggested that the limit of resolution to which the details of the unknown structure could be determined, was about half a wavelength of the irradiating wave. A technique using microwave holography was presented in [31,32] for visualization of internal structures within a dielectric. The object was irradiated with microwaves and the object was reconstructed from its microwave hologram optically. Many artifacts appeared in the reconstructed image.

In a recent work [33], an iterative technique was proposed for one-dimensional dielectric distributions within infinite slabs. The constitutive parameters of a lossy dielectric slab were computed from the diffracted field, when irradiated by a sine-squared-impulse-like wave, in the time domain. The unknown parameters were iteratively determined by solving a space-time discretized field integral equation for direct and inverse scattering problems. Both problems yielded a system of linear equations that were solved in each iteration loop. The order of the systems was equal to the number of intervals into which the slab was divided. Results showed good-fidelity reconstructions for various dielectric profiles[1] for noiseless input data. A multi-projection technique was presented in [34] for reconstruction of various objects using an algorithm similar to the one utilized in X-ray tomography. The object was assumed to be weakly-scattering so that the Born approximation could be used in the analysis i.e. the object could be represented by an ensemble of independent scatterers. A microwave source irradiated the object at various angles of incidence. At each angle, the magnitude and phase of the scattered field on an observation plane located behind the object were recorded. A back-projection method using the deconvolution technique with inverse diffraction filtering was applied to reconstruct the object. The results showed that for the two-dimensional case a resolution of half a wavelength could be achieved although artifacts indicated that the assumption of independent scatterers was not accurate. A similar technique was used by Bolomey et al. [35] to image

[1]The term dielectric profile is used when a one-dimensional dielectric distribution is under consideration.

the polarization current amplitude of two-dimensional dielectric bodies. The reconstructed image depended on both the observation and the incident wave. Consequently, in order to obtain useful information in the reconstructed image it was necessary to assume the field as uniform as possible in the scatterer location.

1.3 MOTIVATION

Through the above sections it is shown that long-wave imaging is an inverse scattering problem. The approach presented in this work makes use of a formidable tool which has been used with great success to solve many electromagnetic problems namely the method of moments. This powerful method can be used to solve numerically integro-differential equations which are frequently encountered in electromagnetic theory. The method yields a system of linear equations that can be solved using modern digital computers by means of appropriate algorithms. The level of difficulty in this work is reduced by considering only one- and two-dimensional cases. One of the attractive features of the method described in the next chapter is that it can be extended to three-dimensional dielectric distributions . A motivation to attack the case of infinite cylinders is that experimental verification of the algorithm can be performed in a controlled environment such as a parallel-plate chamber [9]. This configuration makes finite-length objects appear electrically infinitely long and the transverse electromagnetic (TEM) mode can easily be generated in such a structure.

Chapter II

THEORY

First, the derivation of the integral equations pertaining to the problem of the field diffracted by infinitely long cylinders with arbitrary cross-section is presented. Then a brief description of the moment method is given and its application in the framework of the scattering of infinitely long dielectric cylinders is described. A new algorithm for reconstructing the dielectric distribution of infinite cylinders is presented as a solution of an inverse scattering problem. The difficulty regarding the uniqueness of the solution of the inverse scattering problem is also discussed.

2.1 SCATTERING THEORY

Let an incident wave, with an electric field $E^i(x,y)$[1], irradiate an infinitely long dielectric cylinder[2] with arbitrary cross-section. The only limitation about the incident wave is that the electric field is polarized along

---

[1]The time-factor $\exp(j\omega t)$ is understood.

[2]Cylinder always refers to infinitely long structures with arbitrary cross-section throughout the discussion.

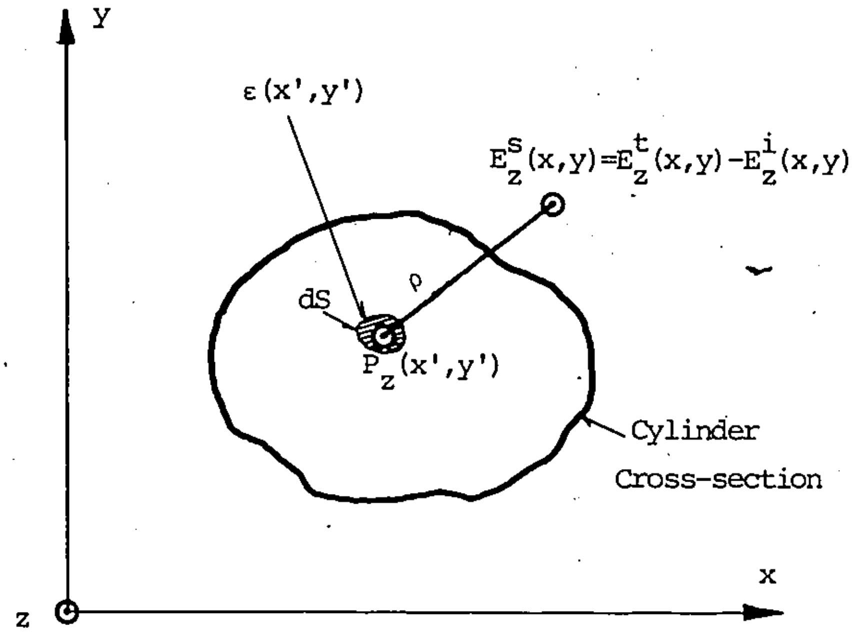

Figure 1: Geometry pertaining to the scattered field produced by dielectric cylinders.

The figure depicts the top view of the cylinder cross-section irradiated by an arbitrary wave whose electric field is polarized along the cylinder axis. The medium surrounding the cylinder has the permittivity of vacuum.

the cylinder axis and does not depend upon the z-coordinate (see Fig. 1). The dielectric scatterer may be lossy[1], but its permittivity is a function of x,y-coordinates only. Because of symmetry, the total field $E^t(x,y)$ and the scattered field $E^s(x,y)$ do not depend on the z-coordinate and are also polarized along the z-axis i.e. along the cylinder axis. The total field at any point can be

[1]However, the medium is assumed to be linear and isotropic.

expressed by[2] :

$$E^t(x,y)=E^s(x,y)+E^i(x,y) \quad . \tag{2.1}$$

The field produced by an elementary electric current filament dI directed along the z-direction in free-space, is given by the following cylindrical wave function [36] :

$$dE = -(k_0^2 dI/4\omega\varepsilon_0)H_0^{(2)}(k_0\rho) \quad , \tag{2.2}$$

where

$$\rho = \sqrt{(x-x')^2+(y-y')^2} \quad ,$$

$H_0^{(2)}$ is the Hankel function of the second kind of order zero, ρ, is the distance from the current filament to the observation point, $k_0=2\pi/\lambda_0$ where λ_0 is the free-space wavelength, ω is the angular frequency of the signal and ε_0 is the permittivity of vacuum.

The filament current dI bears a volume current density P such that :

$$dI=PdS \quad , \tag{2.3}$$

where dS is the infinitesimal cross-section area of the filament current. The volume current density P is called the polarization current density and is related to the total

[2]The subscript z is omitted.

field E^t inside the filament by :

$$P=j\omega\varepsilon_0(\varepsilon-1)E^t \quad , \tag{2.4}$$

where ε is the relative permittivity of the medium in which P is flowing and $j=\sqrt{-1}$. A cylinder irradiated under the conditions previously stated can be seen as a distribution of current filaments directed along its axis and whose cross-section infinitesimal area dS produces an infinitesimal increment in the radiated scattered field which, according to (2.2),(2.3) and (2.4), is given by :

$$dE^s=-(jk_0^2/4)(\varepsilon-1)E^tH_0^{(2)}(k_0\rho)dS \ . \tag{2.5}$$

To determine the total scattered field at any point in the surrounding space, (2.5) is integrated throughout the cross-section of the cylinder :

$$E^s(x,y)=-jk_0^2/4\iint_S[\varepsilon(x',y')-1]E^t(x',y')H_0^{(2)}(k_0\rho)dx'dy' \ , \tag{2.6}$$

where S is the cross-section of the cylinder. It should be kept in mind that the term $j(\varepsilon-1)E^t$ is proportional (within a multiplicative constant $\omega\varepsilon_0$) to the polarization current density P given by (2.4). Therefore (2.6) can be written as :

$$E^s(x,y)=-k_0^2/4\omega\varepsilon_0 \iint_S P(x',y')H_0^{(2)}(k_0\rho)dx'dy' \quad . \qquad (2.7)$$

From (2.6) and (2.7) it is evident that the integration pertains to the primed variables regarding the coordinates of the polarization current density (source of the scattered fields), which is identically zero outside the cylinder cross-section since it is assumed that the medium outside the cylinder has dielectric constant equal to 1. To perform the integration (2.7) one must first determine P, which cannot generally be probed since it flows inside the cylinder. One way to compute the polarization current density is to apply (2.6) over the cylinder cross-section which with (2.1) yields :

$$E^t(x,y)+jk_0^2/4\iint_S[\varepsilon(x',y')-1]E^t(x',y')H_0^{(2)}(k_0\rho)dx'dy' = E^i(x,y) \quad . \qquad (2.8)$$

The integral equation (2.8) can be solved by numerical techniques. A numerical method which is used in this work is called the method of moments and is described in the next section. Once the current density is computed, the scattered field can be determined at ANY POINT outside the scatterer using (2.7).

2.2 THE METHOD OF MOMENTS

Consider the following inhomogeneous equation corresponding to a deterministic problem :

$$L(f)=u \quad , \tag{2.9}$$

where L is any linear operator (such as integrator,differentiator,etc...), u is a known function and f is the function to be determined. The range of L is the space spanned by all functions u resulting from the operation. The set of all possible functions satisfying the boundary conditions accompanying the operator L is called the domain of L. The method of moments consists of transforming (2.9) into a set of linear equations that can be solved numerically.

Let the unknown function f be expanded in a series of BASIS FUNCTIONS or EXPANSION FUNCTIONS $f_1, f_2, \ldots, f_j, \ldots$ in the domain of L such that :

$$f= \sum_j \alpha_j f_j \quad , \tag{2.10}$$

where α_j are constants. For exact solutions, (2.10) may be a finite or infinite summation depending upon the choice of the f_j. In that case, the f_j form a complete set of basis functions. Using the linear property of the operator L and substituting (2.10) in (2.9) yields :

$$\sum_j \alpha_j L(f_j)=u \quad . \tag{2.11}$$

A suitable inner scalar product < , > is determined for a given problem satisfying :

$$\begin{aligned} &\langle f,u\rangle=\langle u,f\rangle^* \\ &\langle \alpha f+\beta u,g\rangle=\alpha\langle f,g\rangle+\beta\langle u,g\rangle \\ &\langle f^*,f\rangle >0 \quad \text{for } f \neq 0 \\ &\qquad\quad =0 \quad \text{for } f = 0 \quad , \end{aligned} \tag{2.12}$$

where α and β are scalars f,g,u any functions and * denotes the complex conjugate. A set of WEIGHTING or TESTING functions $w_1, w_2, \ldots, w_i, \ldots$ is chosen in the range of L. The inner product of (2.11) is taken for each w_i giving :

$$\sum_j \alpha_j \langle w_i, L(f_j)\rangle=\langle w_i, u\rangle \quad . \tag{2.13}$$

This produces a set of linear equations which can be written in a matrix form as :

$$[L][\alpha]=[u] \quad , \tag{2.14}$$

where

$$[L]=\begin{bmatrix} \langle w_1,L(f_1)\rangle & \langle w_1,L(f_2)\rangle & \cdots\cdots \\ \langle w_2,L(f_1)\rangle & \langle w_2,L(f_2)\rangle & \cdots\cdots \\ \cdots\cdots & \cdots\cdots & \cdots\cdots \end{bmatrix},$$

$$[\alpha]=[\alpha_1 \ \alpha_2 \ \cdots\cdots \alpha_j \cdots\cdots]^T$$

and

$$[u]=[\langle w_1,u\rangle \ \langle w_2,u\rangle \cdots\cdots \langle w_i,u\rangle \cdots\cdots]^T ,$$

where ^{T} indicates transposition. If the matrix [L] is nonsingular, its inverse $[L]^{-1}$ exists and the α_j are therefore given by :

$$[\alpha]=[L]^{-1}[u] \tag{2.15}$$

and the solution for f is found using (2.10).

There are infinitely many possible sets of basis functions and weighting functions. One of the main tasks in any particular problem is the selection of an appropriate set of w_j and f_j. They should be chosen to form sets of independent functions. Some additional factors may influence the selection, such as the accuracy of the solution desired, the size of the matrix that can be inverted and the realization of a well-behaved matrix [L]. Different schemes lead to various methods whose complete description can be found in [37].

Let $<f,u>$ be the inner product defined in the complex function space by :

$$<f,u>=\int_{\Omega} f^{*}u \; d\Omega', \tag{2.16}$$

where f and u are defined in the domain Ω . It is easy to prove that (2.16) satisfies the conditions (2.12). Thus the elements l_{ij} and u_i are given by :

$$\begin{aligned} <w_i,L(f_j)> &= \int_{\Omega} w_i^{*} L(f_j) d\Omega' \\ <w_i,u> &= \int_{\Lambda} w_i^{*} u \; d\Lambda'. \end{aligned} \tag{2.17}$$

The integrals involved in (2.17) are often difficult to evaluate even numerically. One way to reduce the amount of computation is to choose the w_i as a set of impulse or Dirac functions at different points of the region of interest. Therefore (2.17) can be solved in a trivial manner using the property of the Dirac function :

$$\begin{aligned} <w_i,L(f_j)> &= L[f_j(\vec{r}_i)] \\ <w_i,u> &= u(\vec{r}_i) \; , \end{aligned} \tag{2.18}$$

where $\vec{r}$ is the coordinate vector. One would obtain the same result by enforcing (2.11) at points of the region of interest. Using Dirac functions as testing functions is called the <u>point matching</u> or <u>collocation method</u>. Again the convergence of the solution depends on the choice of the set of basis functions. The accuracy of the solution is also sensitive to the points of match.

Another possibility is to select a finite set of basis functions f_j which are different from zero only over selected subsections of the domain of f. Hence, each coefficient α_j of the expansion (2.10) affects the approximation of the unknown function f only over a subsection of the region of interest. This is called the <u>subsection method</u>. Using this method does not generally yield an exact solution for f since few basis functions aproximate the unknown function over a given region. However, for sufficiently small subsections a reasonable degree of accuracy may be obtained. Care must be taken in choosing the basis functions. For instance, when differential operators are involved, they must be in the domain of these operators. In particular, if pulse functions are selected, they may not be in the domain of L and the operator must be extended or approximated [37]. However, for integral operators the use of pulse or triangle functions presents no such problem.

The method of subsections in conjunction with collocation further simplifies the evaluation of the matrix elements l_{ij} and u_j .

2.3 SOLUTION TO SCATTERING PROBLEMS USING THE MOMENT METHOD

By inspecting (2.8), it is relatively easy to make the incident field $E^i(x,y)$ correspond to the function u, the total field $E^t(x,y)$ to the unknown function f and the following expression :

$$E^t(x,y)+jk_0^2/4\iint_S[\varepsilon(x',y')-1]E^t(x',y')H_0^{(2)}(k_0\rho)dx'dy' \quad (2.19)$$

to the operation L(f). One must remember that the region of interest for the operator (2.19) is the cylinder cross-section S. To make use of the collocation method one chooses a set of Dirac functions defined at discrete points (x_i,y_i) throughout the cylinder cross-section. According to (2.18) and (2.19), the elements of [L] and [u] can be written as

$$l_{ij}=E_j^t(x_i,y_i)+jk_0^2/4\iint_S[\varepsilon(x',y')-1]E^t(x',y')H_0^{(2)}(k_0\rho_i)dx'dy' \quad (2.20)$$

$$u_i=E^i(x_i,y_i)$$

where

$$\rho_i=\sqrt{(x_i-x')^2+(y_i-y')^2}$$

and E_j^t are the basis functions. The integral (2.20) is often difficult to evaluate. Using the subsection method usually simplifies the evaluation of the matrix elements. Let us define a set of basis functions as follows :

$$\begin{aligned} E_j^t(x,y) &= 1 \qquad \text{within } \Delta S_j \\ &= 0 \qquad \text{elsewhere} \quad , \end{aligned} \tag{2.21}$$

where ΔS_j is a subarea of the cylinder cross-section containing a point of interest (x_j, y_j) (see Fig. 2). Thus by (2.10), the unknown function $E^t(x,y)$ is stepwise approximated.

The physical meaning of (2.21) is that the total electric field is assumed to be constant within ΔS_j. It is further assumed that the relative permittivity ε is also constant within ΔS_j. Consequently, from (2.4) the polarization current density is constant within each subarea. The above considerations permit one to write (2.20) as :

$$\begin{aligned} l_{ij} &= 1 + jk_0^2/4[\varepsilon_j - 1] \iint_{\Delta S_j} H_0^{(2)}(k_0\rho_i)dx'dy' \qquad \text{for } i=j \\ &= jk_0^2/4[\varepsilon_j - 1] \iint_{\Delta S_j} H_0^{(2)}(k_0\rho_i)dx'dy' \qquad \text{for } i \neq j \\ u_i &= E^i(x_i, y_i) = E_i^i \quad . \end{aligned} \tag{2.22}$$

The surface integral of the Hankel function can be evaluated using numerical methods. Care must be taken when the obervation point is inside ΔS_j in which case a

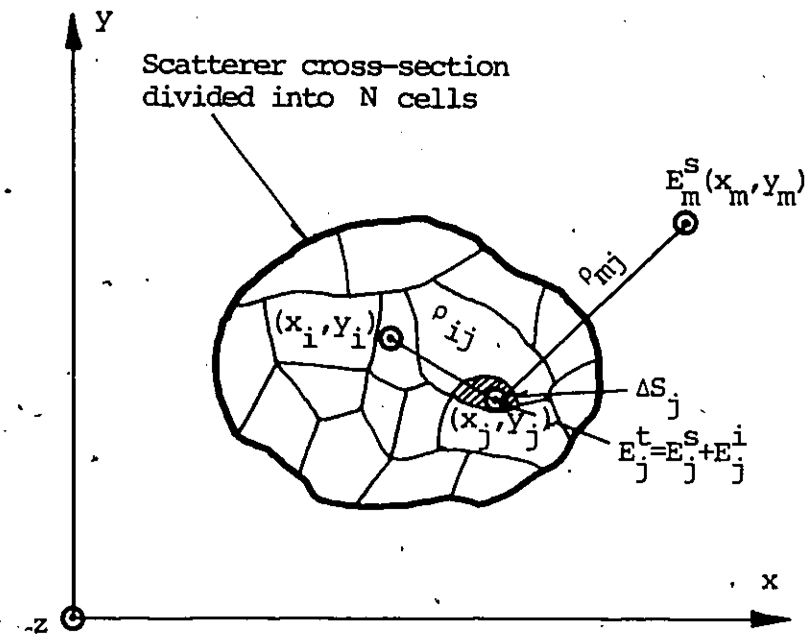

Figure 2: Geometry for subsectional bases of the cylinder cross-section.

The scatterer cross-section is divided into N subareas of arbitrary shape. The relative permittivity ε and the total field E^t are assumed to be constant within each subarea.

singularity occurs for $H_0^{(2)}$ when its argument is zero. However, a closed form solution can be obtained when the subareas ΔS_j are chosen to be circular and centered around the points (x_j, y_j) [38], for which (2.22) becomes :

$$l_{ij}=1+(\varepsilon_j-1)(j/2)[\pi k_0 a_j H_1^{(2)}(k_0 a_j)-2j] \quad \text{for } i=j$$

$$=(\varepsilon_j-1)(j\pi k_0 a_j/2)J_1(k_0 a_j)H_0^{(2)}(k_0\rho_{ij}) \quad \text{for } i\neq j \qquad (2.23)$$

$$u_i=E_i^i \quad ,$$

where :

$$\rho_{ij}=\sqrt{(x_i-x_j)^2+(y_i-y_j)^2}$$

J_1 is the Bessel function of first order, a_j is the radius of the circular subarea ΔS_j and $H_1^{(2)}$ is the Hankel function of the second kind of first order. The subscript i refers to the observation points within the cylinder cross-section at coordinates (x_i,y_i) and j to the subarea ΔS_j at coordinates (x_j,y_j). The total internal field E_j^t within each cell can be determined by solving the linear system (2.14) for α_j and then using (2.10). The latter expression indicates that each subarea representing the cross-section of a thin radiating cylinder cannot be taken as an independent scatterer since the polarization current density which flows into it is a linear combination of all other currents which exist elsewhere in the cylinder.

A similar reasoning applies to the scattered fields at observation points outside the cylinder cross-section. Suppose that the scattered fields $E^s(x,y)$ are known at certain points located outside the scatterer. Thus, by virtue of (2.6), the unknown function is also the total field within the cylinder and the operation L(f) is given by :

$$L(f)=-jk_0^2/4\iint_S[\varepsilon(x',y')-1]E^t(x',y')H_0^{(2)}(k_0\rho)dx'dy' \quad . \qquad (2.24)$$

Using the same reasoning as for observation points located within the cylinder cross-section, the operation (2.24) can be linearized and the matrix elements become :

$$l_{mj}=-(j\pi k_0 a_j/2)(\varepsilon_j-1)J_1(k_0 a_j)H_0^{(2)}(k_0\rho_{mj})$$

$$u_m=E_m^s \quad , \qquad (2.25)$$

where the subscript m refers to points outside the scatterer and j to the subarea ΔS_j within the scatterer. Therefore, once the total field within each subarea is computed, the scattered fields at points outside the scatterer are found using (2.14) with (2.25). The scattered field at any location outside the cylinder is shown as the linear combination of polarization currents in all subareas.

To summarize, the cylinder cross-section is first divided into a number N of subareas (cells) within which the total field, the relative permittivity and consequently the polarization current can be assumed constant. The total field within each cell is found using the matrix equation (2.14) whose elements are given by (2.23). The α_j are the coefficients of the step basis functions which approximate the total internal field. Then, the scattered field E_m^s at ANY POINT outside the scatterer can also be found from (2.14), with l_{mj} given by (2.25); which can be written as :

$$E_m^s = -j\pi k_0/2 \sum_{j=1}^{N} a_j(\varepsilon_j - 1)\alpha_j J_1(k_0 a_j) H_0^{(2)}(k_0 \rho_{mj}) \qquad (2.26)$$

where N indicates the number of cells into which the scatterer cross-section is divided.

It has been found numerically [38] that the result of the integrals in (2.22) does not vary significantly with the shape of the cell. For square cells for instance, a_j should be taken as the equivalent radius i.e. the square root of the subarea divided by π.

Richmond [38] has shown excellent results regarding computations of scattered fields produced by various structures. The accuracy of the solution increases with the number of cells, however the order of the matrix is equal to the number of cells N which may imply some computational difficulty for large scatterers.

2.4 ALGORITHM FOR DIELECTRIC DISTRIBUTION RECONSTRUCTION

The objective of this work is to image the dielectric distribution of cylinders from the diffracted field observed outside the cylinder. The quantity which is in fact measured is always the total field at points located outside the structure. Indeed, the incident field always superimposes upon scattered fields, consequently the latter cannot be probed directly and should be determined from (2.1) since the incident field (the field at any point in the space without scatterer) is known. The unknown quantities are the total electric field inside the scatterer, the relative permittivity and the polarization current density. Therefore three equations are required to determine these three unknowns. By inspection of the matrix equations involved in the solution of the direct scattering problem described in Section 2.3, it appears that a solution of the inverse scattering problem can be obtained by simple manipulations.

Let us first define the following quantity :

$$D_j = (\varepsilon_j - 1)\alpha_j \quad , \tag{2.27}$$

where α_j is the weighting coefficient of the total field inside the cell j. By virtue of (2.4), the quantity D_j is proportional (within the multiplicative constant $j\omega\varepsilon_0$) to the polarization current density in the cell j. Consider a number of observation points equal to the number of cells N into which the cylinder cross-section is divided. Consequently, writing (2.26) for each observation point yields a NxN-set of linear equations :

$$[T][d]=[e^s] \tag{2.28}$$

where

$$t_{mj}=-(j\pi k_0 a_j/2)J_1(k_0 a_j)H_0^{(2)}(k_0\rho_{mj}) \quad ,$$
$$[d]=[D_1\ D_2 \ldots . D_N]^T=[(\varepsilon_1-1)\alpha_1\ (\varepsilon_2-1)\alpha_2 \ldots (\varepsilon_N-1)\alpha_N]^T$$

and

$$[e^s]=[E_1^s\ E_2^s \ldots\ldots E_N^s]^T \quad .$$

Therefore, if the matrix $[T]^{-1}$ exists, the vector [d] can be computed as :

$$[d]=[T]^{-1}[e^s] \tag{2.29}$$

The matrix equation (2.14) which determines the total field within each cell can be written in terms of the vector [d] :

$$[\alpha]+[C][d]=[e^i] \tag{2.30}$$

where

$$c_{ij}=(j/2)[\pi k_0 a_j H_1^{(2)}(k_0 a_j)-2j] \qquad \text{for } i=j$$
$$=(j\pi k_0 a_j/2)J_1(k_0 a_j)H_0^{(2)}(k_0\rho_{ij}) \text{ for } i\neq j$$

and

$$[e^i]=[E_1^i\ E_2^i\ldots\ldots E_N^i]^T$$

Substituting (2.29) into (2.30) yields : .

$$[\alpha]=[e^i]-[C][T]^{-1}[e^s] \qquad (2.31)$$

The dielectric vector $[\varepsilon]$ is easily found from (2.27) and (2.29):

$$[\varepsilon]=[\hat{\alpha}]^{-1}[T]\quad[e^s]+[1] \qquad (2.32)$$

where

$$[\varepsilon]=[\varepsilon_1\ \varepsilon_2\ldots\ldots\varepsilon_N]^T \qquad [1]=[1\ 1\ldots\ldots 1]^T$$

and $[\hat{\alpha}]^{-1}$ is a diagonal matrix NxN whose elements are given by :

$$\hat{\alpha}_{ij}^{-1}= 1/\alpha_{ij} \qquad \text{for } i=j$$
$$= 0 \qquad \text{for } i\neq j\ .$$

The algorithm described above seems to be very attractive. Indeed, the matrices $[T]^{-1}$ and $[C]$ are computed once and stored. They can be used for any dielectric distribution provided that the geometry and the frequency of the the signal remain the same. Then, the computation of $[\varepsilon]$ requires only matrix multiplications and vector additions (the computation of $[\hat{\alpha}]^{-1}$ is straightforward). Another interesting feature is that, for a given number of cells which approximate the cylinder cross-section, there is theoretically no lower limit for the frequency of the incident wave since the assumption of an uniform electric field inside the cells becomes better as the frequency decreases. However, numerical problems inherent to the behavior of Hankel functions with small arguments must be considered.

Hagmann et al. [39], proposed an upper bound on cell-size for the moment method solutions using pulse functions as basis functions. It is stated that significant errors occur in scattering field calculations when the size of the cells is greater than $2/|k|$, where k is the wave factor in the cell medium. For lossless dielectric scatterers, the upper bound is given by :

$$b_j < \lambda_0/\pi\sqrt{\epsilon_j} \qquad (2.33)$$

where b_j is the biggest dimension of the cell j. The condition (2.33) requires some knowledge a priori of the scatterer dielectric distribution. Another feature demonstrates the versatility of the method. Indeed, the cells need not be the same size. Therefore, a first reconstruction may be attempted with equal cell size and then the cross-section may be resampled using smaller cells in areas where the dielectric distribution is suspected to have larger values or to vary significantly. Care must be taken that the condition (2.33) is always met.

Obviously the greater the number of cells, the better the resolution. However, for a given frequency, the arguments of the Hankel functions involved in the matrix coefficients become smaller when the dimensions of the cells are reduced and for the reasons stated above, numerical complications may arise. The number of cells may also give rise to computational problems since the size of the matrices is proportional to N^2, which implies a significant increase of required memory locations and computational time.

The matrix [T] has to be inverted or a solution to (2.28) has to be found. At this point some consideration should be given to the uniqueness of the solution. Indeed, if the solution of (2.28) is not unique, matrix [T] cannot be inverted. This would imply the existence of polarization current densities which do not radiate. Such nonradiating sources may be added to the current density which effectively produces the scattered field (radiating source[1]), without affecting fields observed at discrete points outside the cylinder. In other words, the solution to zero scattered field at discrete locations is not necessarily a trivial solution i.e. a cylinder with uniform

[1]Two distinct radiating sources necessarily produce different scattered fields. Indeed, suppose that they produce identical scattered fields, they would differ only by a nonradiating component according to (2.28).

dielectric constant equal to 1. The question about whether or not such nonradiating sources physically exist is irrelevant since the matrix inversion does not involve any physical considerations. However, it can be easily seen that for a small number of cells, and distinct observation points, the nonradiating source is only a cylinder with zero polarization current density. It should be borne in mind, that the solution using the moment method, with pulse functions as basis functions, is an approximation and therefore the approximation to the homogeneous solution of (2.28) which gives the nonradiating source vector may be only a trivial solution. However, when the number of cells, and consequently the number of observation points, increases it is difficult to ascertain whether the solution is unique. This important question is discussed in more detail in Section 3.3 .

Chapter III

METHOD OF SOLUTION

The objective in the first section of this chapter is to explore the feasibility of the algorithm of reconstruction using computer simulations. There is a great concern about the efficiency of the method when some noise (computational or/and measurement noise) is present in the process. In practical situations, it is expected that some noise is contained in the measurements. Therefore, simulations must include the presence of noise in the scattered field values. In addition, the problem bears many parameters such as the position of the observation points (detectors) and the frequency of the incident wave which influence the accuracy of the reconstruction since both are involved in the [T] matrix elements and have some impact on the behaviour of [T] during its inversion process.

First, the reconstruction of the dielectric distribution of a thin lossless homogeneous cylinder is analyzed. These preliminary results illustrate the ill-conditioned nature of the problem.

It is found that the solution of the problem becomes hopeless if direct inversion of the matrix [T] is attempted even when noise levels are below realistic values. Therefore, the problem must be attacked using optimization techniques similar to those utilized in other fields (image restoration, optics, etc.) namely the least-square minimization. An estimate of the polarization current vector is found such that its magnitude is minimum with the constraint that the norm of the difference (error) between the scattered field vector obtained from the measurements and the scattered field vector that would produce that estimate is minimum. The procedure known as the pseudoinverse transformation generates a unique solution for that estimate.

Finally, the pseudoinverse operator is introduced in the algorithm and the reconstruction of the same simple structure is performed. In addition, the use of the pseudoinverse operator gives some insight into the uniqueness problem which was discussed in previous sections.

3.1 FIRST ATTEMPT : RECONSTRUCTION OF A THIN HOMOGENEOUS RECTANGULAR CYLINDER

The behavior of the algorithm, described in the previous chapter, is analyzed through dielectric-profile reconstructions of a thin homogeneous cylinder with rectangular cross-section and uniform dielectric distribution. This simple structure has been selected because of the simplicity of representing one-dimensional functions. The choice of one-dimensional problems also limits the size of the matrices and consequently considerably reduces the computation time. Nevertheless, this simple example is sufficient to illustrate the principal features of the method and to permit discussion of different possibilities to improve the reconstruction when some noise is added to the measurement values.

The simulation geometry is shown in Fig. 3 . The incident wave is a plane wave[1] with a wavelength λ_0. The dielectric distribution of the scatterer is uniform and arbitrarily chosen equal to 2 (lossless case). The cylinder cross-section is divided into 16 square cells of $0.05\text{-}\lambda_0$ size. The condition (2.33) is certainly satisfied. An array of detectors is located at a distance d from the cylinder axis. The frequency of the incident wave should be selected such that the cylinder cross-section dimensions and the wavelength are of the same order of magnitude. Indeed, the scattered field contains the information about the electric parameter distribution of the scatterer. Consequently, large contributions from the diffraction effects are needed.

The scattered field at the observation points outside the cylinder is computed using the procedure described in Section 2.3. The dielectric profile is reconstructed by solving (2.28) and introducing the solution into (2.30) and

---

[1]It is important to remember that it is not necessary to irradiate the structure with a plane wave. However, this choice pertains to the possibility of propagating TEM waves in a parallel-plate structure for future experimental work.

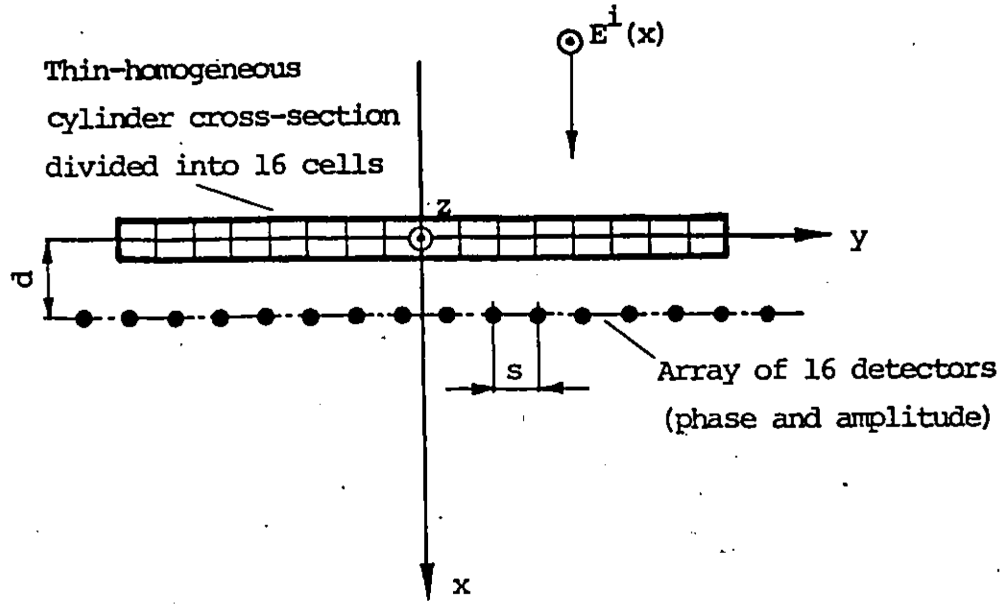

Figure 3: Simulation geometry pertaining to the case of a thin homogeneous cylinder dielectric-profile reconstruction.

A plane wave with 1 V/m peak amplitude (wavelength λ_0) propagating along the x-direction, irradiates a cylinder whose rectangular cross-section (dimension : $0.05 \times 0.8\ \lambda_0$) is divided into 16 identical square cells of $0.05\ \lambda_0$ each. The dielectric distribution of the cylinder is uniform (ε =2-lossless medium). An array of 16 equally spaced detectors is located at a distance d from the origin of the coordinate system symmetrically with respect to the x-axis.

(2.27). Therefore matrix $[T]^{-1}$ is not calculated in this example. Computations are carried out with double precision to minimize the round-off error propagation.

The phase and amplitude of the scattered field in the plane located at a distance of $0.15\ \lambda_0$ (near field) from the z,y-plane, is shown in Fig. 4 . The phase of the incident field is taken arbitrarily equal to zero at the origin of the coordinate system.

Theoretically, for noiseless input data (measured values), it should be possible to reconstruct the dielectric profile of the scatterer with errors no greater than those produced by computations. Figure 5 shows the reconstructed real part[1] of the dielectric profile when some noise is added to calculated scattered field values, for different noise levels. As expected, the signal-to-error ratio in the reconstruction[2] is very high for low noise input data owing to the fact that the relatively small size of matrices involved in the calculations makes the computational round-off errors negligible (see Fig. 5 a)).

The situation worsens dramatically when some noise is introduced to the input data, i.e. to the scattered field values. For a signal-to-noise ratio in the measurements (see footnote p. 40) lower than 85 dB (equivalent to noise levels belo~~w 10~~ ppm), the fidelity of the reconstruction degrades rapidly as shown in Fig. 5 b) and c) . A noise level as low as 1 ppm is required in the present case to reconstruct the

---

[1]The imaginary part presents the same type of discrepancy and is not discussed unless it is clearly mentionned.

[2]Signal-to-error ratio in the reconstruction in dB is calculated as :

$$S_e^{\varepsilon}=20 \log\{ \|[\bar{\varepsilon}]\| / \|[\bar{\varepsilon}]-[\varepsilon]\| \}$$

where $[\bar{\varepsilon}]$ is the original dielectric distribution vector.

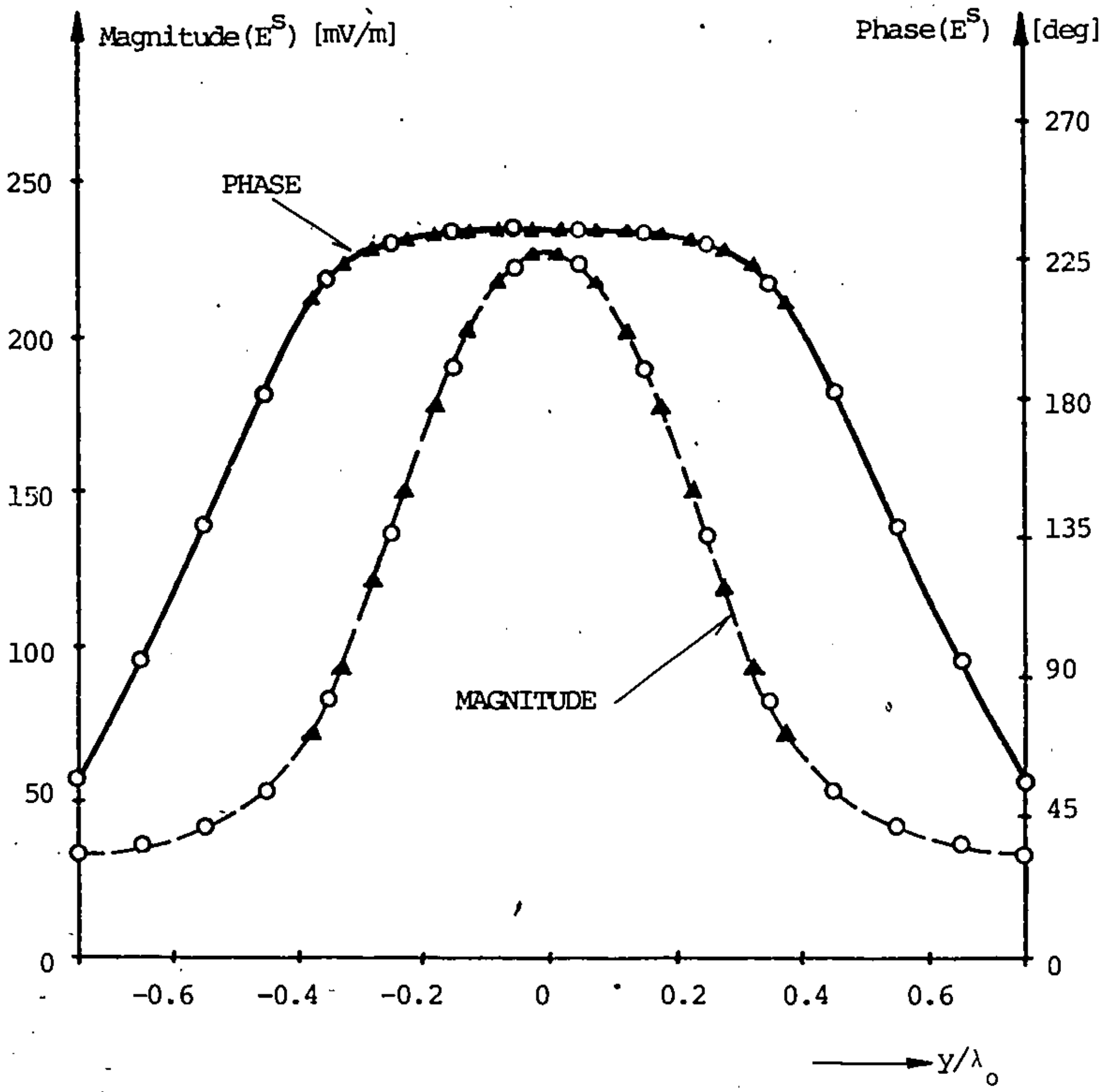

Figure 4: Amplitude and phase of the scattered field produced by the thin homogeneous cylinder depicted in Fig. 3 .

The scattered field is represented in a plane located 0.15 λ_0 from the y,z-plane and containing an array of detectors. The field is computed using the moment method described in Section 2.3 . Triangles and circles indicate the spacing between the detectors : 0.05 λ_0 and 0.1 λ_0, respectively.

dielectric profile with a signal-to-error ratio of 38 dB (the imaginary part is ignored). Obviously, such a noise level is far below practical values. The noise present in the input data simply propagates (as expressed in dB) to the reconstructed dielectric profile and no filtering is evident in the inversion process. It was also found that the reconstructed dielectric profile (including the imaginary part) produces scattered field values identical to noisy input values (neglecting small errors due to computations) in all cases shown by Fig. 5 . In other words, the signal-to-error ratio for the reconstructed scattered field with respect to the input scattered field (see footnote p. 42) is very high. This indicates that the inversion of the matrix [T] is correctly performed.

The position of the detectors is also an important factor that influences the reconstruction fidelity of the dielectric profile. Table 1 a) shows S_e^{ε} vs. spacing s between detectors. The signal-to-error ratio for the reconstructed scattered field with respect to noiseless input data (see footnote p. 42) is also presented. Values show that there is an optimum spacing equal to s=0.05 λ_0 for

---

Signal-to-noise ratio in the measurements in dB is given by :

$$S_n^s=20 \log\{\|[e^s]\| / \|[n]\|\}$$

where $[e^s]$ and $[n]$ are the noiseless scattered field vector and the noise vector respectively.
Noise level (nl) is expressed in part per million (ppm) of the incident wave peak amplitude.
Noise generation process is descibed in Section 4.1 .

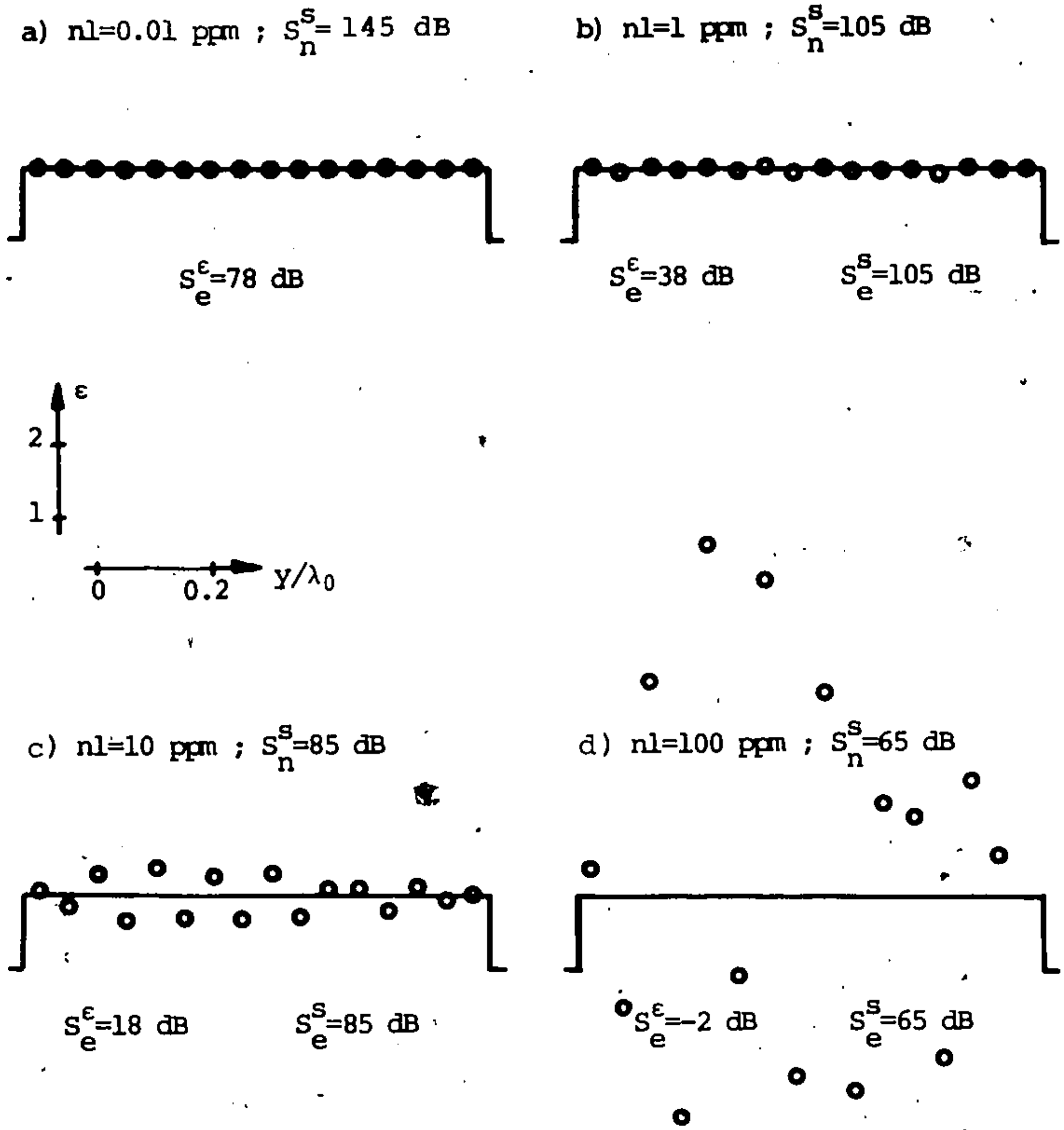

Figure 5: Dielectric profile reconstruction from noisy input data using direct solution of (2.28).

The geometry pertaining to the reconstruction is illustrated in Fig. 3 . Dielectric reconstructions are shown for different noise levels expressed in ppm of the peak amplitude of the incident wave (1 V/m). Spacing s between detectors is 0.05 λ_0 and the array of detectors is located at distance d=0.15 λ_0. The original dielectric distribution is equal to 2 and is represented by a solid line. Circles represent the reconstructed values of the dielectric constant at the center of each cell.

which the reconstruction of the dielectric profile is the most accurate. However, this spacing is not optimum for other array locations. Even for a noise level as low as 0.01 ppm, the fidelity of the reconstruction decreases rapidly when the detector array is moved further away from the scatterer as shown in Table 1 b).

It is expected that if the frequency of the incident signal is increased for a given size of the scatterer, the fidelity of the reconstruction can be improved maintaining the same detector location. Figure 6 illustrates dielectric-profile reconstructions for different noise levels but with the incident wave frequency increased by a factor two. This corresponds to doubling s and $\tilde{d}$ values and the scatterer cross-section dimensions relative to the wavelength. The condition (2.33) is also certainly satisfied. Comparison between Fig. 5 and 6 yields a slight improvement of 6 dB in the reconstruction fidelity for the shorter wavelength taking into account the fact that S_n^s is about 6 dB above the corresponding values for to the case illustrated in Fig. 5 .

Signal-to-error ratio for the reconstructed scattered field in dB is calculated as :

$$S_e^s=20 \log\{\|[e^s]\| / \|[e^s]-[\overline{e}^s]\|\},$$

where $[e^s]$ is the input scattered field vector (measurements) and $[\overline{e}^s]$ is the reconstructed scattered field from the reconstructed dielectric vector using (2.27) and (2.28).
$\overline{S}_e^s$ denotes the signal-to-error ratio for the reconstructed scattered field relative to the noiseless input data.

TABLE 1

Reconstruction fidelity vs. detector location using direct solution of (2.28).

s/λ_0	S_e^{ε}[dB]	S_n^s[dB]	$\overline{S}_e^s$[dB]
0.03	88	146	146
0.05	78	145	145
0.10	13	142	142
0.20	-34	139	139

a) s variable ; $d=0.015\ \lambda_0$

d/λ_0	S_e^{ε}[dB]	S_n^s[dB]	$\overline{S}_e^s$[dB]
0.10	102	145	145
0.15	78	145	145
0.30	6	144	144
0.60	-40	143	143

b) d variable ; $s=0.050\ \lambda_0$

The signal-to-error ratio pertaining to the dielectric-profile reconstruction (S_e^{ε}), scattered field reconstruction ($\overline{S}_e^s$) and signal-to-noise ratio in the measurements (S_n^s) are tabulated as a function of the spacing between detectors s and the distance of the detector array from the y-axis d. The geometry pertaining to the reconstruction is illustrated in Fig. 3 . The noise level added to scattered field values is 0.01 ppm (relative to 1 V/m).
The signal-to-noise ratio in the measurements S_n^s varies as little as 7 dB for the different detector locations whereas S_e^{ε} fluctuates as much as 142 dB !

At this stage, the solution of an inverse scattering problem using the moment method seems totally hopeless under

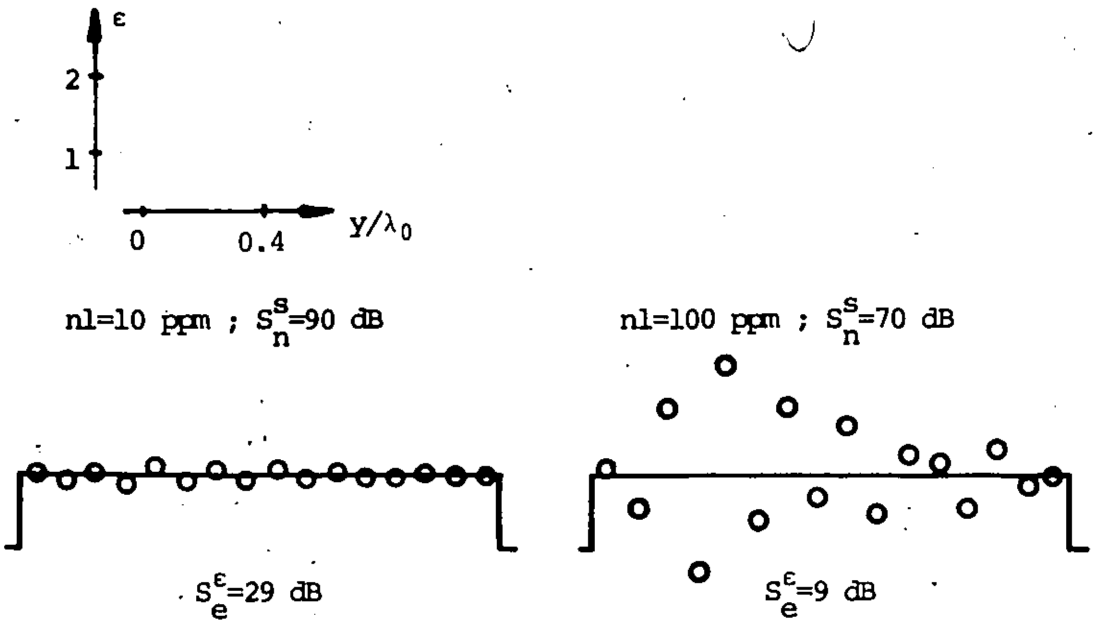

Figure 6: Dielectric profile reconstruction for higher frequency of the incident wave using direct solution of (2.28).

The real part of the reconstructed dielectric profile is illustrated for two different noise levels. The geometry is the same the one used for the case shown in Fig. 5, except that the frequency of the incident wave is doubled. Consequently $s=0.1\ \lambda_0$, $d=0.3\ \lambda_0$ and the scatterer cross-section dimensions are $0.1x1.6\ \lambda_0$.

realistic conditions. The scattering pattern shown in Fig. 4, indicates that there are no significant observation points affected by a large error resulting from noise. Reasonable fidelity reconstructions can be obtained when the detector array is placed at distances well within $0.1\ \lambda_0$ from the scatterer, but practical difficulties would arise as a result of coupling effects between the detectors and the scatterer. Computations show that when the array of detectors is moved further away from the scatterer, the determinant of the matrix [T] is very small even if a scaling factor is used. As a result, the matrix becomes nearly singular. Indeed, at relatively large distances, columns of the matrix [T] which pertain to close adjacent observation points are almost identical owing to the fact that the relative distances from these points and the cells of the scatterer have nearly the same values rendering their elements t_{ij} almost identical. The effect of different spacings upon the behaviour of [T] is not as easy to explain. However, it was found that the determinant of [T] was maximum when spacing s yielded the best fidelity of reconstruction. It turns out that the degree of ill-conditioning of a matrix is somehow related to its determinant [40].

From these preliminary results, one can conclude that except for a few cases, the matrix [T] is generally ill-conditioned. One faces the problem of dealing with matrices with a high condition number defined as a square root of the ratio of its highest and lowest eigenvalues [40]. Near-singularity of a matrix is associated with a very high condition number and the solution of the resulting system of linear equations becomes difficult. In the presence of noise (whether measurement noise or computational noise) the matrix featuring a high condition number can become singular within the bounds of uncertainty imposed by the noise. In the next section, an optimization procedure is described to overcome the difficulties associated with noise sensitivity of the solution.

3.2 LEAST-SQUARES OPTIMIZATION TECHNIQUES

The poor fidelity of the reconstruction illustrated in Fig. 5 c), can be explained as follows :

Suppose that a noisy vector [n] is added to the scattered field vector $[e^s]$. Thus (2.28) can be written as :

$$[e^s]=[T][d]+[n] \quad . \tag{3.1}$$

An estimate of [d] can be generated by

$$[\hat{d}]=[T]^{-1}[e^s] \quad , \tag{3.2}$$

and from (3.1) :

$$[\hat{d}]=[d]+[T]^{-1}[n] \quad . \tag{3.3}$$

The above estimate consists of two parts, the noiseless solution [d] and a term involving an inverse of [T] acting on the noise. It turns out that the matrix [T] has a large condition number, except when a small number of cells is considered. Thus, the inverse $[T]^{-1}$ has very large entries, and consequently the term $[T]^{-1}[n]$ can significantly dominate the noiseless solution [d]. One faces a problem of solving an ill-conditioned system. There is no unique solution in view of noise and ill-conditioning. Some meaningful rationale must be employed to pick a better solution than that, for instance, shown in Fig. 5 c). The linear nature of (2.28) permits one to employ various techniques, which are used in image restoration. An excellent review of those techniques can be found in [40].

Consider the model posed by (3.1). Without any knowledge about [n], a criterion for solution would be based on an estimate of the vector [d] such that

$$\|[n]\|^2 = \|[e^s]-[T][\hat{d}]\|^2 \tag{3.4}$$

is minimum. This is called the least-squares solution philosophy. The operator which minimizes (3.4) is known as an inverse filter. The major inconvenience of that filter is its lack of capability of handling ill-conditioned problems.

Another criterion is to construct an estimate [d] such that the quantity

$$\|[d]-[\hat{d}]\|^2 , \tag{3.5}$$

is minimum. The stochastic nature of this approach, involves some knowledge of the statistical properties of both the noise ~~and~~ the original vector [d]. If the minimization of (3.5) is subject to

$$[\hat{d}]=[L][e^S]$$

where L is a linear operator, this technique leads to the Wiener filter. There is no ill-conditioned behavior associated with the Wiener estimate (or minimum mean-square-error estimate). However, for ill-conditioned problems, it has generally unacceptable smoothing effects.

Additional control over the restoration process, leads to another type of techniques, namely, the constrained least-squares techniques. They, more or less, combine the two previous approaches in different manners. For instance, the norm of the noise [n] may be known or measurable a posteriori. Thus, the problem could be formulated as

$$\text{minimize } \|[L][\hat{d}]\|^2 \qquad (3.6)$$

$$\text{subject to } \|[e^S]-[T][\hat{d}]\|^2=\|[n]\|^2$$

where L is a linear operator. The generality of the matrix [L], allows the development of a variety of constraints. For instance, if [L] pertains to the statistical properties (covariance matrix) of the noise and the original vector, the constrained least-squares technique generates the parametric Wiener filter. It is not always possible to find an adequate model of noise, especially when part of the overall noise is due to round-off error propagation during computations. In addition, the unknown vector [d] may not be positive and consequently a stochastic approach is not appropriate.

A deterministic approach seems more suitable for the problem under consideration. Indeed, the unknown is a complex quantity and for reasons mentioned before, one wants to obtain an estimate without introducing any statistical behaviour of the noise in the measurements or of the original vector [d]. Rather than solving directly the system of linear equations (2.28), an estimate $[\hat{d}]$ is generated such that the norm of the difference (error) between the scattered field vector produced by this estimate and the scattered field input vector (containing the scattered field values measured by the detectors) is minimum with a supplementary condition that the norm of $[\hat{d}]$ is minimized. This can be summarized as follows :

$$\text{Among all } [d] \text{ which minimize } \|[e^S]-[T][d]\|^2,$$

$$\text{find a vector } [\hat{d}] \text{ for which } \|[d]\|^2 \text{ is minimum} \quad , \tag{3.7}$$

with

$$\|[e^S]-[T][d]\|^2=\{([e^S]-[T][d])^*\}^T([e^S]-[T][d])$$

and

$$\|[d]\|^2=([d]^*)^T[d] \quad .$$

The condition (3.7) yields a unique solution of (2.28) if the matrix [T] is not singular. In order to take advantage of the optimization expressed by (3.7), the matrix [T] which generally has a high condition number, is set to be singular, i.e. its nearly dependent column vectors are purposely considered as linearly dependent. The solution of (3.7) is given by [40,41] :

$$[d]=[T]^{\dagger}[e^{S}] \;, \tag{3.8}$$

where $[T]^{\dagger}$ is the pseudoinverse[1] of the matrix [T].

The pseudoinverse transformation (or pseudoinverse filter) has demonstrated its usefulness in many fields facing ill-posed problems such as image restoration techniques [42], optics [43] and recently tomographic image reconstruction [44]. It has the merit of handling problems not only when they are characterized by an ill-conditioned behavior, but also when the matrix of the operator describing the process is singular.

---

[1]The pseudoinverse is sometime referred to as the Moore-Penrose inverse.

3.3 THE PSEUDOINVERSE OPERATOR

A vector space approach is utilized to give a description of the pseudoinverse transformation applied to the framework of the inverse scattering problem :
The matrix [T] represents a bounded linear transformation :

$$T : \mathcal{V} \longrightarrow \mathcal{W} \quad (C^{Nx1} \longrightarrow C^{Nx1})$$

in the complex space C^{Nx1} [1]. An adjoint tranformation :

$$\tilde{T} : \mathcal{W} \longrightarrow \mathcal{V} \quad (C^{Nx1} \longrightarrow C^{Nx1})$$

is defined such that :

$$[\tilde{T}]=([T]^{*})^{T} \quad . \tag{3.9}$$

The existence of $\tilde{T}$ is guaranteed by the bounded[2] linear nature of T.

Let t_j be the column vectors of the matrix [T]. The set of vectors t_j spans a subspace of $\mathcal{W}$ called the range of the operator T (range(T)). One also defines the nullspace of T (nullspace(T)) as a subspace of $\mathcal{V}$ spanned by a set of

---

[1] C^{Nx1} is a complete linear inner product space called Hilbert space.

[2] All transformations on finite-dimensional spaces are bounded [41].

vectors which are the solutions of :

$$[T][d]=0 \quad . \tag{3.10}$$

Physically, nullspace(T) is spanned by the set of nonradiating source vectors since [d] is proportional to the polarization current density vector.

If the t_j are linearly independent, they complete a basis for range(T). The transformation T is said onto W. In the present case, any input vector $[e^s]$ in W is expressed by a unique linear combination of the t_j, implying that the solution of (2.28) is unique. The transformation T is said to be one-to-one. Nullspace(T) in V contains only the zero vector [0].

In the case of ill-posed problems, some of the t_j are nearly dependent. The manner of treating near-singularities is to set all nearly-dependent column vectors of the matrix [T] to be dependent. Consequently, range(T) is no more W and nullspace(T) does not contain only [0]. The input vector $[e^s]$ cannot be expressed as a linear combination of the t_j any more, except if it is contained in range(T) in which case the combination is generally not unique. The system is said to be incompatible. However, a least-error solution is possible.

Consider the following example in R^{3x1} for which range(T) defines a plane (there are two linearly dependent

t_j)[1]. The input vector $[e^s]$ is not contained in range(T). Considering a projection of $[e^s]$ onto range(T) (see Fig. 7), the norm of the error $[e^s]-[e^s]_p$ is minimum when the projection is orthogonal. Then, finding the least-error solution of (2.28) is equivalent to solving :

$$[T][d]=[e^s]_p \tag{3.11}$$

when some column vectors of [T] are set to be dependent and where $[e^s]_p$ is the ORTHOGONAL PROJECTION of $[e^s]$ onto the range of T. There exists an infinite set of vectors [d] in R^{3x1} that satisfies (3.11). The system is underdetermined. Indeed, if it is supposed that the second and third columns of the matrix [T] are dependent, one can transform the linear system (3.11) such that the third column is a zero vector. Therefore the third coordinate of the vector, solution of (3.11) can be arbitrarily chosen.

One wants to find, among all possible solutions, a vector $[d]_s$ which has the smallest norm. The adjoint transformation concept is utilized to explain how the smallest least-error solution of a problem can be found and at the same time describes the pseudoinverse operation.

---

[1]For the sake of simplicity, all vectors in this example are real.

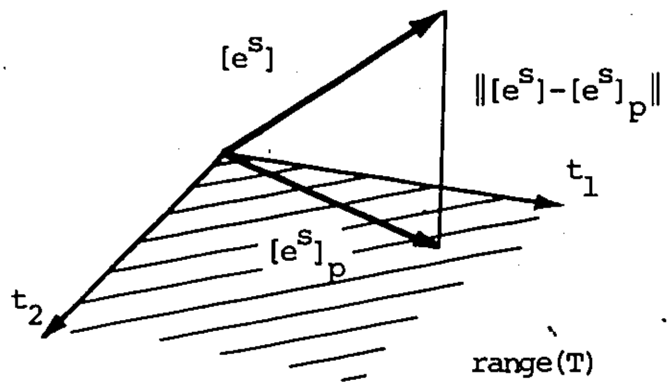

Figure 7: Illustration of a least-error problem in R^{3x1}.

The figure illustrates the vector approach in the search of the least-error solution of a problem described by a matrix equation :

$$[T][d]=[e^S]_p$$

when the system is incompatible. The input vector $[e^S]$ is not contained in range(T), but the minimum error occurs for an estimate of [d] when the input vector is replaced by its ORTHOGONAL projection $[e^S]_p$ onto range(T).

In order to find the nullspace component of any vector of V and using the properties of the operator T shown before, one can utilize the orthogonal decomposition theorem [41] :

$$\mathcal{V}=\text{nullspace}(T)\overset{\perp}{\oplus}\text{range}(\tilde{T})$$

$$\mathcal{W}=\text{nullspace}(\tilde{T})\overset{\perp}{\oplus}\text{range}(T) \qquad (3.12)$$

where the symbol $\overset{\perp}{\oplus}$ indicates that these direct sums are orthogonal. The nullspaces and ranges are orthogonal complements. Expressed in terms of polarization current densities pertaining to the inverse scattering problem, the theorem (3.12) states that the space defined by the nonradiating source vectors is ORTHOGONAL to range(T) spanned by the radiating source vectors.

Let $[\hat{d}]$ be a solution of (3.11). Thus, according to (3.12), it can always be decomposed as :

$$[\hat{d}]=[d]_N+[d]_R \qquad (3.13)$$

where $[d]_N$ and $[d]_R$ are the orthogonal projections of $[\hat{d}]$ onto nullspace(T) and range($\tilde{T}$), respectively. An important corollary of this theorem is that any solution of the linear system produced by (2.28) can always be decomposed into a radiating source (in range($\tilde{T}$)) and a nonradiating one (in nullspace(T)). By virtue of the Pythagorean theorem and the orthogonality property (3.12) :

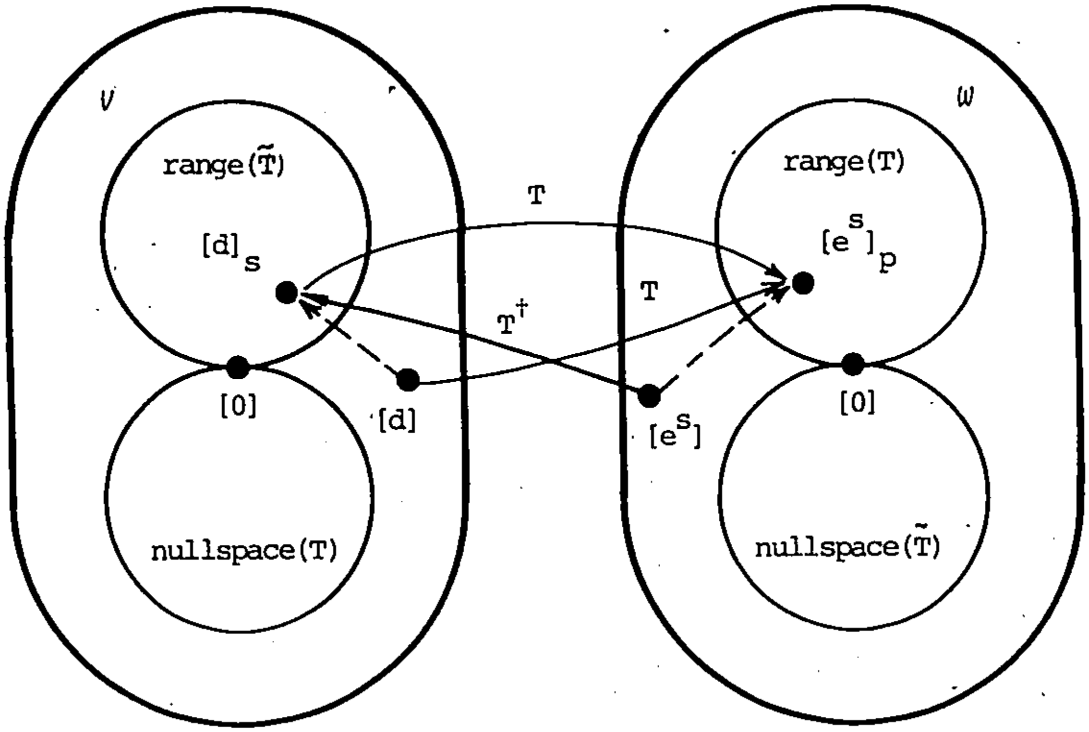

Figure 8: Construction of the pseudoinverse.

The pseudoinverse transformation $T^\dagger$ determines the smallest solution $[d]_s$ to $[T][d]=[e^s]$ which minimizes the error $\|[e^s]-[e^s]_p\|$ when T is neither one-to-one nor onto. Dashed lines indicate orthogonal projections.

$$\|[\hat{d}]\|^2=\|[d]_N\|^2+\|[d]_R\|^2 \quad . \tag{3.14}$$

In order to minimize $\|[\hat{d}]\|$ one has to choose a solution with $[d]_N=[0]$. Therefore, the minimum norm solution $[d]_s$ of (3.11) is an orthogonal projection of any particular vector of the solution (3.11) onto range($\tilde{T}$). The solution $[d]_s$ is indeed unique since any two solutions of (3.11) have the same projection onto range($\tilde{T}$).

The important conclusion from the above discussion pertains to the uniqueness of the solution to the inverse scattering problem using the moment method. Indeed, the smallest least-error solution using the pseudoinverse operator cannot contain any nonradiating components whose presence would imply more than one solution to the problem. One might suggest that although the polarization current density is uniquely determined, both total internal field and relative permittivity may be chosen arbitrarily since P is proportional to the product of these quantities. However, (2.30) precludes any other solution for $[\alpha]$ and by virtue of (2.27), the dielectric vector $[\varepsilon]$ is unique.

To summarize, given an operator T which is neither one-to-one nor onto, the vector $[e^s]$ is orthogonally projected onto range(T) yielding the matrix equation (3.11) whose solutions minimize the error $\|[e^s]-[e^s]_p\|$. Then the hyperplane containing the solutions of (3.11) is projected orthogonally onto range($\tilde{T}$) yielding the unique smallest norm least-error solution $[d]_s$ (see Fig. 8).

The pseudoinverse operation is based upon two ORTHOGONAL projections. However, one could solve the same problem by projecting $[e^s]$ onto range(T) along any subspace X and $[\hat{d}]$ onto range($\tilde{T}$) along any subspace Y such that :

$$\mathcal{V} = \mathcal{Y} \oplus \mathrm{range}(\tilde{T})$$

$$\mathcal{W} = \mathrm{nullspace}(\tilde{T}) \oplus \mathcal{X} \tag{3.15}$$

However, this process[1] does not possess the minimization properties of the pseudoinverse.

Numerous techniques have been proposed for computing the pseudoinverse of an arbitrary matrix [45-48]. The technique proposed in this work utilizes a projection method based on the Gram-Schmidt orthogonalization and is described in detail in Appendix A. An attractive feature of this method is its simplicity and the fact that computational errors are reduced by using pivoting in the Gram-Schmidt orthogonalization procedure.

3.4 PSEUDOINVERSE OPERATOR APPLIED TO THE CASE OF THE THIN HOMOGENEOUS RECTANGULAR CYLINDER

When the matrix [T] is computed, it is not known a priori which one of its column vectors have to be taken as dependent. The orthogonalization of the matrix [T] yields column vectors which have a norm relatively small compared with the remaining column vectors when the matrix has an

[1]Projecting onto any particular subspaces satisfying (3.15) to obtain $[e^s]_p$ and then $[d]_s$ defines a GENERALIZED INVERSE of [T].

high condition number. These small vectors are set to a [0] vector and the minimum least-error solution of (2.28) is calculated. Then [d] is introduced into (2.30) and the solution is found using (2.27). The reconstruction of the dielectric profile of the homogeneous thin cylinder is shown in Fig. 9 for different noise levels in the measurements. The geometry is the same as the one illustrated in Fig. 5 . There are great differences between these two figures. Whereas the solution diverges completely for noise levels greater than 100 ppm using direct inversion of (2.28), S_e^{ε} as large as 32 dB (see Fig. 9 c)) is feasible with pseudoinverse transformation for noise levels as high as 10,000 ppm (equivalent to about 10 per cent average error in the measurements). The pseudoinverse operator acts like a low-pass filter and removes noise components during the transformation at a price of reducing the spatial bandwidth of the algorithm as depicted in Fig. 9 d) . Bandwidth limitations of the method are further discussed in Chapter IV.

The position of the detectors is not as critical as in the direct solution of (2.28). The signal-to-error ratio in the reconstruction for the real part of the dielectric profile and the scattered field vs. detector spacing and distance of the detector array from the y-axis are listed in Table 2 a) and b) respectively. The parameters pertaining to the geometry are the ones used in Table 1 for the same noise

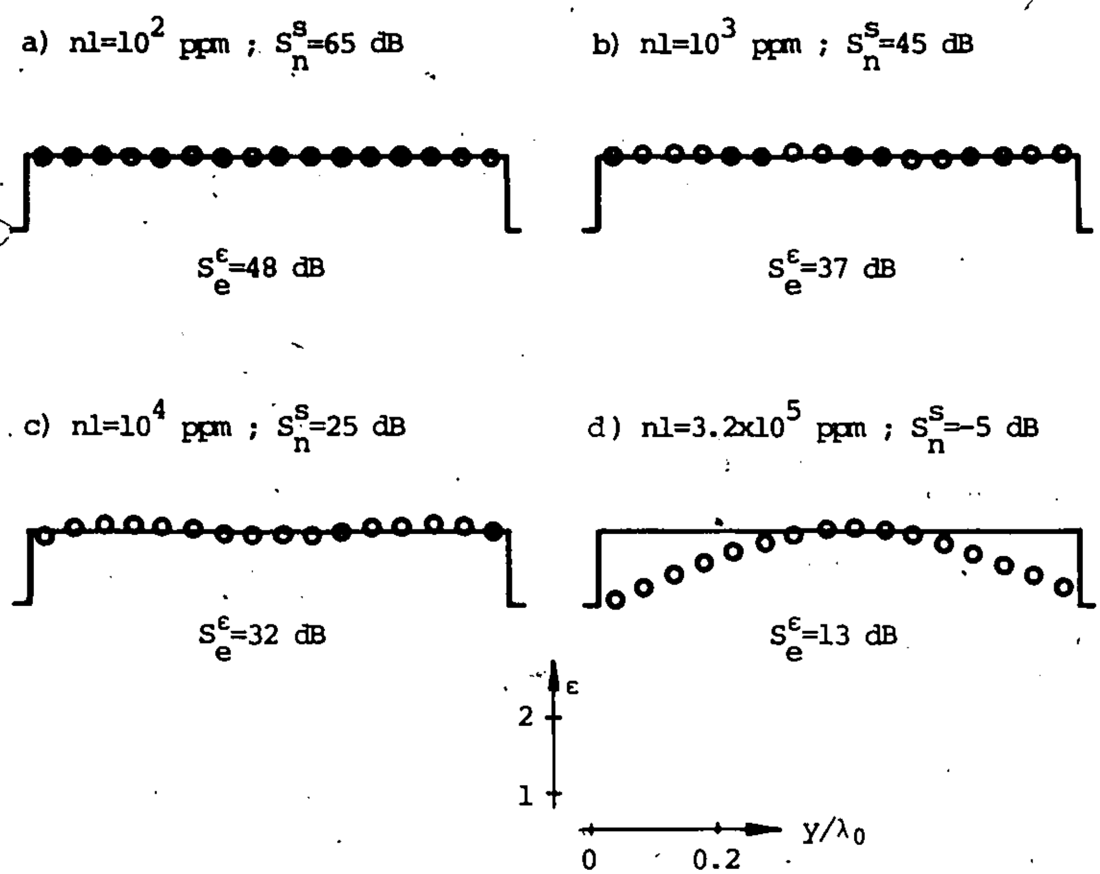

Figure 9: Dielectric profile reconstruction from noisy data using the pseudoinverse operator.

The real part of the dielectric distribution reconstruction is represented for different noise levels in the measurements. The parameters pertaining to the geometry are the same as the ones used in Fig. 5 . Both the signal-to-error ratio in the reconstruction S_e^ε and the signal-to-noise ratio in the measurements S_n^s are indicated.
The bandwidth of the reconstruction algorithm is greatly reduced for relatively high noise levels as shown by Fig. 9 d) .

level. A comparison of the values in Table 1 b) and Table 2 b) shows that the pseudoinverse operator is significantly less sensitive to the array location than in the situation in which the direct solution of (2.28) was utilized. Indeed, excellent fidelity of reconstruction is achieved even for an array located as far as 0.6 λ_0 from the scatterer axis. However, S_e^{ε} is slightly smaller when the array of detectors is moved further away from the scatterer, even though the signal-to-noise ratio in the measurements remains pratically constant. As explained before, the number of nearly dependent columns of the matrix [T] increases when the detectors are moved further away from the scatterer, increasing the ill-conditionning of [T], limiting the spatial bandwidth of the method and consequently introducing some distortion in the reconstructed dielectric profile.

Table 2 a) also identifies an optimum spacing around 0.10 λ_0 for which the matrix [T] has a relatively good behavior. This optimum value of s changes when other parameters such as the detector array location, the frequency of the incident wave or the size of the scatterer, are modified but remains constant when only the dielectric distribution of the scatterer is modified. Indeed, the permittivity is not involved in matrix-[T] element calculations. This important observation points out a possibility of finding an optimum geometry using computer simulations before proceeding to practical experiments.

TABLE 2

Reconstruction fidelity vs. detector location using the pseudoinverse transformation.

s/λ_0	S_e^{ε}[dB]	S_n^s[dB]	$\bar{S}_e^s$[dB]
0.03	48	147	146
0.05	84	145	145
0.10	101	144	142
0.20	67	141	139

a) s variable; $d=0.015\ \lambda_0$

d/λ_0	S_e^{ε}[dB]	S_n^s[dB]	$\bar{S}_e^s$[dB]
0.10	84	145	145
0.15	84	145	145
0.30	74	147	144
0.60	70	147	143

b) d variable; $s=0.005\ \lambda_0$

The signal-to-error ratio pertaining to the dielectric-profile reconstruction (S_e^{ε}), scattered field reconstruction ($\bar{S}_e^s$) and signal-to-noise ratio in the measurements (S_n^s) are tabulated as a function of the spacing between the detectors s and the distance of the detector array from the y-axis d. The geometry pertaining to the reconstruction is illustrated in Fig. 3 . The noise level added to scattered field values is 0.01 ppm. Comparison with Table 1 shows that the pseudoinverse operation effectively attenuates S_e^{ε} fluctuations when the detector location is changed.

A major parameter which has a great impact on the reconstruction fidelity is the number of column vectors N_i of the matrix [T] taken as independent during the reconstruction process. Indeed, N_i is related to some extent to the spatial cutoff frequencies inherent to the

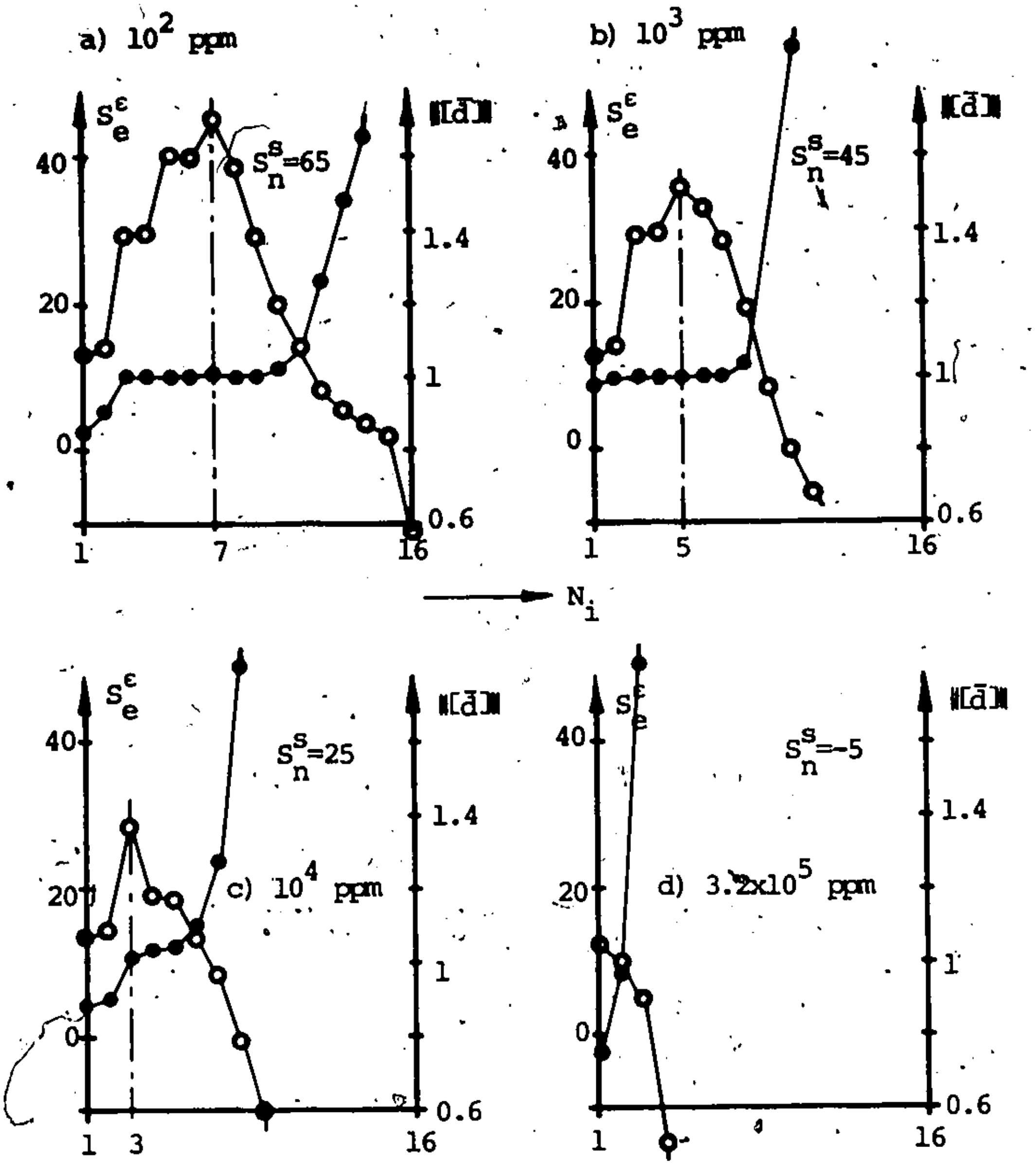

Figure 10: The fidelity of the reconstruction vs. the number of independent column vectors of [T].

The norm of an estimate vector [d] (normalized to the noiseless solution) represented by dots and the signal-to-error ratio in the reconstruction (S_e^ε) represented by circles, are illustrated as a function of the number of column vectors N_i of the matrix [T] taken as independent for four different noise levels. Dashed lines indicate N_i values for the best dielectric-profile reconstruction fidelity.
Diagrams pertain to the case illustrated in Fig. 9 ($s=0.05\ \lambda_0$ and $d=0.15\ \lambda_0$).

pseudoinverse transformation. Figure 10 shows the norm of the vector [d] and the signal-to-error ratio in the reconstruction as a function of N_i for four different noise levels in the situation illustrated in Fig. 8 . The figure reveals the existence of a plateau followed by an abrupt increase of $\|[\bar{d}]\|$ (dots), accompanied by a rapid decrease of S_e^{ε} (circles) above a critical value of N_i. For low signal-to-noise ratios, the plateau does not appear clearly as depicted in Fig. 9 c) and d). In practical situations, the dielectric distribution is indeed not known a priori and consequently S_e^{ε} cannot be calculated. The sole quantity that can be determined during the calculations is the norm of the estimate vector [d]. As a result, it is the only parameter that can give some information about which value of N_i should be selected.

A physical interpretation of the above observations can be given if one considers that according to (2.27), the norm of [d] represents a discretized value of the following surface integral (within the multiplicative factor $j\omega\varepsilon_0$) :

$$\iint_S \|\vec{P}\| dS' , \tag{3.16}$$

where $\vec{P}$ is the polarization current density vector and S is the scatterer cross-section. Consequently, finding the absolute minimum norm of [d] which minimizes the error between the input scattering field values and the ones

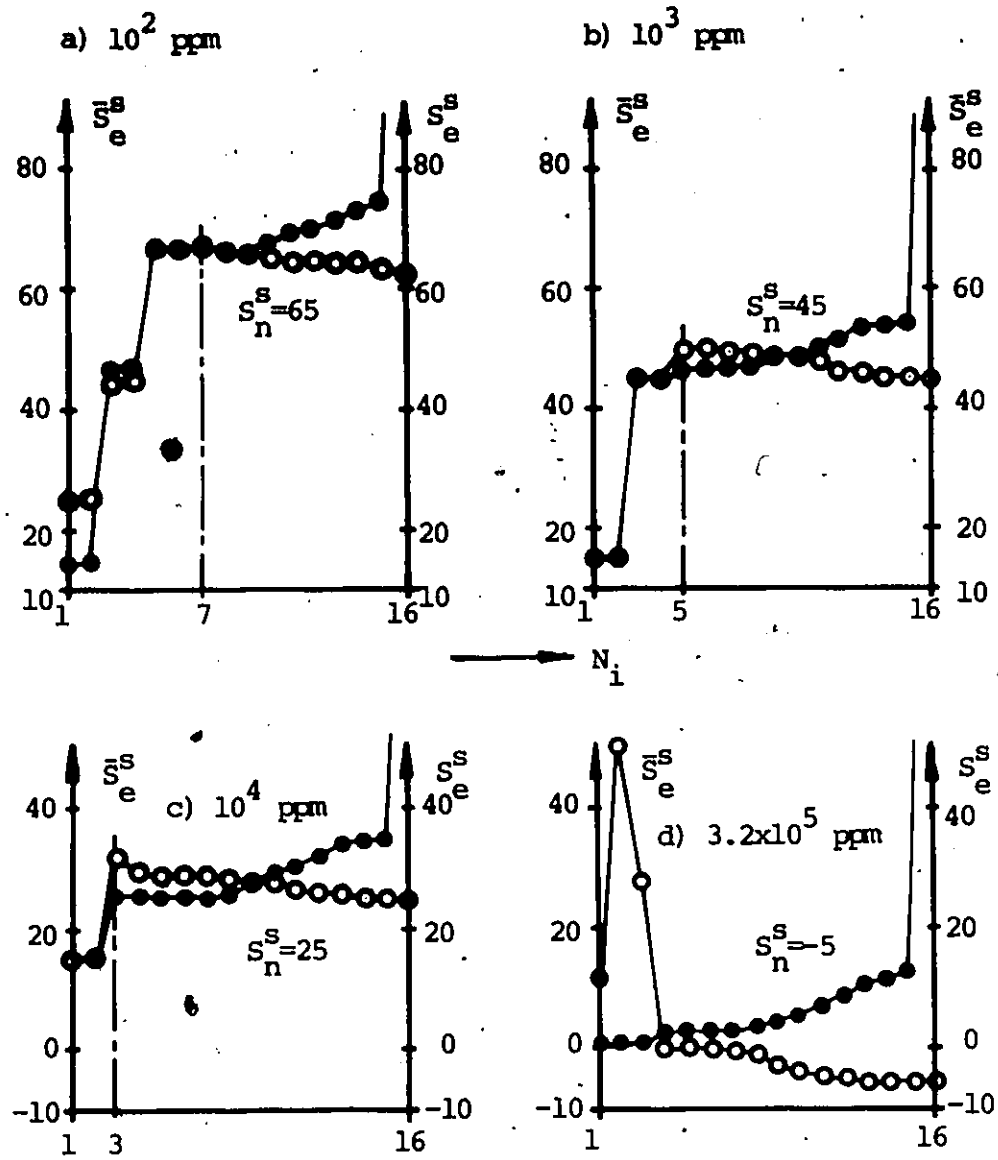

Figure 11: The input data reconstruction error vs. the number of independent column vectors of the matrix [T].

The signal-to-error ratio of the reconstructed scattered field $\bar{S}_e^s$ with respect to the noiseless input data is illustrated as a function of the number N_i of [T] independent column vectors for 4 different noise levels (circles). The signal-to-error ratio for the reconstructed scattered field computed with respect to noisy input data is also represented as a function of N_i (dots). Dashed lines indicate N_i values for the best dielectric-profile reconstruction fidelity. Diagrams pertains to the case illustrated in Fig. 9 (s=0.05 λ_0 and d=0.15 λ_0).
For N_i=16, the pseudoinverse is equivalent to $[T]^{-1}$.

produced by the estimate (equivalent to maximizing S_e^s), is equivalent to minimizing the polarization current distribution across the cylinder cross-section taken together with the constraint of obtaining a least error of the reconstructed scattered field. The minimization of the volume current distribution magnitude was proposed by Muller [49] to overcome the problem of uniqueness for an inverse scattering solution. A similar condition on the energy source was proposed by Porter and Devanay [28] for solving the inverse source problem in holography. According to Fig. 10, the absolute minimum of $\|[\bar{d}]\|$ appears for N_i equal to 1. The selection of $N_i=1$ would reduce considerably the bandwidth of the system and severe distortions would appear in the reconstruction especially in the case of original dielectric distributions with a wide spatial frequency spectrum as illustrated in Fig. 9 d). On the other hand, taking N_i too large does not optimize the solution efficiently and the reconstructed profile would be overhelmed by noise and would require some additional filtering. In practical situations, different reconstructions must be performed and compared. The N_i values should be selected on the plateau of the $\|[\bar{d}]\|$-vs.-N_i curves. The norm of [d] is not absolutely minimum but it turns out to be close to the noiseless solution for [d] and the error on reconstructed data is smaller than for $N_i=1$ as illustrated in Fig. 11 . In this figure, the signal-to-error ratio in the reconstruction computed relative to the noiseless data ($\overline{S}_e^s$) and noisy data (S_e^s) is represented as a function of N_i. A comparison with Fig. 10 shows that the best reconstruction of the scattered field (with respect to the noiseless data) generally occurs for maximum S_e^ε . In addition, $\overline{S}_e^s$ is always larger than the signal-to-noise ratio S_n^s in the measurements. For N_i=16, the pseudoinverse acts as $[T]^{-1}$ and the reconstructed scattered field values are, within small computation errors, identical to noisy input data.

These observations show that seeking the optimum, smallest least-error solution of an ill-conditioned problem is a compromise between the fidelity of the solution and the error of the reconstructed input data with respect to the noisy input vector for a given level of noise. This compromise is determined by the selection of N_i.

3.5 CONCLUDING REMARKS

A simple example of reconstruction proved that a solution of the problem is generally impossible if the polarization current vector is determined directly using matrix inversion from the input scattered field vector when the latter contains some noise. Taking a compromise between the scattered field values produced by an estimate solution and the scattered field effectively measured, yields excellent results even for relatively high noise levels in the measurements. This compromise can be easily realized by the pseudoinverse operator instead of direct inversion.

The pseudoinverse of a matrix involves a choice of a certain number of column vectors of that matrix that have to be taken as linearly dependent. This selection is a compromise between the quality of the solution and the difference between the reconstructed scattered field vector from an estimate of the dielectric vector and the noisy input vector (containing the measured scattered field values). The selection of the number of independent column vectors of the matrix [T] also affects the spatial frequency bandwidth capability of the system. For any number of independent column vectors of [T], the solution for the polarization vector (and consequently the dielectric vector) is unique and do not imply any nonradiating components which alleviates ambiguities about the uniqueness of the solution. This property is inherent to the pseudoinverse transformation.

Chapter IV

COMPUTER SIMULATIONS AND RESULTS

In the previous chapter, the pseusoinverse transformation was found to be an effective tool in seeking a solution of an ill-conditioned problem. However, the utilization of the pseudoinverse operator in the algorithm for dielectric profile reconstructions generally results in a significant spatial bandwidth limitation when some noise (computational and/or measurement noise) is present in the process. In addition, many parameters pertaining to the problem such as the position of detectors (observation points) and frequency of the incident wave[1] play an important role in the degree of ill-conditioning of the matrix [T], which is directly involved in the bandwidth performance of the operator.

The objective of this chapter is to investigate the spatial resolution capability of the algorithm. First, various reconstructions of dielectric profiles of thin rectangular cross-section cylinders are presented to depict the impact of different parameters of the problem on the fidelity of the reconstruction. The selection of these one-dimensional dielectric distributions is inherent to the

---

[1]The dimensions of the scatterer are constant throughout simulations but may change if expressed relatively to the wavelength.

facility of displaying such functions as mentioned in the previous chapter. Then, various dielectric distributions with different spatial frequency spectra (including some two-dimensional dielectric distributions) are presented and the spatial resolution of the system is evaluated. Finally, the feasibility of the algorithm is discussed and some steps are proposed to improve the spatial resolution of the method.

4.1 SIMULATION GEOMETRY (1-D CASE)

The simulation geometry is shown in Fig. 12 . The situation is the same as in Chapter III except that the cylinder cross-section can be divided into more than 16 cells. A distinction between the number of cells N and the number of detectors N_d is introduced. The dielectric scatterer may be lossy and its dimensions may vary relative to the wavelength.

Simulations must be performed under realistic conditions i.e. measurement values from the detectors should include some noise which is caused mainly by interference due to multiple reflections. The presence of noise in the measurements is simulated by adding a random complex vector before each reconstruction to the noiseless scattered field vector. The real and imaginary parts of this noise vector are generated by two independent gaussian sequences with

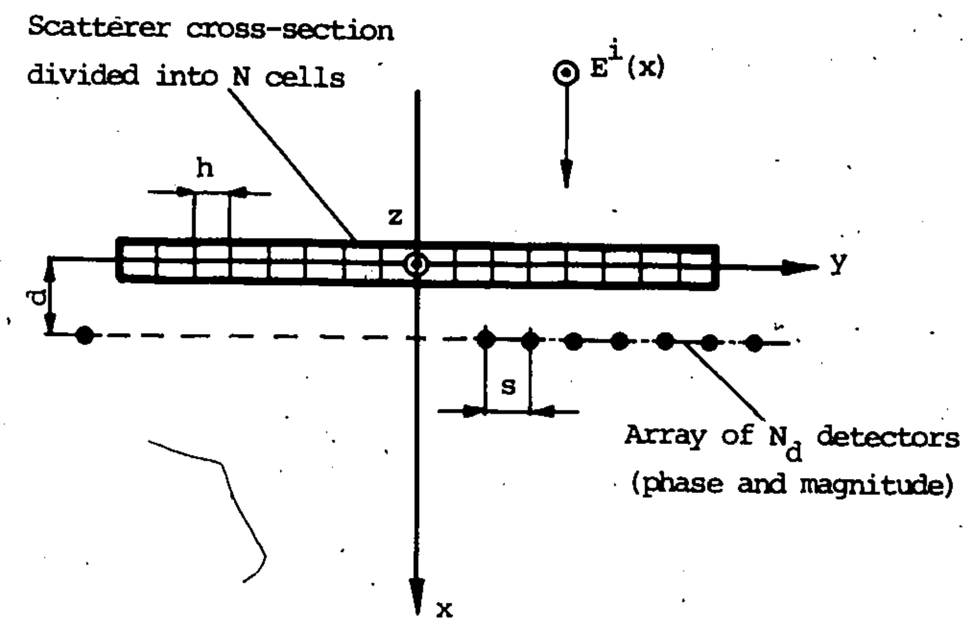

Figure 12: Simulation geometry for the one-dimensional case.

A plane wave with 1 V/m peak amplitude (wavelength λ_0) propagating along the x-direction, irradiates a cylinder whose rectangular cross-section (dimension : $0.05 \times 0.8\ \lambda_0$) is divided into N identical cells (dimension : $0.05\ \lambda_0 \times h$). An array of N_d equally spaced detectors is located at a distance d from the origin of the coordinate system symmetrically with respect to the x-axis.

zero mean value. The orthogonal combination of these two sequences yields components of the noise vector. One can show that the amplitude and phase of each component are also independent and that they have a Rayleigh and uniform probability density function, respectively. This model simulates adequately the random envelope of a signal with interference components [50]. This process is known as multiplicative noise.

Computations of the dielectric vector solution are carried out with double-precision[1] to minimize round-off error propagation. In order to minimize the CPU time and the memory storage requirements, the minimum least-error solution of (2.28) was calculated rather than the pseudoinverse.

The reconstruction fidelity depends on the selection of the number of column vectors of the matrix [T] taken as independant. Consequently, solutions of (2.28) where found for various values of N_i, and the corresponding curve $\|[\bar{d}]\|$-vs.-N_i was plotted (see Fig. 10). Then, the dielectric vector for each N_i value was reconstructed using (2,31) and (2.37). Finally, the the solution which yielded the best S_e^{ε} was selected. Obviously, the last part of the above procedure does not reflect any practical situation. Indeed, the original distribution is generally not known and consequently, S_e^{ε} cannot be calculated.

[1] 64 bit precision on the Amdahl 470/V7A computer.

4.2 POSITION OF THE DETECTORS.

From the results in the previous chapter it is found that the fidelity of reconstruction is affected to some extent by the spacing between the detectors (see Table 1). In addition, there is an optimum spacing (for a given location of the detector array) which yields the best reconstruction fidelity. Likewise in pactical situations, the optimum spacing is determined by a series of reconstructions of known dielectric distributions. The values pertaining to the optimum spacing evaluation are listed in Table 3 . The dielectric distribution used for this test is an asymmetric triangle function represented by solid lines in Fig. 13 . The distance of the detector array from the origin of the system of coordinates is $0.3\ \lambda_0$. By inspection of Table 3 an optimum spacing $s=0.1\ \lambda_0$ was selected and used in subsequent experiments when $d=0.3\ \lambda_0$. As already observed in Section 3.3, the pseudoinverse transformation is relatively insensitive to s variations as far as S_e^{ε} values are concerned. However, the parameter N_i is important for the spatial bandwidth capability of the algorithm and should be chosen as large as possible. Therefore $s=0.1\ \lambda_0$ should be selected for this geometry since it yields the best fidelity reconstruction and the largest N_i for a given S_n^s.

The tests described above should always be performed when the geometry of the problem is modified. This assures optimum conditions for any original dielectric-distribution reconstruction.

TABLE 3

Reconstruction fidelity vs. detector location.

s/λ_0	S_e^{ε} [dB]	S_n^s [dB]	N_i
0.03	36	144	10
0.05	37	144	12
0.10	37	142	12
0.15	32	141	10
0.20	34	140	11
0.30	33	139	9
0.40	33	138	9

Values of S_e^{ε}, S_n^s and N_i are tabulated vs. the spacing between detectors. The (real) dielectric distribution of the scatterer is an asymmetric triangle function represented by solid lines in Fig. 13 . Calculations of S_e^{ε} include real part of only. The number of cells and detectors is 16. The detector array is placed at a distance of 0.3 λ_0 from the origin and the noise level in the measurements is 0.01 ppm.
The optimum spacing is $s=0.1\ \lambda_0$.

4.3 NOISE IN MEASUREMENTS

The influence of noise in the measurements is illustrated in Fig. 13 for an asymmetric triangular dielectric-distribution function. A very strong low-pass filtering effect is observed for relatively high noise levels as shown in Fig. 13 c) and d). The pseudoinverse transformation removes completely noise components if an appropriate value of N_i is selected. For relatively high noise levels (low S_n^s values), low values of N_i should be selected for an optimum reconstruction fidelity. These low N_i values reduce the spatial frequency bandwidth of the algorithm which results in some distortions of the reconstructed profiles.

The spatial bandwidth of the algorithm can be adjusted accordingly with the level of noise present in the measurements or generated by round-off error propagation during computations. The adjustment of the bandwidth capability of the algorithm depends on various factors for a given level of noise namely the position of the detector (section 4.2) and the frequency of the incident wave for a given geometry (section 4.4). Figure 14 shows the effect of the selection of N_i on the spatial frequency bandwidth capability of the algorithm when no measurement noise is present. This figure is almost a replica of Fig. 13 which indicates the lack of sensitivity to measurement noise below a certain level, for a selected value of N_i. For instance, S_n^s above 42 dB results in a reconstruction fidelity shown in Fig. 14 b) for the case under discussion and N_i=4. The effect of computational noise is shown in Fig. 14 c) for which 15 out of 16 column vectors of the matrix [T] should be taken as independent for optimum reconstruction. Some improvement seems feasible by selecting higher values for N_i implying the presence of noisy oscillations in the reconstructed profile. Such oscillations, if their amplitude is relatively small, can be removed by appropriate filtering techniques other than low-pass-like ones. This possibility is further investigated in Section 4.9 for a selected

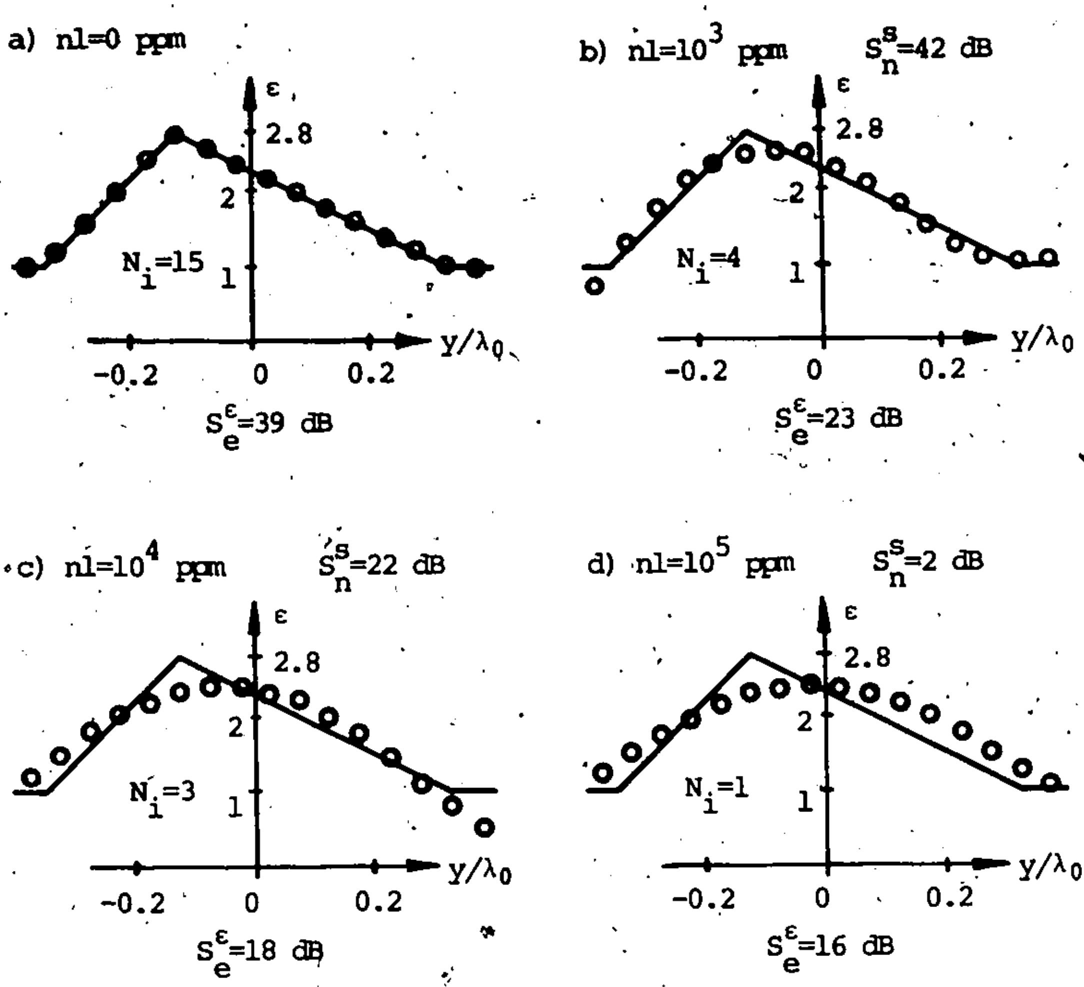

Figure 13: Reconstruction fidelity vs. the input noise level.

The real part of the reconstructed dielectric profile is depicted for different noise levels present in the measurements. The original dielectric distribution is represented by a solid line.
The geometric parameters are $s=0.1\,\lambda_0$, $d=0.3\,\lambda_0$ and $N=N_d=16$.
A strong spatial bandwidth limitation is evident for nl greater than 1000 ppm (relative to 1 V/m) in this example.

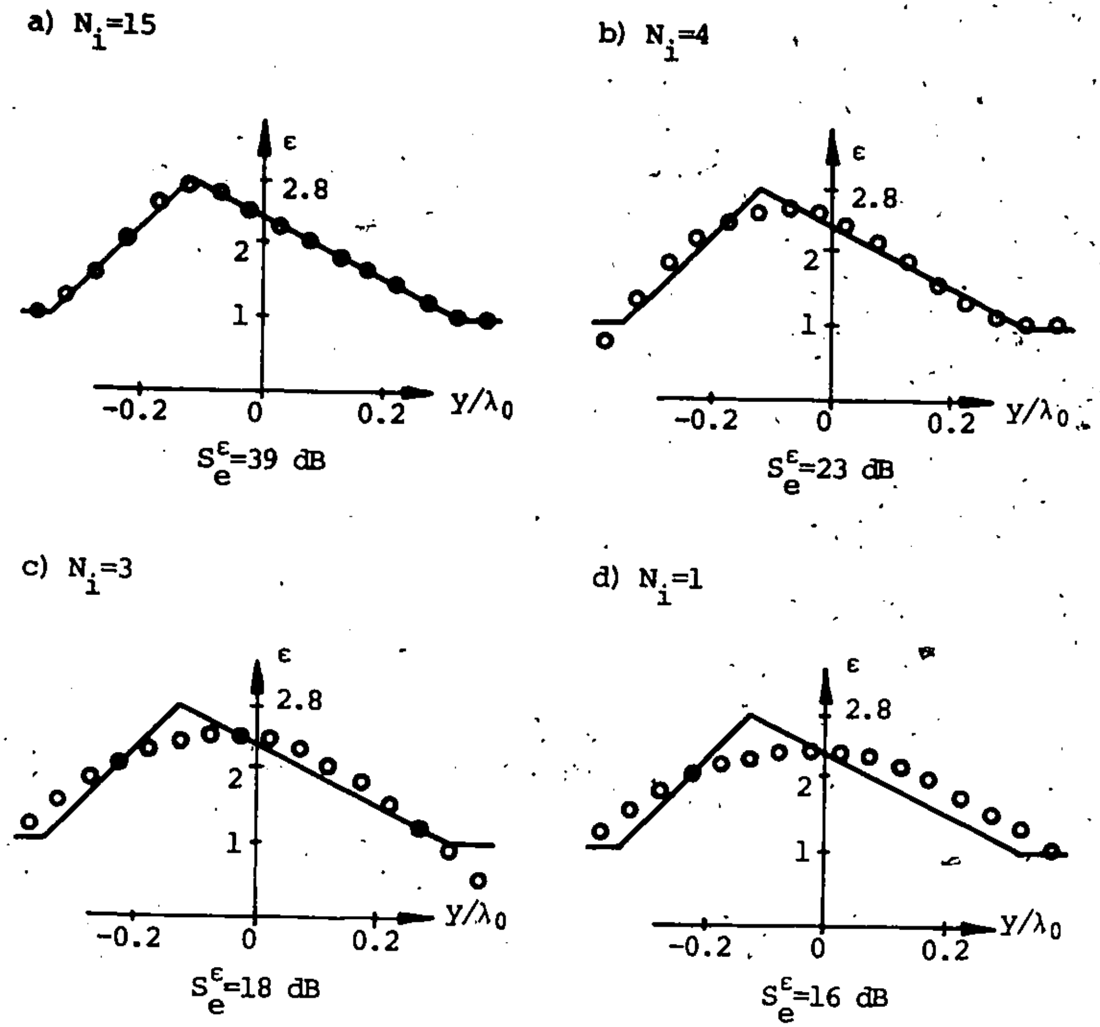

Figure 14: Reconstruction fidelity vs. N_i as illustrated in Fig. 13 but with noiseless input data.

The real part of the reconstructed dielectric profile is shown for the case depicted in Fig. 13 but for noiseless input data and the corresponding N_i values . This figure reveals the band-limiting effect of the algorithm due to the decreasing values of N_i.

dielectric profile for which band-limiting effects are more apparent than in the case presented in Fig. 13 .

In addition to the noise resulting from the radiofrequency interference, which is most likely to be the main cause of uncertainties in the measurements, the noise of the detectors and other electronic components may also contribute to the overall noise. Such noise has different statistical characteristics than the noise utilized in the present simulations. However, its effects upon the performance of the algorithm should be qualitatively similar.

4.4 RELATIVE SIZE OF THE SCATTERER CROSS-SECTION

The frequency of the incident signal plays an important role. As mentioned before, imaging over a range of frequencies may provide additional information for diagnostic purposes. However, some criteria should be considered before selecting these frequencies. It is assumed that the dimensions of the scatterer cross-section and the size of the cells are given. In practical situations, the range of scatterer permittivity values are approximately known and therefore the highest frequency of the incident wave that can be used is determined by the condition (2.33) for lossless cases. At lower frequencies, another factor arises inherent to the relatively small size of the scatterer and cells which renders the matrix [T] more ill-conditioned than at higher frequencies. The advantage of using low frequencies pertains to lossy scatterers in which the electric field and consequently the polarization current are less attenuated [56,57]. Consequently, a better transmission of the wave through the scatterer is obtained and this should result in some improvement in the reconstruction fidelity. The influence of the frequency of the incident wave on the reconstruction fidelity is depicted in Fig. 15 . The original dielectric distribution is an asymmetric triangle function with a peak amplitude of 2.8 .

For long wavelengths, the electric dimensions of the scatterer cross-section becomes small and therefore scattering effects are reduced. This is expressed in a drastic drop of S_n^s. The pseudoinverse transformation band-limits the reconstruction algorithm in such a way that only one column vector of the matrix [T] should be taken as independent for an optimum reconstruction. As a result, only the DC-component of the original dielectric distribution (mean value) is restored as shown in Fig. 15 c). The spacing used for this case is not optimum[1] and further tests would most likely improve the results.

The distance of the detector array from the scatterer, for the case shown in Fig. 15 c), is 0.1 λ_0 and according to previous observations a better reconstruction fidelity

---

[1]The position of the detectors and the size of the scatterer were fixed such that the spacing between detectors is optimum only for the case illustrated in Fig. 15 b) .

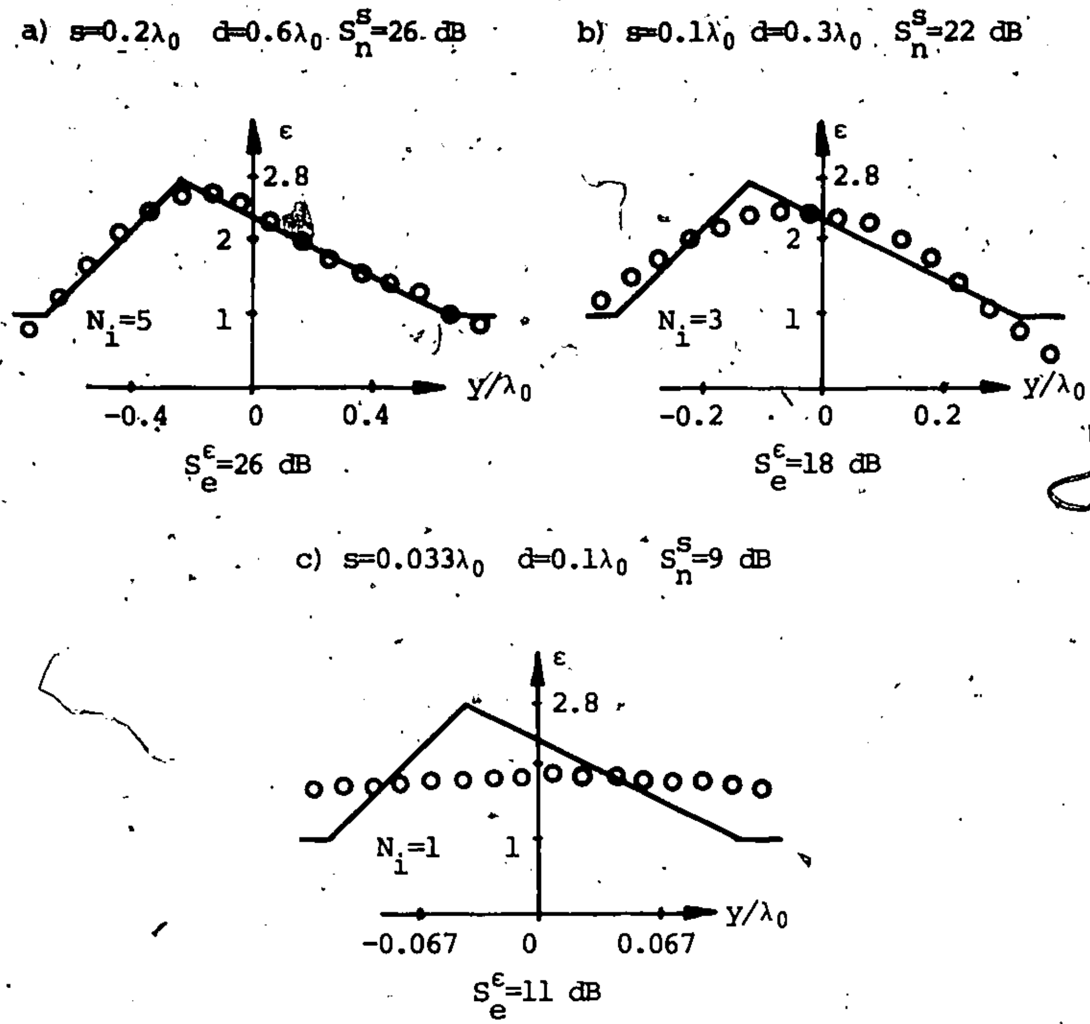

Figure 15: Reconstruction fidelity vs. wavelength.

The dielectric constant reconstruction is shown for different irradiation wavelengths. The dimensions of the scatterer and the position of the detectors are fixed. The noise level present in the input data is 10,000 ppm and $N=N_d=16$.
For relatively long wavelength the band-limiting effect is so high that only the DC-component (mean value) of the original dielectric distribution is restored (see Fig. 15 c).

should be obtained. The reason for this discrepancy is that the spacing between detectors is so small (with respect to the wavelength) that the observation points are almost equivalent for every cell of the scatterer cross-section implying a very high ill-conditioning of the matrix [T].

On the other hand, the fidelity of reconstruction is slightly improved when the wavelength is shortened as shown in Fig. 15 a). Although S_n^s is 4 dB larger than in the case illustrated in Fig. 15 b), the reconstruction fidelity is improved by 8 dB. This suggests that for a given size of the scatterer, the frequency range of the incident wave should be selected as high as possible (within the condition (2.32)), when low-loss structures are concerned. For relatively high-loss media (biological tissues for instance), the selection of the incident wave frequency range should be a compromise between an adequate transmission of the wave through the body and the size of the scatterer cross-section which should be at least of the order of the wavelength.

4.5 CONTRAST

In this section, the reconstructions of identical dielectric profiles with different amplitude factors are presented. The objective is to determine the effect of the distribution contrast, on the reconstruction fidelity.

The reconstruction of three asymmetric triangle-like dielectric profiles with different dielectric constants (varying contrast) are shown by Fig. 16 . The relative reconstruction fidelity does not vary significantly for the three cases despite widely different values of S_n^s. Comparisons of the signal-to-error ratios of the reconstruction are difficult in this case because the computation of this quantity favors high-contrast distributions. This can be observed in Fig. 16 b) and c). Indeed, the reconstruction fidelity is similar in both cases but their S_e^ε differs by 18 dB. However, better reconstruction fidelity would occur for low-contrast distributions if comparable S_n^s values were assumed. This is demonstrated by comparing Fig. 16 b) and c). It turns out that the fidelity of reconstruction pertaining to these two cases is comparable, yet a much higher S_n^s value (36 dB) is obtained for the high-contrast distribution. Consequently, augmenting S_n^s by a corresponding value, in the case of the low-contrast dielectric distribution, would considerably enhance its reconstruction fidelity.

The relatively high S_n^s values for the high-contrast dielectric distributions result in a wider spatial frequency bandwidth of the algorithm. This is translated to a higher value for N_i as shown in Fig. 16 b) in which higher spatial frequency components are visible.

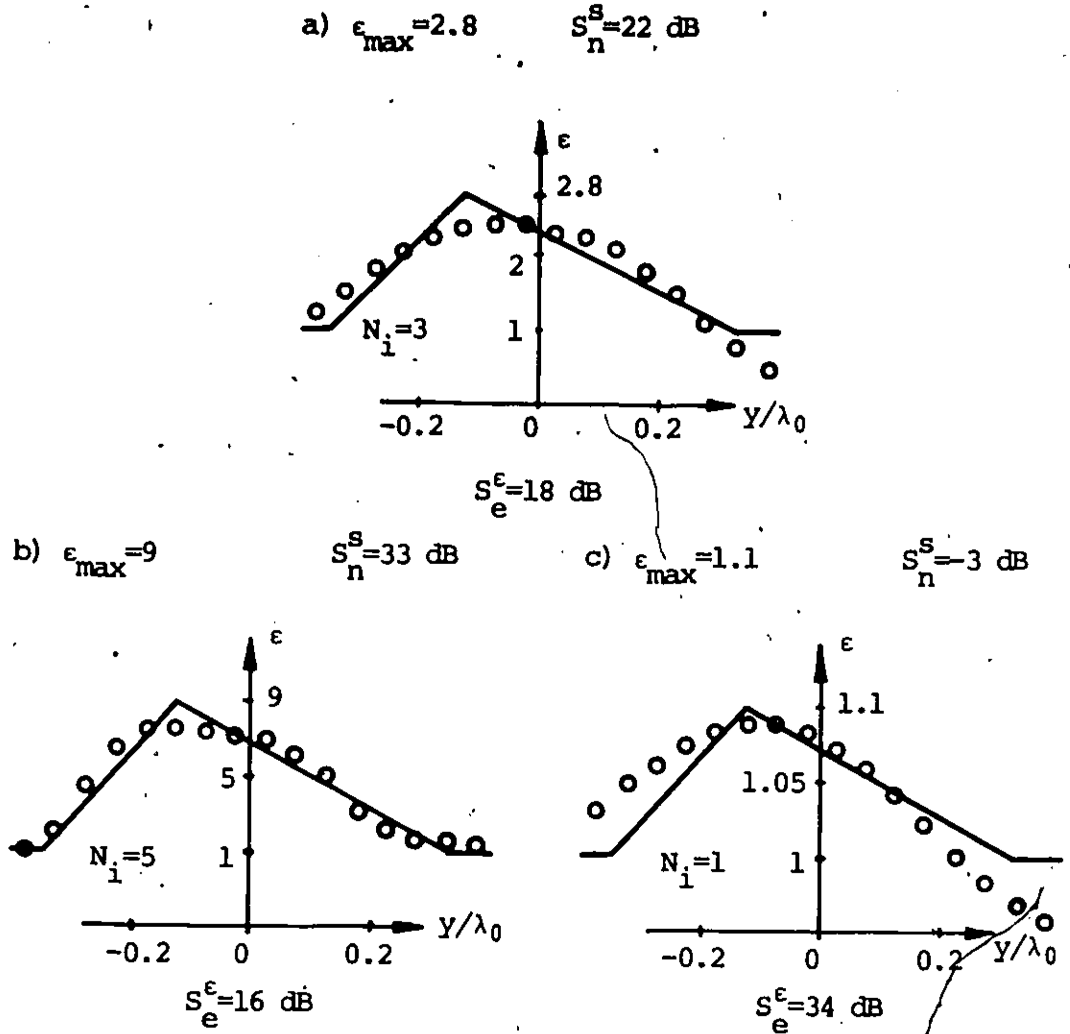

Figure 16: Reconstruction fidelity vs. dielectric constant of the scatterer (effect of contrast).

The reconstruction of the real part of triangle-like dielectric distributions is shown for different dielectric constants (amplitude factors). The scales are adjusted to the same magnitude for the sake of comparison. The geometric parameters are $s=0.1\ \lambda_0$, $d=0.3\ \lambda_0$, $N=N_d=16$ and the noise level present in the input data is 10,000 ppm.
The fidelity of reconstruction is comparable in all cases but when an extremely low S_n^s is considered for the case shown in Fig. 16 c), better reconstruction fidelity is obtained for low original contrasts.

In conclusion, low-contrast dielectric distributions are better reconstructed than high-contrast ones for comparable signal-to-noise ratios in the measurements. However, low-contrast dielectric distributions scatter weakly and consequently low S_n^s values are obtained for a given incident wave amplitude, which results in severe band-limiting effects of the algorithm. Increasing the amplitude of the incident wave is inefficient since the level of reflections would increase correspondingly and no significant improvement in S_n^s would be achieved. Decreasing the contrasts by increasing the background permittivity[1] can be considered. For instance, this can be achieved by immersing the scatterer in a matching medium (in water for biological scatterers). However, relatively long wavelengths should be used because of the very high attenuation occuring in water at high frequencies.

4.6 SPATIAL FREQUENCY SPECTRUM OF THE ORIGINAL DISTRIBUTION

Due to the bandwidth limitation introduced by the pseudoinverse transformation, reconstructed dielectric distributions are, for a given geometry, distorted depending mainly on the noise level present in the measurements. Consequently, it is expected that the dielectric distributions with a wide spatial frequency spectrum will

[1]In this case, equations pertaining to the scattering theory must be modified.

be, for a given level of noise and geometry, subject to greater distortions. This is illustrated by Fig. 17 and 18 which show the reconstruction of three different dielectric-profile functions for $d=0.3\ \lambda_0$ and $0.15\ \lambda_0$, respectively. In Fig. 17, the value of $N_i=3$ severely limits the bandwidth of the algorithm for all cases considered. Signal-to-error ratios differ significantly despite comparable S_n^s values.

The reconstruction fidelity significantly improves when the detector array is located closer to the scatterer as shown in Fig. 18 . The signal-to-noise ratios in the measurements are comparable with the cases illustrated in Fig. 17 but S_e^ε improves by up to 11 dB. This is caused by a wider algorithm spatial frequency bandwidth resulting from higher N_i values selected for optimum reconstructions. The spacing between the detectors used in Fig. 18 is optimum and equal to $0.05\ \lambda_0$. This value was determined from the tests carried out in Section 3.3 (see Table 1 a)).

The effect of the number N_i of the column vectors of the matrix [T] taken as independent is shown in Fig. 19 . The reconstruction of the real part of a pulse-like dielectric profile is illustrated for noiseless input data. The best reconstruction is achieved when 14 out of 16 column vectors of the matrix [T] are taken as independent and is illustrated in Fig. 19 c). This demonstrates the band-limiting effect due to computational noise only and

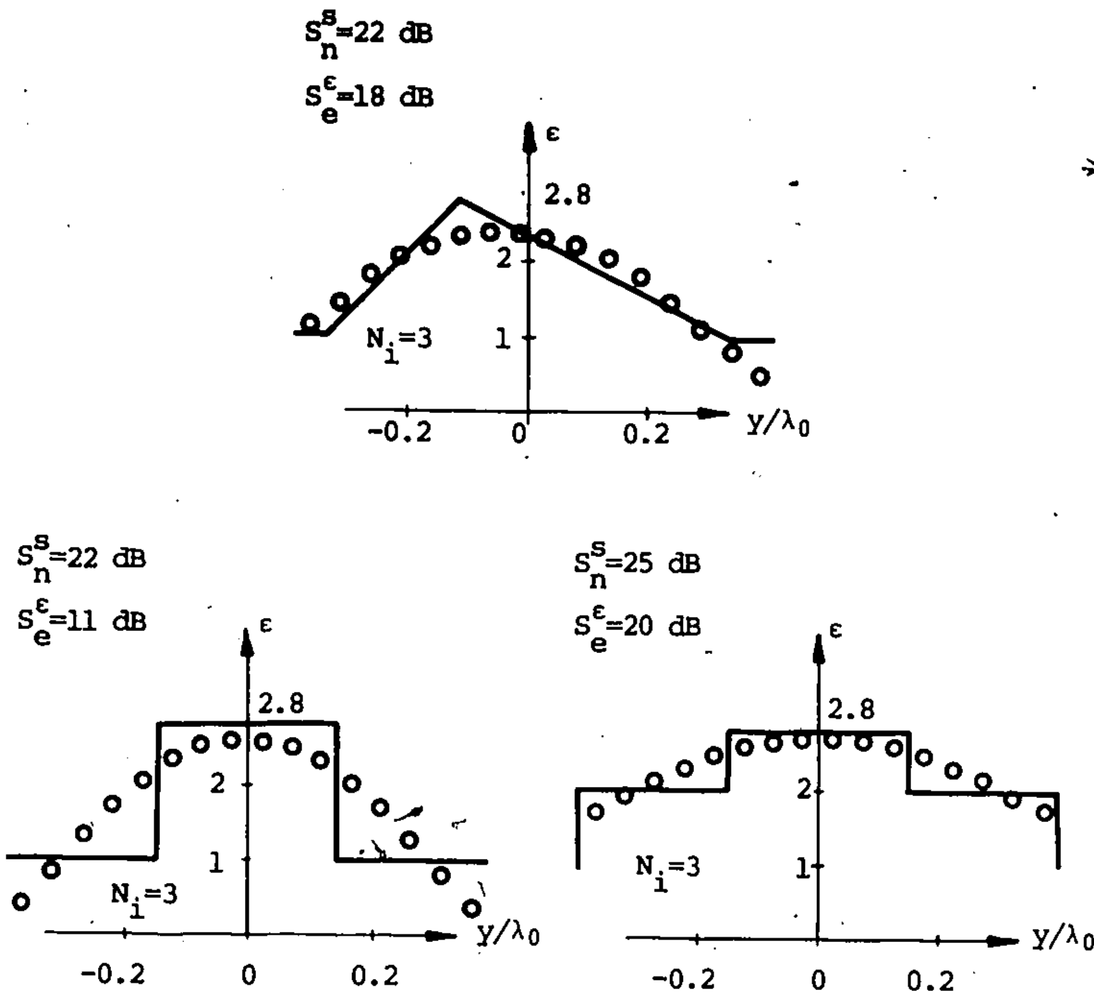

Figure 17: Reconstruction fidelity for different original dielectric-profile spatial frequency spectra ($d=0.3\ \lambda_0$).

The real part of the reconstructed dielectric profiles (circles) is shown for various original distribution functions (solid lines). The geometric parameters are $s=0.1\ \lambda_0$, $d=0.3\ \lambda_0$ and $N=N_d=16$. The noise level in the measurements is 10,000 ppm.
Severe distortion effects are visible for original dielectric distributions with a wide spatial frequency spectrum such as illustrated in Fig. 17 b) and c).

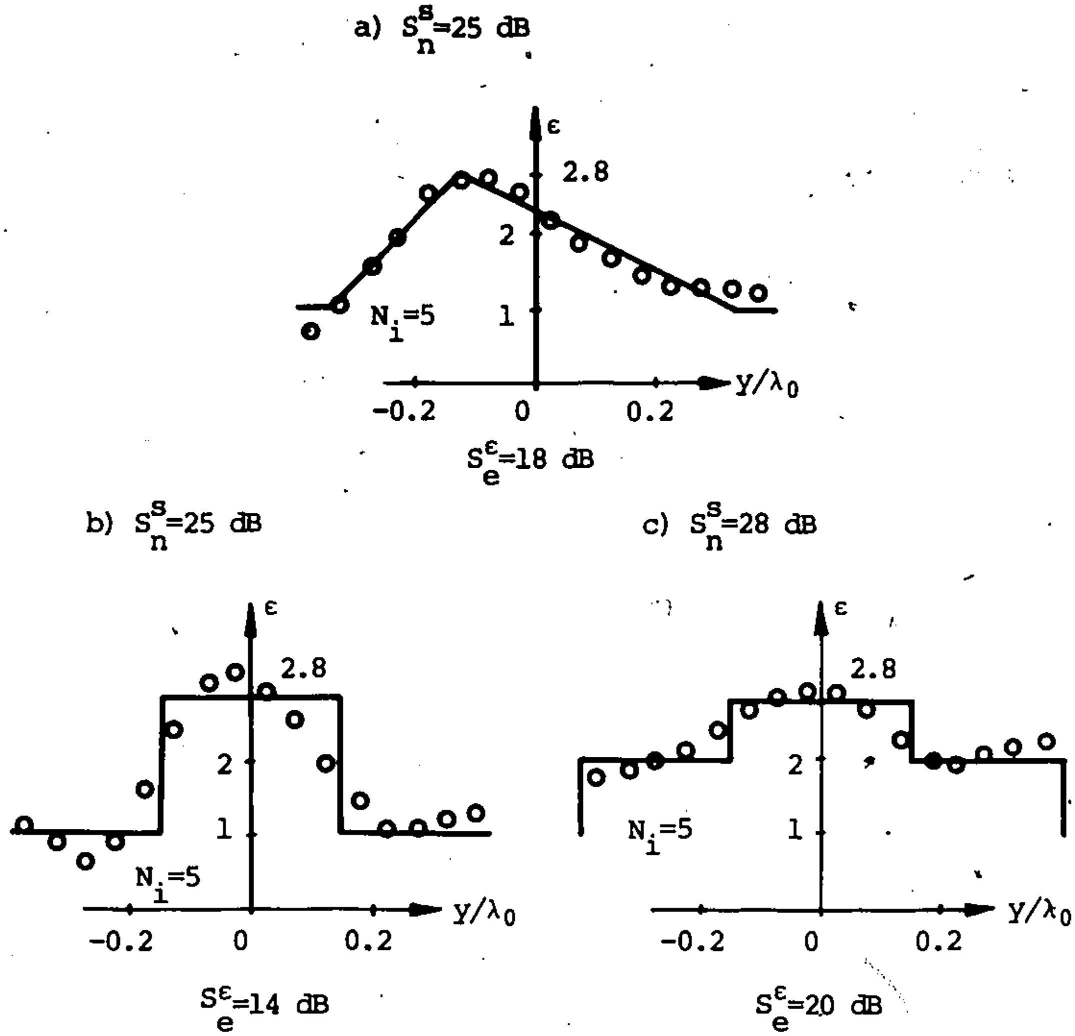

Figure 18: Reconstruction fidelity for different original dielectric-profile spatial frequency spectra ($d=0.15\ \lambda_0$).

The real part of the reconstructed dielectric profiles (circles) is shown for various original distribution functions (solid lines). The geometric parameters are $s=0.05\ \lambda_0$, $d=0.15\ \lambda_0$ and $N=N_d=16$. The noise level in the measurements is 10,000 ppm.
Comparison with Fig. 17 shows that the bandwidth of the algorithm improves when the array of detectors is located closer to the scatterer.

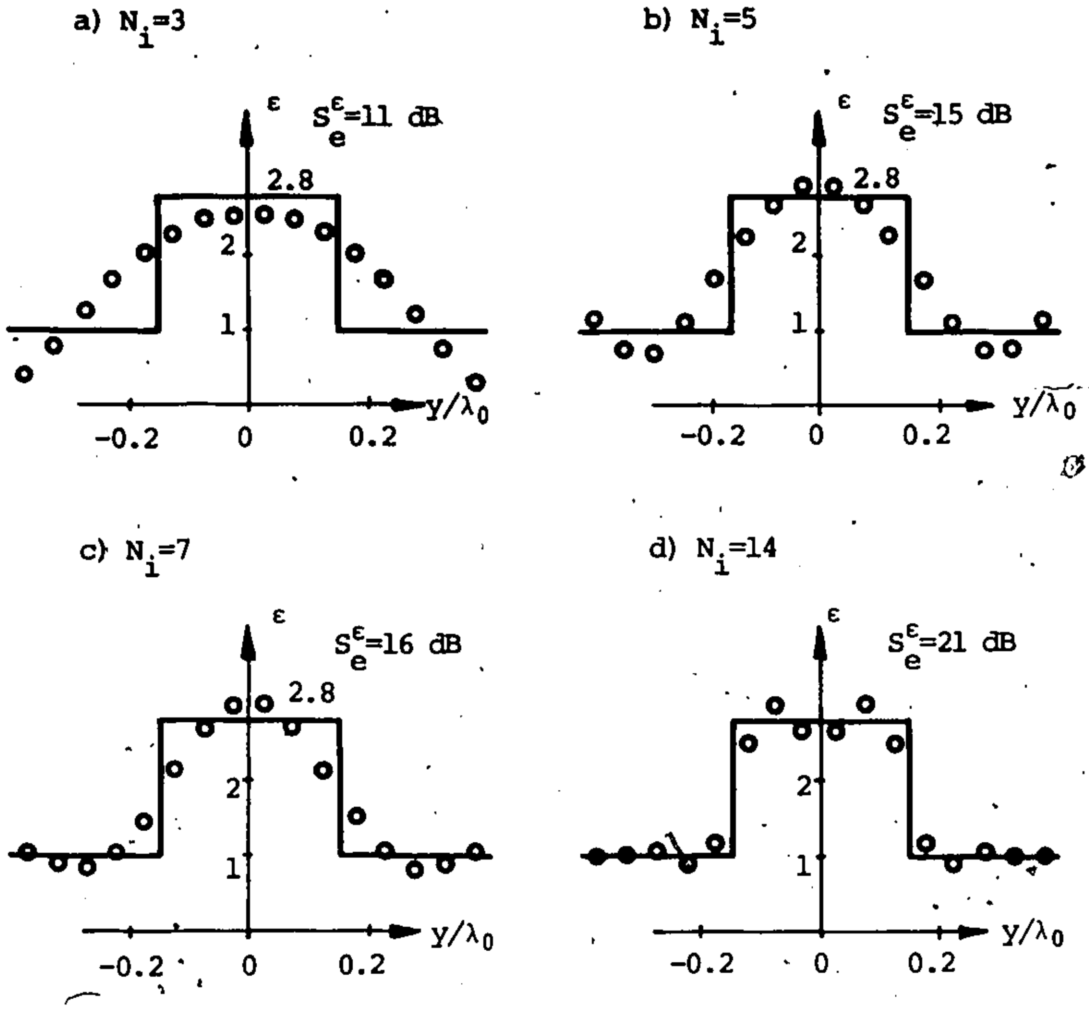

Figure 19: Reconstruction fidelity for pulse-like dielectric profiles for noiseless input data.

The real parts of reconstructed pulse-like dielectric profiles are shown for different numbers of column vectors of the matrix [T] taken as independent and for lossless input measurements.
The geometric parameters are $s=0.1\,\lambda_0$, $d=0.3\,\lambda_0$ and $N=N_d=16$.
The effect of computational noise can be observed in Fig. 19 d) which gives the best reconstruction with no noise in the input data.

reflects the degree of ill-conditioning of the matrix [T] for this geometry.

4.7 REDUNDANT DATA

The pseudoinverse transformation allows a minimum least-error solution even for a larger number of observation points than cells into which the scatterer cross-section is divided. It is expected that using redundant input data, one can improve the quality of the reconstruction. Indeed, the smallest least-error solution generated by the pseudoinvese transformation takes into account all components of the vector $[e^S]$. Using redundant data is, to some extent, similar to utilizing the data from different "projections".

Figure 20 shows the reconstruction of the asymmetric-triangle-like dielectric profile for two different numbers of detectors. There is no noticeable improvement in the reconstruction fidelity. The bandwidth of the algorithm turns out to be slightly wider for the case shown in Fig. 20 a), although N_i values are the same for both cases. This is due to the fact that the matrices [T] are different and the same N_i value does not necessarily yield the same spatial frequency bandwidth limitation. The addition of redundant observation points does not change the degree of dependence of the column vectors of the matrix [T] for this geometry. The failure of obtaining a significant

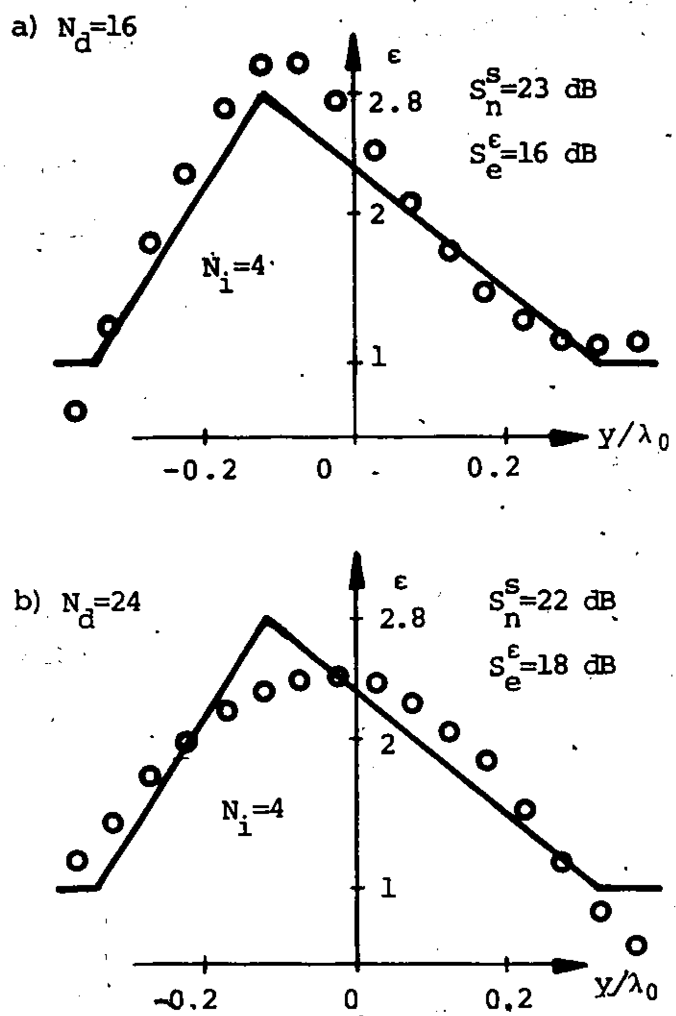

Figure 20: Reconstruction of an asymmetric-triangle-like dielectric profile using redundant data.

The real part of the dielectric-profile reconstruction is shown in two cases :
a) N_d=16 observation points.
b) N_d=24 observation points.
The geometric parameters are $s=0.01\ \lambda_0$, $d=0.15\ \lambda_0$, N=16, and the noise level is 10,000 ppm.

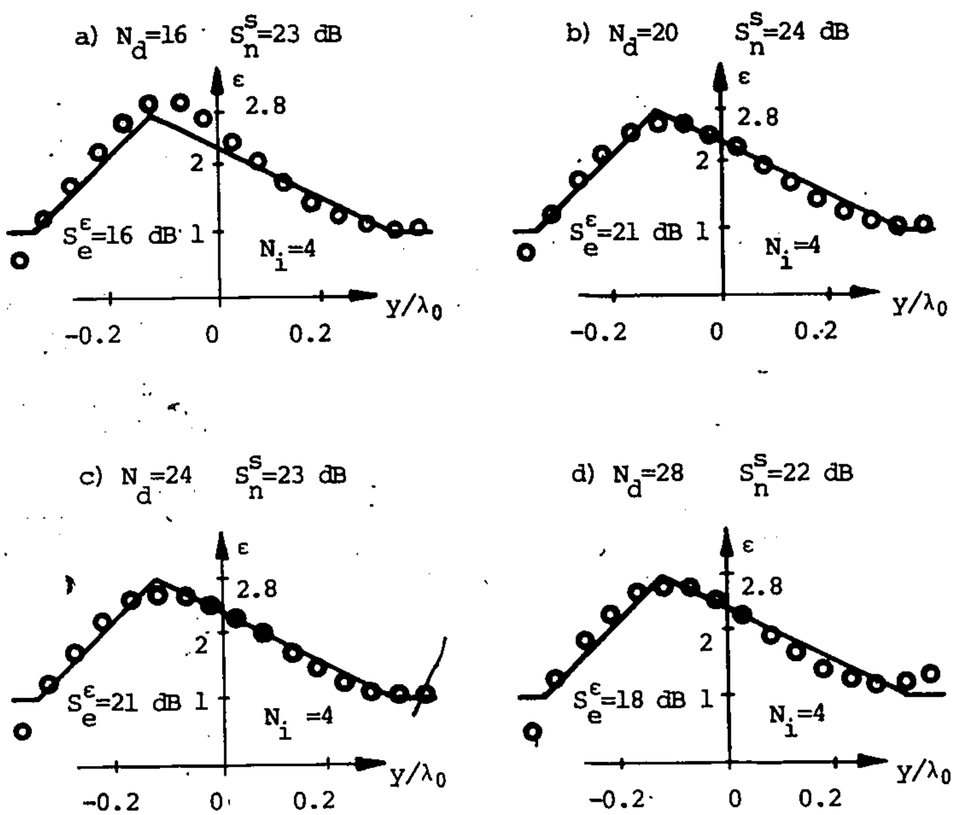

Figure 21: Dielectric-profile reconstructions for different numbers of detectors.

The real part of the dielectric-profile reconstruction is shown for different numbers of detectors located on two parallel arrays.
The geometric parameters pertaining to the first array are $d=0.015\ \lambda_0$, $s=0.01\ \lambda_0$, N=16 for all cases.
The geometric parameters for the second array are $d=0.02\ \lambda_0$, $s=0.015\ \lambda_0$.
The noise level is 10,000 ppm.

improvement by using redundant data, can be explained by the fact that the detectors bearing the redundant information, are located at the extremities of the array and consequently far away from the scatterer. In Fig. 21, the redundant observation points are located on a linar array, placed parallel to the y-axis at a distance of 0.02 λ_0 from the origin of the coordinate system. An improvement as great as 5 dB is obtained by using 20 or 24 detectors. However, for N_d=28 the value of S_e^ε decreases. Again, the geometry of the detectors may play a significant role. For a number of redundant observation points as large as 28, the 4 extra detectors (relative to the case N_d=24), should be placed in some other locations for which the geometry would be optimum. Some numerical problem may also be considered, due to the relative increase of the size of the matrices.

4.8 CROSS-SECTION DIVIDED INTO MORE CELLS

For rapidly varying dielectric distributions, dividing the cross-section into a larger number of cells may improve the reconstruction fidelity. Care must be taken to satisfy the condition (2.33) pertaining to the size of the cells. It was found [37,38] that the shape of the cells does not play an important role in scattered field calculations. Therefore, it is possible in the present case to subdivide the cylinder cross-section into more than 16 cells. It was verified that 25 (0.05x0.032 λ_0) rectangular cells yielded scattered field values within 0.1 per cent of the ones calculated with 16 cells. This is well within uncertainties resulting from the noise in the measurements for the inverse process.

Figures 22 a) and b) show the reconstruction of the real part of a pulse-like dielectric profile for N=16 and N=25, respectively. The level of noise is 10,000 ppm and S_n^s values differ by 1 dB. There is no significant increase in the reconstruction fidelity when the scatterer cross-section is divided into more cells for this geometry. This can be explained by the same number of independent column vectors (N_i=5 in both cases) of the matris [T] required for optimum reconstruction. Sampling the scatterer cross-section with more cells implies a reduction of the cell size. Consequently, the degree of ill-conditioning of the matrix [T] increases. Indeed, there are 5 out of 16 independent column vectors in the case N=16, whereas only 5 out of 25 should be considered as independent in the case of N=25. Therefore, dividing the cylinder cross-section into more cells does not give any advantage unless a detector configuration is found such that a higher number of independent column vectors can be selected. An increase in the size of matrices involved in the algorithm does not seem to affect the fidelity of the reconstruction. However, there is a potential advantage in using a larger number of cells (consequently a larger number of observation points),

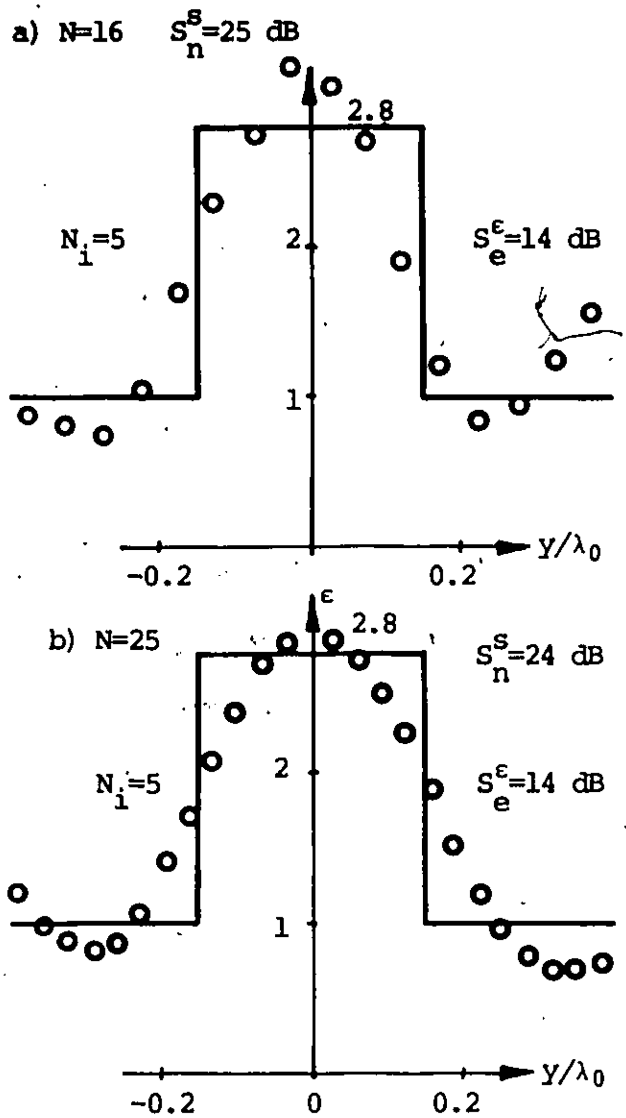

Figure 22: Reconstruction of the pulse-like dielectric profile for N=25.

The real part of the reconstructed dielectric profile is shown for two different numbers of cells of the scatterer cross-section (cell size : $0.05 \times 0.032 \lambda_0$). The geometric parameters pertaining to the detector location are $s=0.05\ \lambda_0$, $d=0.15\ \lambda_0$, $h=0.032\ \lambda_0$, $N_d=25$ and the noise level is 10,000 ppm.

that improves the efficacy of additional filtering of both the scattered field values and the reconstructed dielectric profiles.

4.9 ADDITIONAL FILTERING

Additional filtering may improve the reconstruction fidelity in certain cases. The first possible filtering can be introduced by truncating the reconstructed dielectric constant values below or above certain thresholds. In practical situations, the maximum and minimum possible values of the dielectric constant are generally known a priori. As mentioned previously, the pseudoinverse transformation is essentially equivalent to low-pass filtering and severely distorts wide spatial frequency spectrum dielectric distributions. A method known as the Median Window Restoration (MWR) technique conserves steps but obliterates oscillations with a period less than half the window length [51,52]. This technique is based upon the following scheme : The sampled values within a window centered at the point under consideration, are sorted in increasing or decreasing order. The best estimate of the sample under consideration is taken as the value at the mid-location in the window (after sorting).

To evaluate the effectiveness of the MWR technique, different dielectric-profile reconstructions were performed for N_i values selected on the plateau which occurs on the

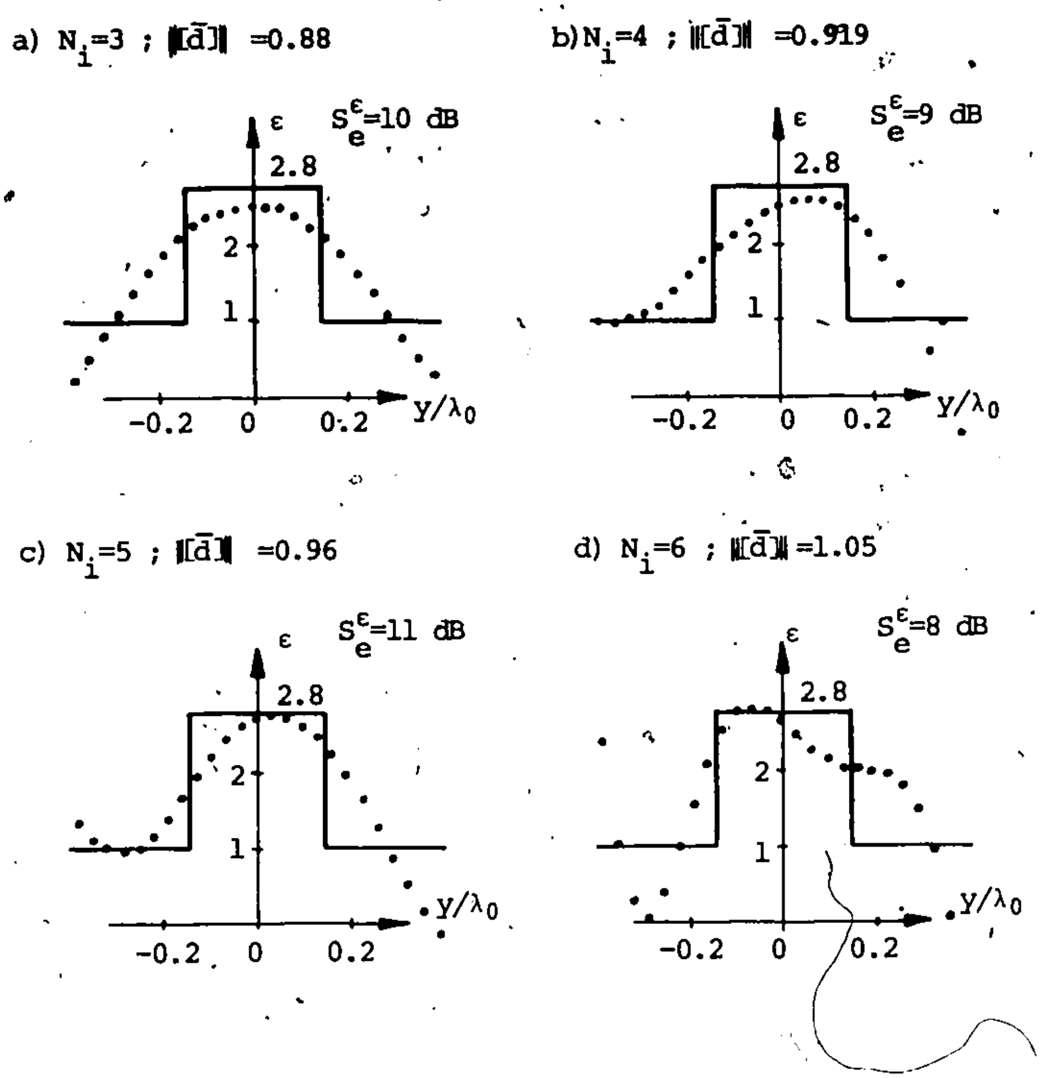

Figure 23: Pulse-like function reconstructions for various N_i.

The real part of the reconstructed pulse-like dielectric profile is shown for different selections of the number of independent column vectors of the matrix [T]. These N_i values are located on the plateau occuring in the characteristic ‖[d̄]‖-vs.-N_i (ref. Fig. 10). The geometric parameters are $s=0.1\ \lambda_0$, $d=0.3\ \lambda_0$ and $N=N_d=25$. The noise level present in the input data is 10,000 ppm (S_n^s=21 dB).
Higher spatial frequency components are visible when N_i increases.

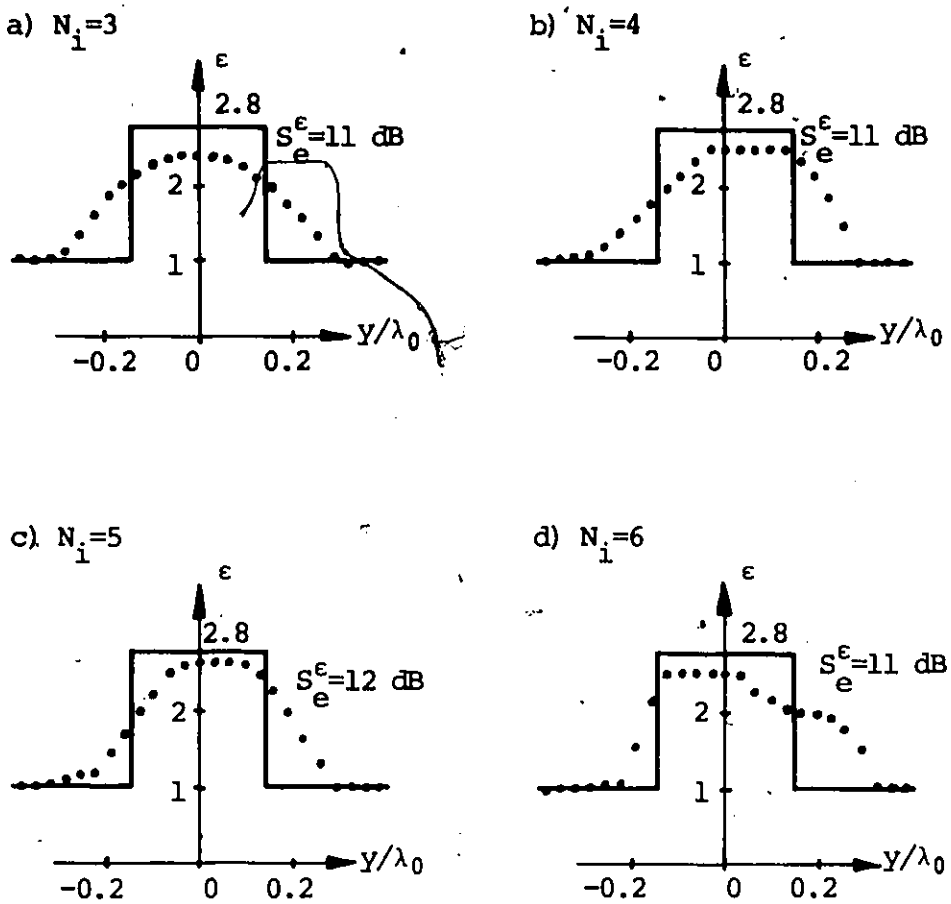

Figure 24: Reconstructed dielectric profiles with post-Median Window Restoration.

The reconstructed profiles of Fig. 23 are filtered using the MWR techniques. This nonlinear filtering conserves steps but removes high spatial frequency oscillations. The best reconstruction fidelity still occurs for N_i=5 after filtering (see Fig. 24 c)).

characteristic $\|[\bar{d}]\|$-vs.-N_i (see. Fig. 10). These reconstructions are illustrated in Fig. 23 . Some oscillations are evident when N_i becomes larger. Generally, the MWR filter is, for a given window length, effective for images containing large high spatial frequency components. This suggests the selection of even larger N_i values. However, for N_i greater than 6, the reconstructed values diverge completely resulting in a S_e^{ε} value below -20 dB in the case under consideration. This corresponds to a N_i value beyond the sharp turning point in the characteristic illustrated in Fig. 10 . For a such low S_e^{ε}, filtering techniques are difficult to apply without removing the usefull information.

Figure 24 illustrates the reconstructed profiles shown in Fig. 23 after MWR filtering with a window length equal to 9. In order to avoid additional distortions caused by edge effects, the knowledge of dielectric constant values outside the scatterer cross-section is utilized in such a way that the reconstructed sampled dielectric profile is extended by a half of the window length on each side with the background permittivity values. There is a slight improvement (1 dB) in the reconstruction fidelity (Fig. 24 c)) as compared with the best nonfiltered reconstruction shown in Fig. 23 c). These results are not exceptional but they show that the selection of N_i values on the plateau of the characteristic displayed in Fig. 10 may have a great influence on the reconstruction fidelity.

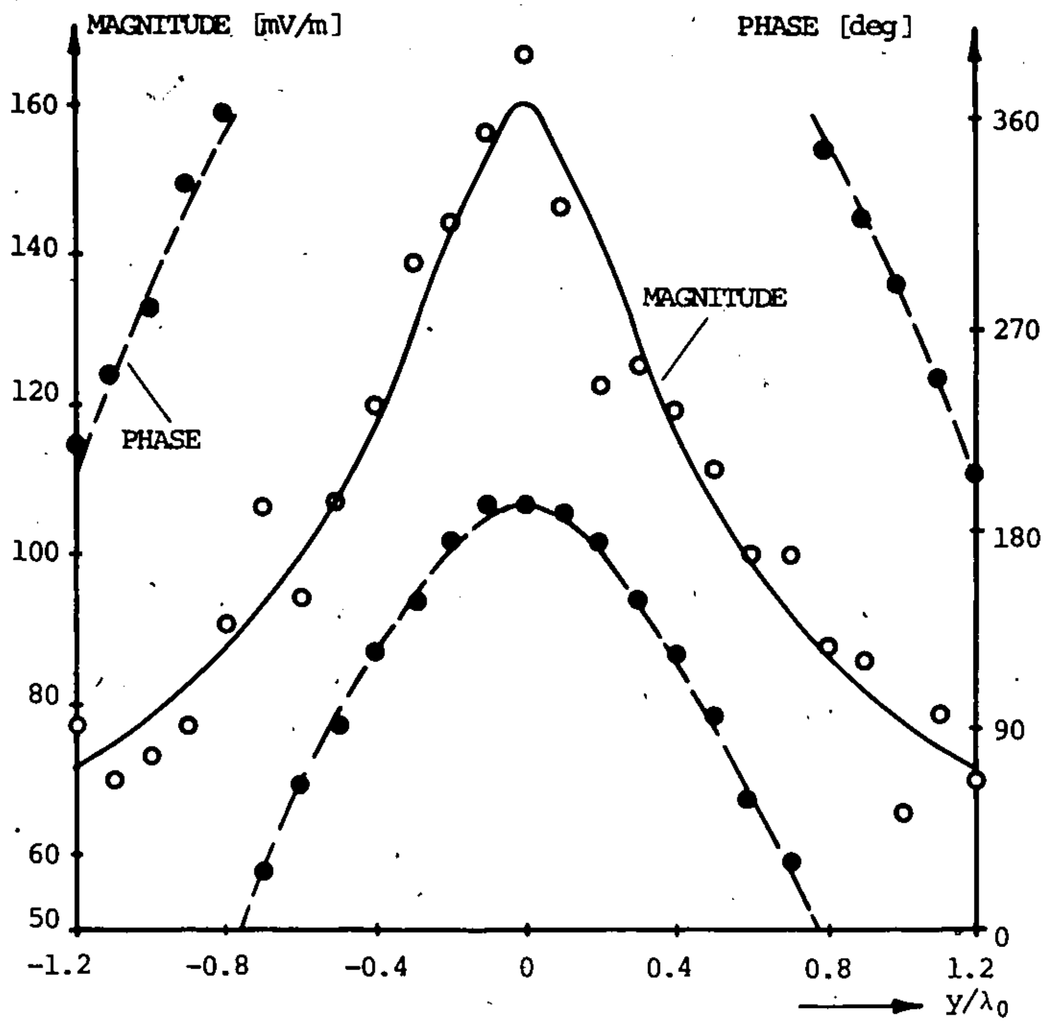

Figure 25: Phase and magnitude of the scattered field pertaining to the cases illustrated in Fig. 23 and 24 .

Phase and amplitude of the scattered field along the detector array computed using the moment method. Dots and circles represent the detector position. Solid and broken lines represent the magnitude and phase of the noiseless scattered field, respectively.
Geometric parameters are the same as the cases illustrated in Fig. 23 and 24 : $s=0.1\ \lambda_0$, $d=0.3\ \lambda_0$ and $N=N_d=25$.
The noise level is 10,000 ppm (relative to 1 V/m) corresponding to $S_n^s=21$ dB.

Other improvements in the reconstruction fidelity can be achieved by considering the scattered field phase and magnitude values measured by the detectors depicted in Fig. 25 . In practice, the phase and magnitude of the total field would be recorded and presented in a form of complex numbers. Then, the incident field values would be subtracted from the measured values yielding the noisy scattered field. Drawing real and imaginary parts of the scattered field as a function of the detector location would result in similar characteristics as those shown in Fig. 25. Obviously there are higher spatial frequency components in the measured fields than in the noiseless scattered fields. Therefore, some filtering is justified in order to increase S_n^s before applying the reconstruction algorithm. A simple low-pass filtering of the experimental data is generally sufficient to improve S_n^s appreciably, especially for low original S_n^s values. Low-pass filtering of the measured data illustrated in Fig. 25 yielded 5 dB improvement in the S_n^s value.

Figure 26 a) reveals an improvement in the reconstruction fidelity obtained by filtering the scattered field values before applying the reconstruction algorithm. There is a 3-dB increase in the S_e^ε value as compared with the case illustrated in Fig. 23 c). Subsequently, MWR filtering with a window length equal to 9 was performed yielding an additional 1-dB increase in the S_e^ε value as shown in Fig. 26 b).

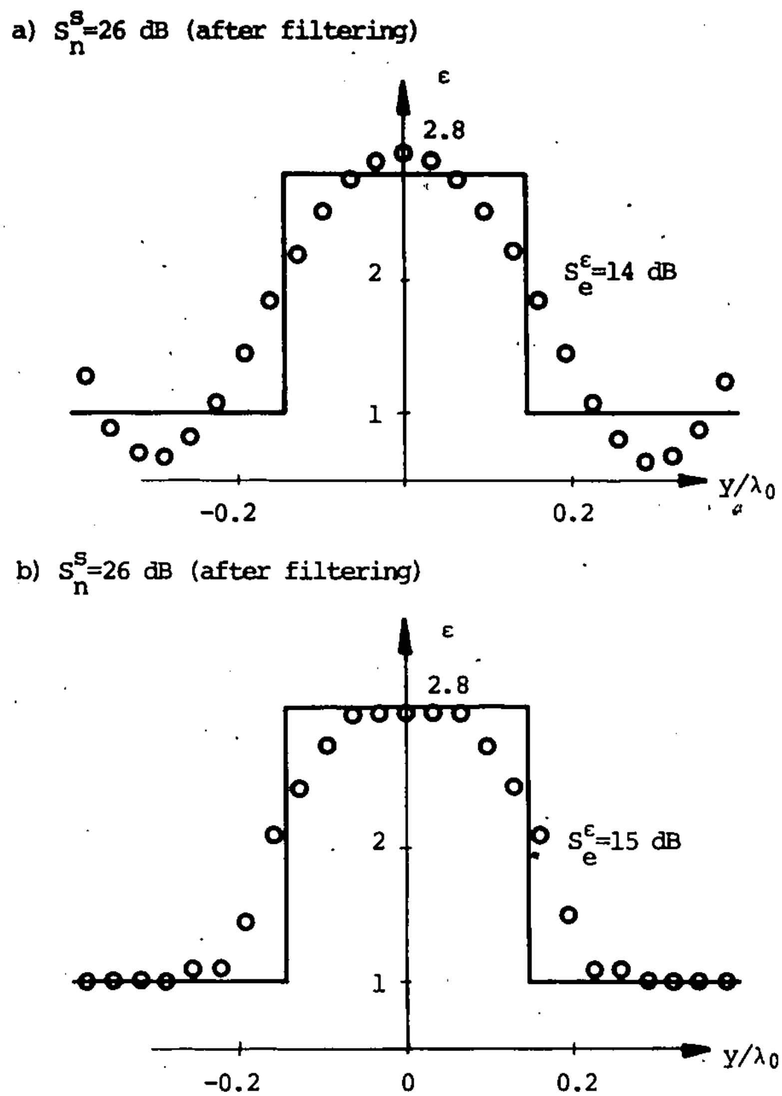

Figure 26: Low-pass filtering of the input data followed by MWR filtering of the reconstructed profile.

The real part of the reconstructed pulse-like dielectric profile is illustrated.
a) measured scattered field values are low-pass filtered yielding an improvement of 3 dB in the S_e^ε value.
b) the reconstructed profile (Fig. 26 a)) is filtered using the MWR technique, resulting in an additional improvement of 1 dB in the S_e^ε value.
The geometric parameters are the same as for the cases illustrated in Fig. 23 and 24 : $s=0.1\,\lambda_0$, $d=0.3\,\lambda_0$ and $N=N_d=25$. The noise level is 10,000 ppm corresponding to S_n^s=21 dB before input data filtering.

The objective of this section was to demonstrate that filtering can be performed on both the measured scattered field and the reconstructed values of the dielectric constant in conjunction with the algorithm using the pseudoinverse transformation. More sophisticated filtering techniques are available and may provide further improvement in the reconstruction fidelity. These methods however, will not be discussed here.

4.10 LOSSY SCATTERER

The method presented here also allows one to reconstruct lossy structures. In this case the permittivity has a non-zero imaginary part pertaining to the lossy character of the dielectric medium. The condition (2.33) should be written for the general case :

$$b_j > 2/|k| \; . \tag{4.1}$$

In lossy media, the wave number is given by :

$$k=[j\omega\mu_0(\sigma+j\omega\varepsilon_0\varepsilon')]^{1/2} , \tag{4.2}$$

where μ_0 is the vacuum magnetic permeability, ε' the dielectric constant and σ the conductivity of the lossy dielectric which is given by :

$$\sigma = \omega \varepsilon_0 \varepsilon'' , \tag{4.3}$$

where ε'' is the imaginary part of the relative permittivity called the relative loss-factor.

A reconstruction of a thin slab of human fat in shown in Fig. 27 . The permittivity of the human fat was taken from [53]. The resulting wave factor is practically the same as that of lossless medium for the incident wave frequency of 3 GHz, indicating small attenuation in the medium. For $d=0.3\ \lambda_0$, spatial oscillations with relatively high amplitude appear in the reconstruction of the loss factor whereas the real part of the dielectric constant distribution exhibits the same type of spatial bandwidth limitation as for the lossless cases. These oscillations are attenuated when the detector array is placed closer to the scatterer as shown in Fig. 27 b). The optimum value of N_i is identical in both cases illustrated in Fig. 27 . However, different reconstruction fidelities are obtained because the matrices [T] are different. The S_e^{ε} is slightly larger (by 3 dB) for the case in Fig. 27 b) than in Fig. 27 a). The criterion for selection for N_i values pertains to the one that yields the best S_e^{ε} value which is calculated by taking the rms value of the relative permittivity.

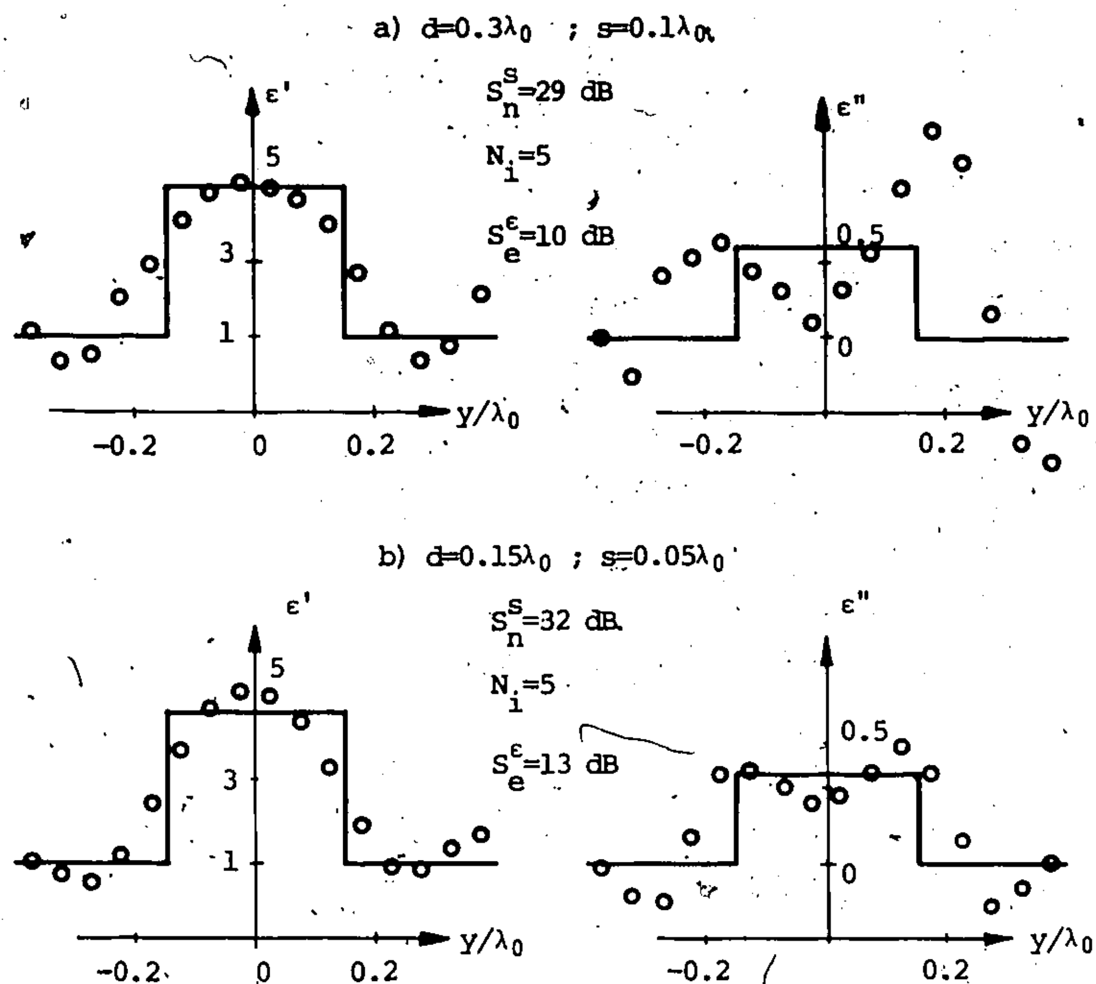

Figure 27: Reconstruction of a thin slab of human fat.

The reconstructed real and imaginary parts of the permittivity of a thin slab of human fat are shown for two different detector array locations. Other geometric parameters are $N=N_d=25$. The relative noise level is 10,000 ppm.
The values of $\varepsilon'=5$ and $\varepsilon''=0.6$ ($\sigma=0.1$ S/m) are taken from [53].

4.11 EVALUATION OF THE SYSTEM SPATIAL RESOLUTION

In this section, the spatial resolution of the reconstruction algorithm is evaluated. First, a test to determine the two-point spatial resolution of the method is defined. Then, a criterion to evaluate quantitatively the spatial resolution is clearly stated to provide a possible comparison with other methods. The test consists of reconstructing two rods of the dimensions of the cells, with a dielectric constant equal to 2.8 (lossless) and separated by a certain distance (taken from center to center). The criterion to evaluate the two-point spatial resolution, relative to the test previously described, is the minimum distance for which the two rods (they may be distorted) are reconstructed with all other spurious oscillations or artifacts amplitude at least 50 per cent (3 dB) below the peak amplitude of both reconstructed rods (evaluated relative to the background permittivity i.e. $\varepsilon=1$)[1].

Theoretically, the spatial resolution of the algorithm should be of the order of the cell size into which the scatterer cross-section is divided. However, the first limitation results from computational noise which gives rise to some spatial frequency bandwidth limitations and consequently decreases the spatial resolution of the

---

[1]In image processing, the resolution is defined as the degree of discernable detail [55]. This criterion may be subjective and a comparison between different methods may be difficult.

algorithm. In addition, one cannot ignore an additional noise which is always present in the measurements and which further reduces the algorithm spatial resolution capability.

Figures 28 and 29 show the reconstruction of two dielectric rods (ε=2.8) separated by a distance of 0.5 λ_0 and 0.2 λ_0 respectively, for four different noise levels. A 0.5-λ_0 two-point spatial resolution is feasible for S_n^s values larger or equal to 10 dB, when the detector array is placed at distances within 0.1 λ_0 from the scatterer cross-section as shown by Fig. 28 a). As mentioned before, some practical difficulties may arise due to the proximity of some of the detectors, which would result in a coupling effect with the scatterer and produce some additional errors in the measurements.

A spatial resolution of 0.2 λ_0 is feasible for S_n^s above 35 dB as shown in Fig. 29 b). For lower signal-to-noise ratios in the measurements, Fig. 29 a) illustrates that the algorithm is not capable of detecting the two rods as separate elements. The signal-to-noise ratio in the measurements significantly affects the spatial resolution capability of the algorithm. Less significant, but not negligible, is the computational noise which also contributes to the band-limiting effect of the pseudoinverse transformation. For instance, Fig. 28 c) and 29 c) illustrate the band-limiting effect due to computational noise only, demonstrating that the maximum theoretical

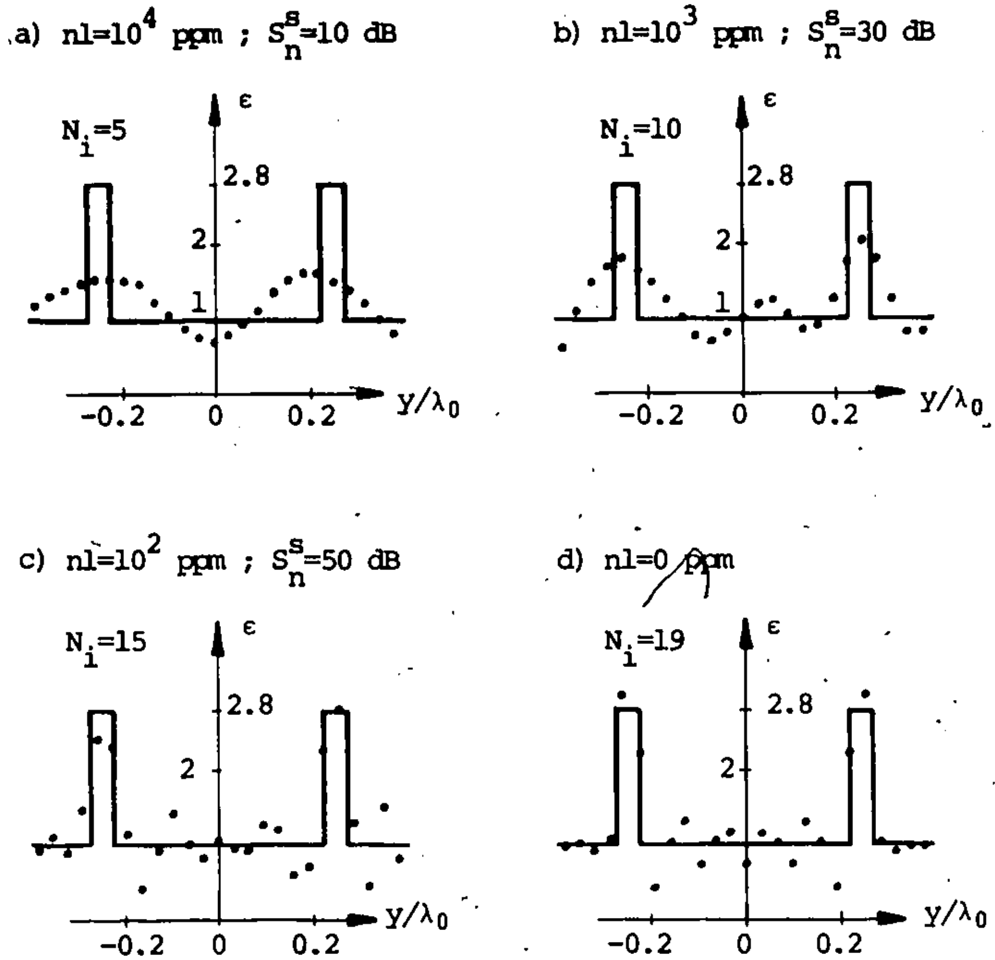

Figure 28: Reconstruction algorithm capability of detecting two dielectric rods distant by 0.5 λ_0 as separate elements.

The reconstruction of two 0.05x0.05-λ_0 dielectric rods (ε=2.8) separated by a distance of 0.5 λ_0 is shown for four different noise levels.
The geometric parameters are s=0.05 λ_0, d=0.1 λ_0 and $N=N_d=25$. Fig. 28 c) shows the effect of computational noise only.
A two-point spatial resolution of 0.5 λ_0 is feasible for S_n^s larger or equal to 10 dB.

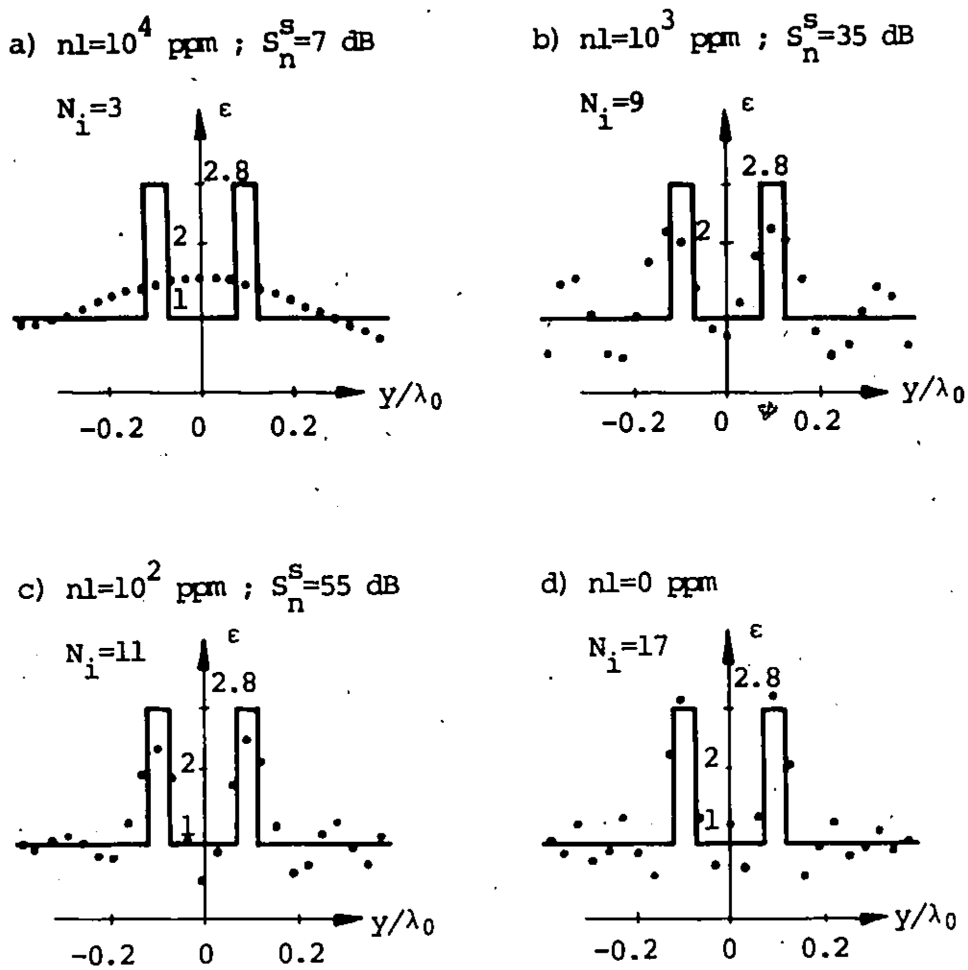

Figure 29: Reconstruction algorithm capability of detecting two dielectric rods distant by 0.2 λ_0 as separate elements.

The reconstruction of two 0.05x0.05-λ_0 dielectric rods (ε=2.8) separated by a distance of 0.2 λ_0 is shown for four different noise levels. The geometric parameters are the same as those in Fig. 28 . A spatial two-point resolution of 0.2 λ_0 is feasible for S_n^s values larger or equal 35 dB.

spatial resolution capability of the algorithm (cell size) may not be realized.

The resolution capability of the algorithm may be augmented by filtering the input data. However, because of the wide spatial frequency spectrum of the original profiles illustrated by solid lines in fig. 28 and 29, filtering after reconstruction would be very difficult.

One can conclude that according to the criterion defined before, the algorithm yields a spatial resolution capability of at least 0.5 λ_0 for realistic signal-to-noise ratios in the measurements (10 dB), when the detector array is located at 0.1 λ_0 from the scatterer. It was stated in [54] that for separations equal to or larger than 0.1 λ_0 the coupling between the detectors and the scatterer can be neglected.

The spatial resolution of the algorithm was evaluated by sampling the space in one dimension. Two-dimensional spatial resolution of the algorithm is investigated in the next point.

4.12 SIMULATION GEOMETRY (2-D CASE)

The properties of the reconstruction algorithm revealed in the previous sections, are expected to remain similar for the two-dimensional case. For instance, there is an optimum configuration of the detectors and the detectors have to be placed as close as possible to the scatterer in order to have optimum conditions for reconstruction. However, the two-dimensional grid that represents the scatterer cross-section (see Fig. 30) suggests that the detectors should not form a linear array but rather a circular array centered in the origin of the coordinate system. This, rather intuitive reasoning, pertains to the fact that with a linear array a significant number of detectors would be at remote locations (those which are close to the end of the array) and that would effectively increase the degree of ill-conditioning of the matrix [T]. Two-dimensional dielectric distributions generally imply a larger number of cells. Consequently, the size of the matrices increases significantly and some problems related to memory size and computational noise begin to appear.

The simulation geometry for two-dimensional dielectric-distribution reconstructions is shown in Fig. 30. The scatterer cross-section is divided into 64 0.1×0.1-λ_0 square cells. This implies a manipulation of 64x64 matrices. On each circular array centered at the origin of the coordinates and located at a distance of 0.8 and 1.0 λ_0, respectively, 32 detectors record phase and amplitude of the diffracted field. The cylinder is irradiated by a plane wave (1 V/m peak amplitude) propagating along the x-axis. No detectors are located closer than 0.1 λ_0 from the scatterer to prevent any significant coupling effects.

The procedure for two-dimensional-dielectric-distribution reconstructions is identical to the one described in Section

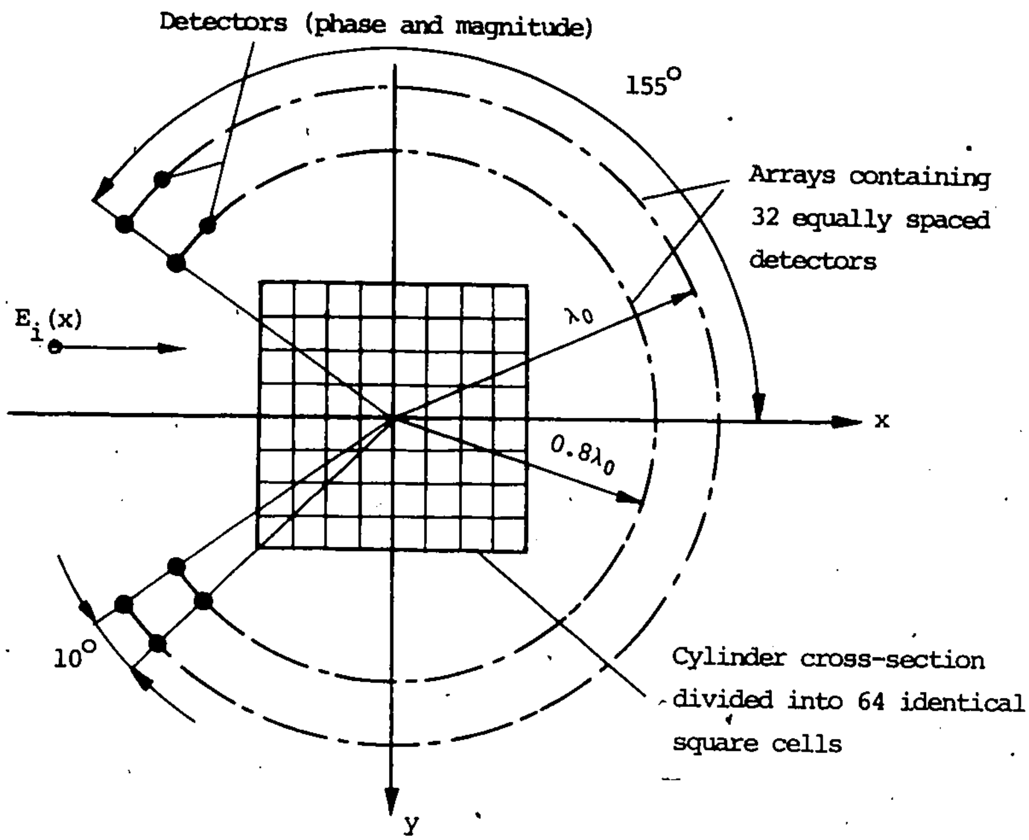

Figure 30: Simulation geometry for the two-dimensional case.

A plane wave with 1-V/m electric field peak amplitude and a wavelength λ_0, propagates along the x-direction and irradiates a dielectric cylinder with a square cross-section ($0.8 \times 0.8\ \lambda_0$) which is divided into 64 cells $0.1 \times 0.1\ \lambda_0$. Two concentric circular arrays containing 32 equally spaced detectors each are located at a distance of 0.8 and 1.0 λ_0 from the origin of the coordinates, symmetrically with respect to the x-axis.

4.1 . Because of the relatively large size of the matrices involved in the computations and the numerous possibilities to arrange the detectors, only limited tests to determine an optimum geometry were performed by varying the spacing between the detectors. Consequently, reconstructions are not necessarily performed in optimum conditions which may result in some limitations in the algorithm performance.

4.13 SOME EXAMPLES OF TOMOGRAPHIC VIEW RECONSTRUCTIONS

In this section, some examples of dielectric-distribution reconstructions (tomographic views) are presented for the original distributions illustrated in Fig. 31 . In order to obtain finer three-dimensional representations of the various distributions, the original 8x8 grids are linearly interpolated and transformed to 15x15 grids.

Figure 32 shows the reconstructed dielectric distributions of the sine-square-like and the pulse-like dielectric constant distributions for two different levels of noise. For smooth dielectric distributions a relatively good reconstruction fidelity can be obtained even for a relative noise level as high as 100,000 ppm. In this case the number of independent columns N_i is equal to 4 (for an optimum reconstruction) which indicates a strong limiting effect on the spatial-frequency bandwidth of the algorithm. However, for narrow-band original frequency spectra, distortions due to band-limitation are not significant. On

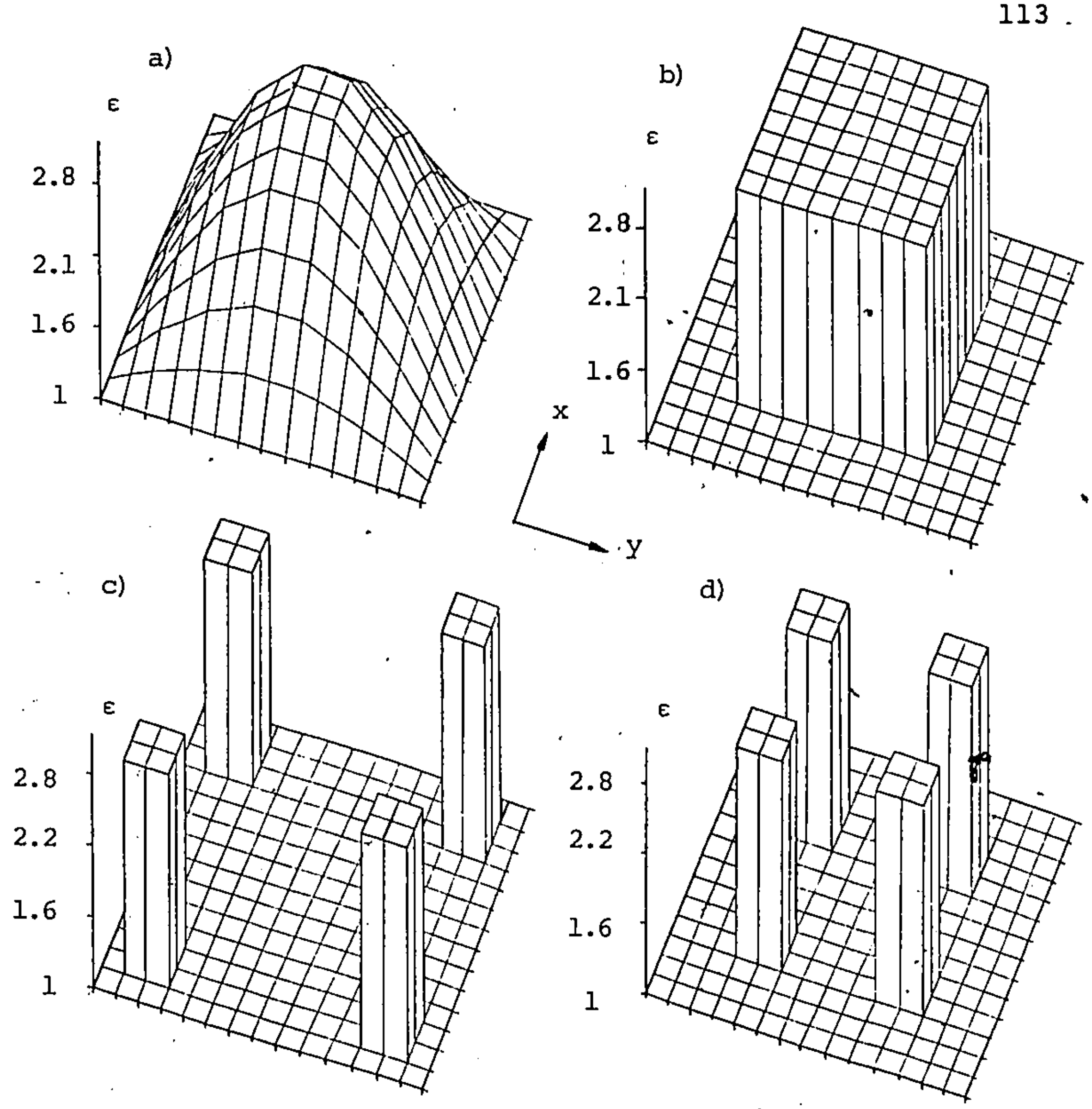

Figure 31: Original two dimensional dielectric distributions.

Four different original dielectric distributions are :
a) Sinus-square-like dielectric distribution.
b) Pulse-like dielectric distribution.
c) Four rods separated by 0.5 λ_0.
d) Four rods separated by 0.3 λ_0.
The peak amplitude of all dielectric distributions is 2.8 (lossless cases). Odd lines parallel to both x and y-axis indicate the position of the center of the cells of the original 8x8 grids. The distance between grid lines is 0.05 λ_0.

the other hand, the band-limiting process severely distorts the pulse-like dielectric distributions and some oscillations appear even for a relatively high signal-to-noise ratio in the measurements. Unfortunately, because of the relatively small number of cells, filtering turns out to be inefficient for rapidly varying dielectric distributions.

The criterion for evaluating the two-point spatial resolution of the algorithm was presented in Section 4.11 . For the two-dimensional case, however, the two-point resolution may be different depending upon the alignment of the rods with respect to the coordinate system. Consequently, the spatial resolution should be evaluated along the y and x-directions. Thus, the test consists of reconstructing four rods located at the corners of a square, as illustrated in Fig. 31 c) and d).

Figures 33 a) and b) show the reconstruction of four rods separated by a distance of 0.5 λ_0 and 0.3 λ_0 respectively, and for two values of N_i corresponding to the beginning and the end of the plateau on the $\|[\bar{d}]\|$-vs.-N_i characteristics. Figure 33 a) shows that a spatial resolution of 0.5 λ_0 is feasible in both directions. However, there is a stronger spatial bandwidth limitation in the y-direction than in the x-direction which corresponds to the direction of propagation of the incident wave. On the other hand, Figure 33 b) shows that a resolution of 0.3 λ_0 cannot be obtained

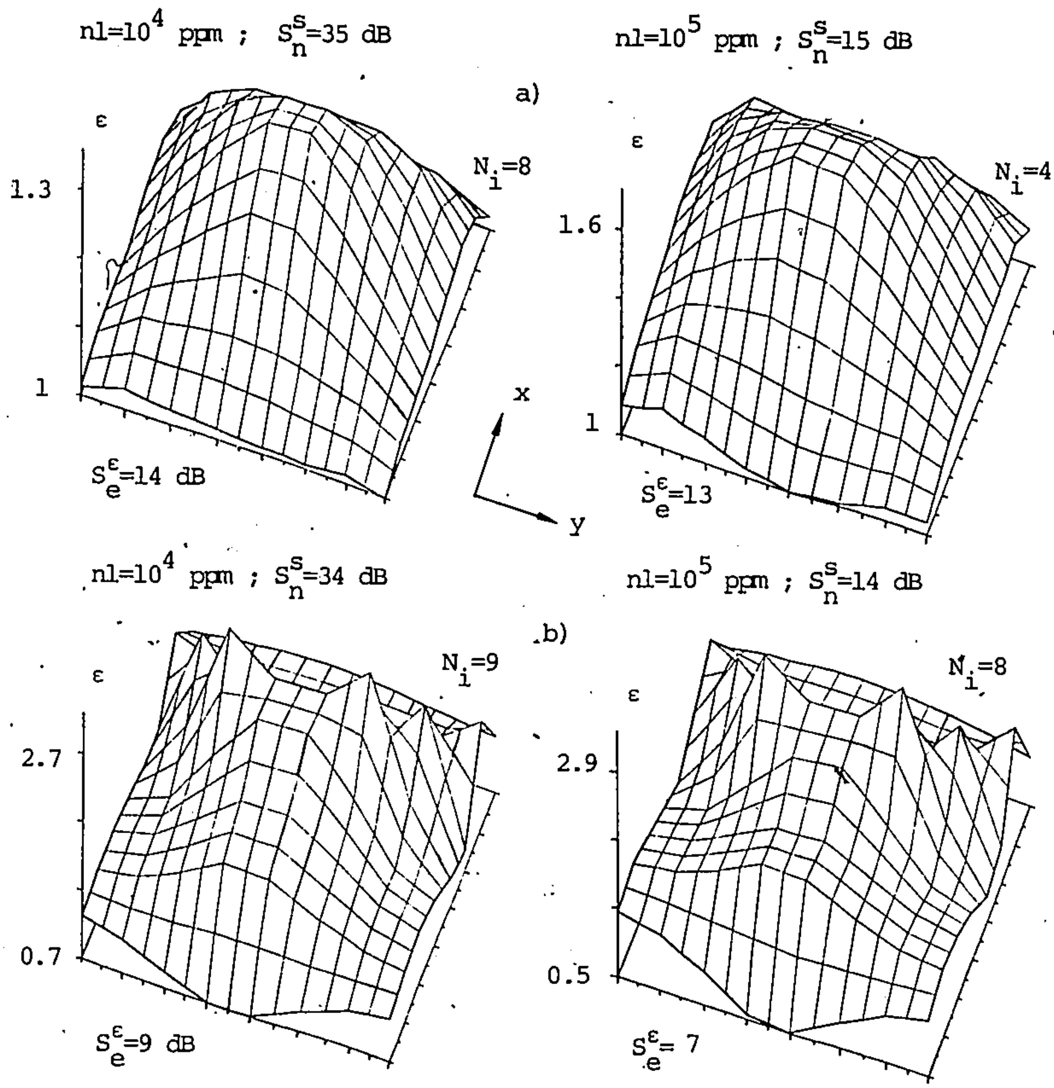

Figure 32: Reconstruction of sine-square-like and pulse-like dielectric distributions for two different levels of noise.

The reconstruction of the dielectric constant distribution represented in Fig. 31 a) and b), is illustrated in the case of two different levels of noise. The distance between grid lines is $0.05\ \lambda_0$.
a) sine-square-like distribution.
b) pulse-like distribution.
Severe distortions caused by a strong band-limiting effect of the algorithm are visible in Fig. 32 b).

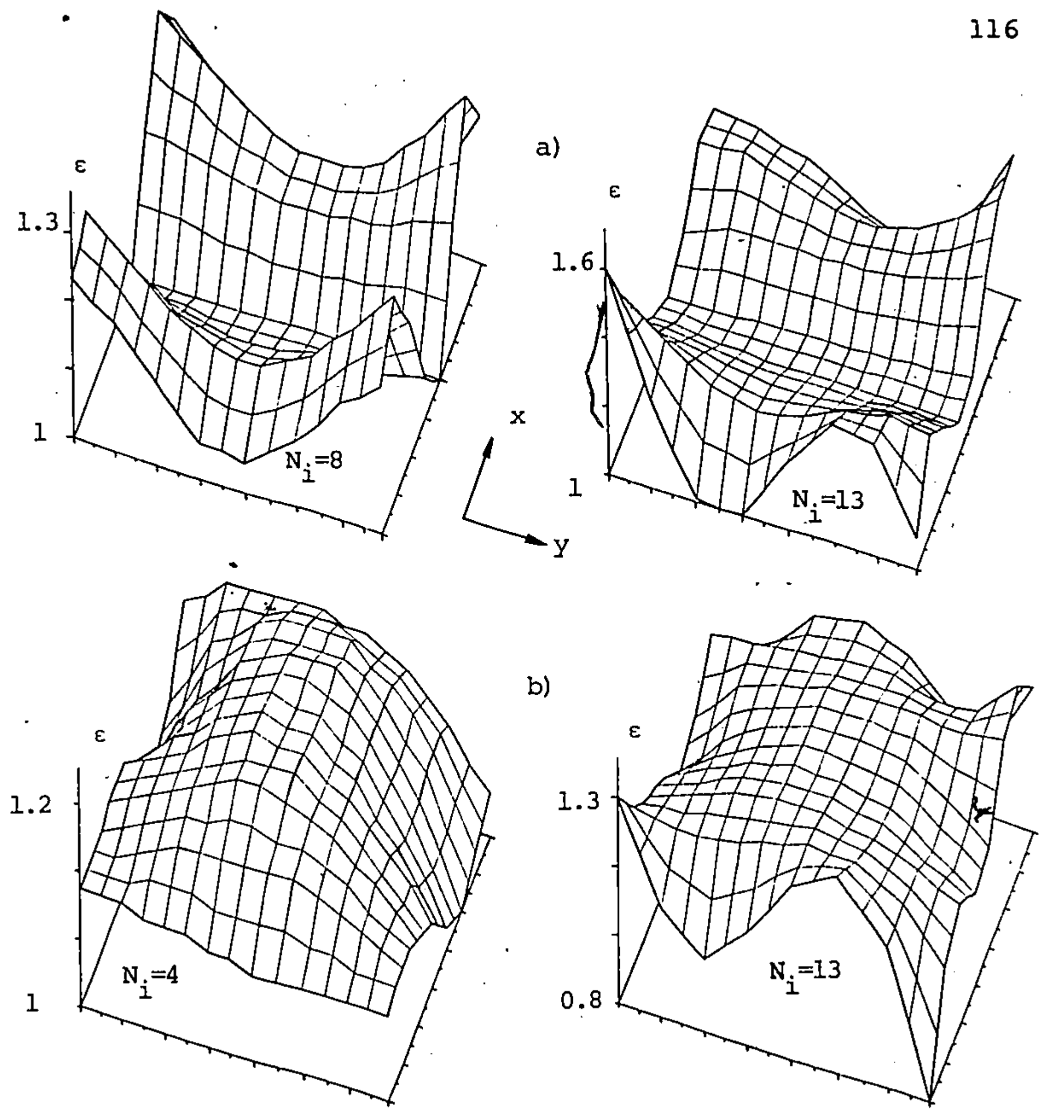

Figure 33: Reconstruction-algorithm capability of separating four rods.

The reconstruction of four rods of the dimension of the cells ($0.1 \times 0.1\ \lambda_0$) and dielectric constant 2.8 are represented in two cases :
a) separation=0.5 λ_0 S_n^s=23 dB (10,000 ppm).
b) separation=0.3 λ_0 S_n^s=24 dB (10,000 ppm).
The N_i values are selected at the beginning and at the end of the plateau of the $\|[d]\|$-vs.-N_i characteristic for each case.

in either direction when the noise level present in the measurement is equal or above 10,000 ppm.

A two-point spatial resolution better than $0.5\,\lambda_0$ cannot be obtained even when the signal-to-noise ratio in the measurements is increased by 20 dB as shown in Fig. 34 a),b) and c) which illustrate different selections of N_i. For instance, Fig. 34 c) shows the reconstruction for $N_i=28$, just before the turning point of the $\|[\bar{d}]\|$-vs.-N_i curve for which higher spatial oscillation amplitudes appear but the four rods even distorted cannot be detected. For relatively large matrix sizes, computational noise is sufficient to severely limit the spatial resolution capability of the method. This is illustrated in Fig. 34 d) in which the reconstructed rods are shown for noiseless input data. Thus, a spatial resolution of $0.3\,\lambda_0$ cannot be reached even for ideal measurement conditions in this case.

Two-dimensional dielectric-distribution reconstructions adequately illustrate the limitation of the method at its present stage of development. This type of distribution generally involves large matrix sizes and computational noise becomes preponderant. A two-point spatial resolution of $0.5\,\lambda_0$ with a realistic noise level of 10,000 ppm can be obtained with the detector configuration shown in Fig. 30 . Some improvement may be possible for other configurations of the detectors. For instance, the frequency of the incident signal may be chosen such that the dimensions of the scatterer cross-section are of the order of the wavelength,

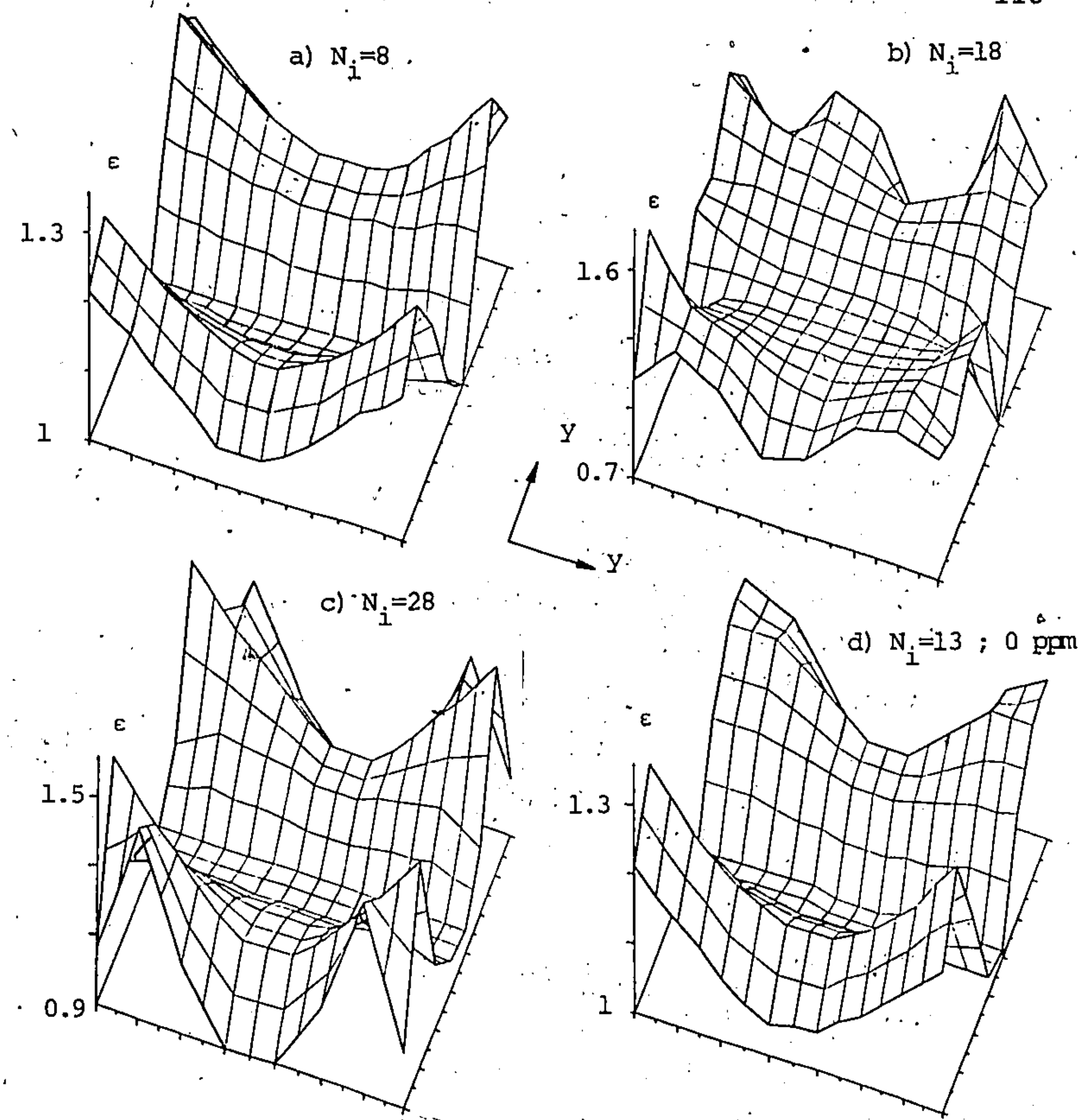

Figure 34: Reconstruction of four rods separated by $0.3\,\lambda_0$ for different noise levels.

The reconstruction of four rods represented in Fig. 31 c) is illustrated for a noise level equal to 1000 ppm corresponding to S_n^s=43 dB, for different values of N_i (Fig. 34 a) to c)).
Figure 34 d) shows the reconstruction for noiseless input data and illustrates the effect of computational noise only which limits the two-point spatial resolution of the algorithm to $0.5\,\lambda_0$.

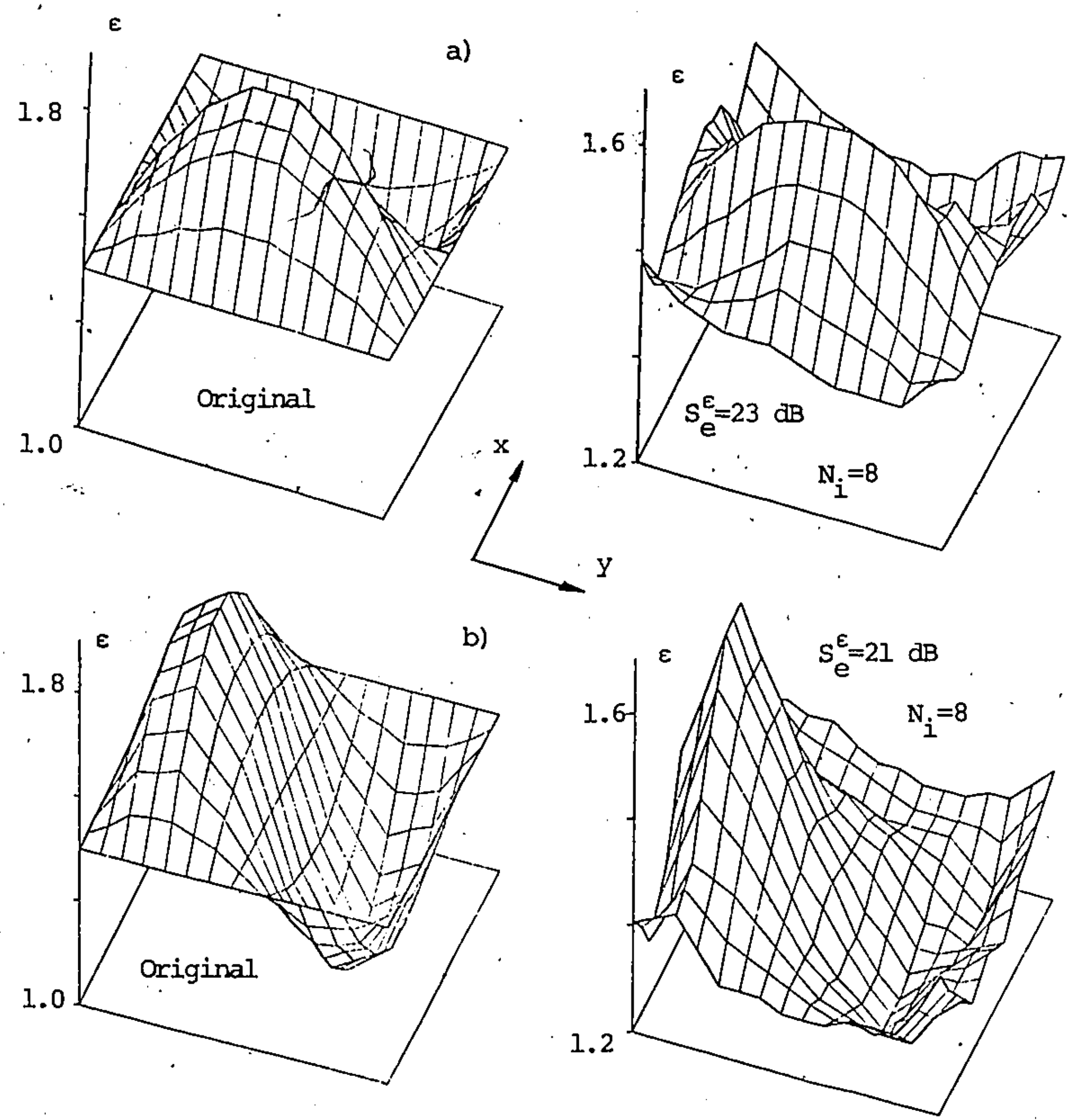

Figure 35: Reconstruction of a one-half-period-sine-square-like dielectric distribution.

The reconstructions of the real part of a sine-square-type dielectric distribution are shown when it is rotated by an angle of 90 degrees. The noise level is equal to 1000 ppm corresponding to S_n^s=41 dB in both cases.

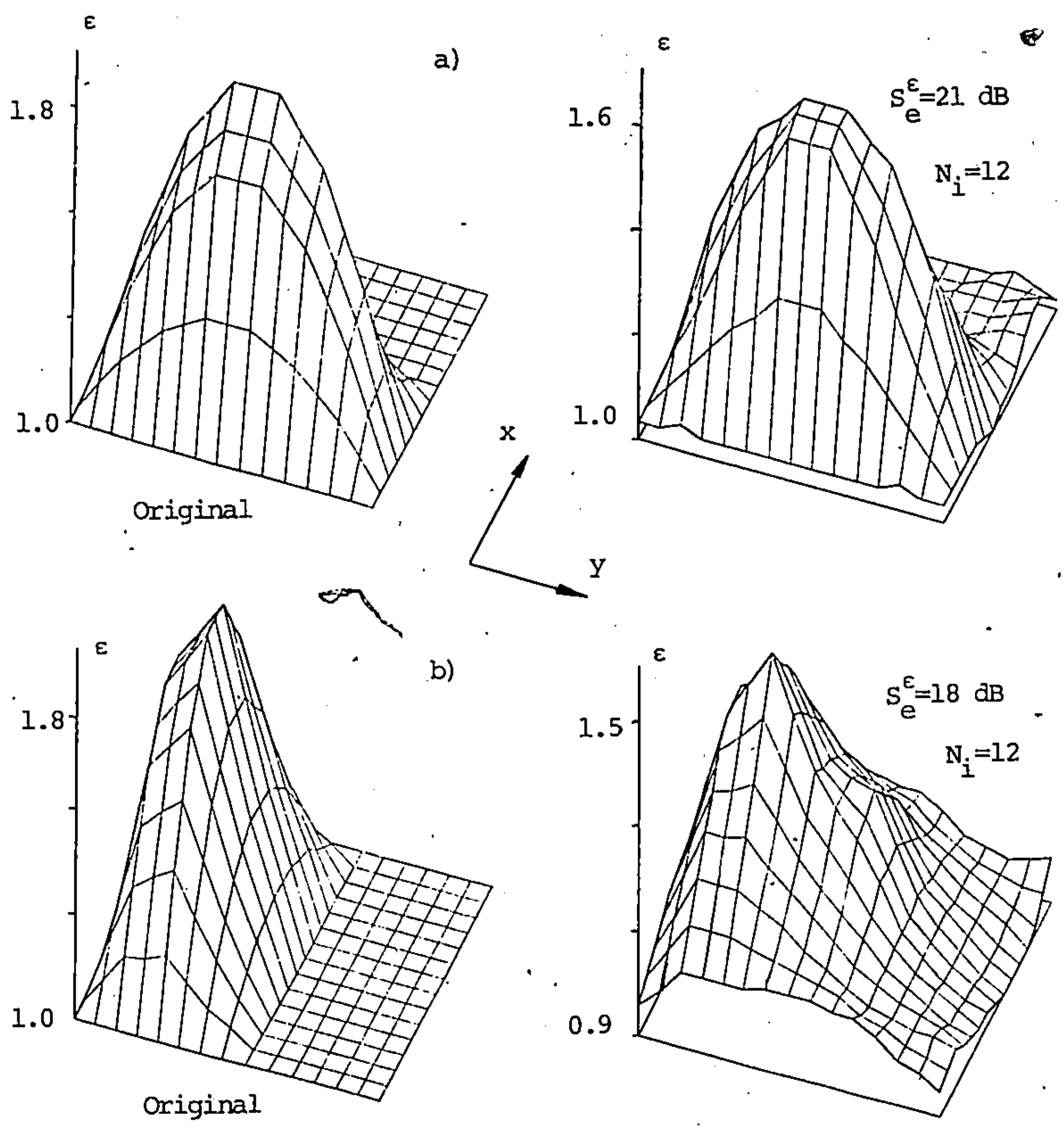

Figure 36: Reconstruction of a one-quarter-period-sine-square-like dielectric distribution.

The reconstructions of the real part of a one-quarter-period-sine-square-like distribution are shown when it is rotated by an angle of 90 degree.
The noise level is equal to 1000 ppm corresponding to S_n^s=42 dB in both cases.

in order to obtain strong diffraction effects which result in high S_n^s values. Unfortunately, in order to keep all detectors at a distance greater than 0.1 λ_0 from the scatterer, some detectors are located at distances as far as one wavelength. This certainly increases the degree of ill-conditioning of matrix [T]. A better detector configuration would consist of linear arrays placed parallel to each side of the grid. In this case, all detectors would be relatively close to the scatterer and would certainly reduce significantly the degree of ill-conditioning of the matrix [T].

The resolution of the algorithm turns out to be better in the direction of irradiation of the cylinder. This indicates that at least for two-dimensional distributions, the direction of the incident wave is also a parameter involved in the reconstruction fidelity. This is confirmed by Fig. 35 and 36, which show the reconstruction of dielectric distributions of the sine-square type function. The original dielectric distribution shown in Fig 35 b) is the same as the one shown in Fig 35 a) but rotated by an angle of 90 degrees. Fairly good signal-to-error ratios in the reconstruction are obtained in both cases, although the reconstruction shown in Fig. 35 b) indicates more distortions. The adopted method of graphical presentation amplifies the distortions since the plotting subroutine performs an automatic scaling[1]. It should be mentioned that there is a slight attenuation factor between the original and reconstructed dielectric profile introduced by the pseudoinverse operator. The same remarks apply to the example of reconstructions shown in Fig.36 . However, the difference in the reconstruction fidelity between the two cases is slightly more apparent in terms of S_e^{ε}.

4.14 COMMENTS AND FURTHER DEVELOPMENTS

The algorithm is found to yield good results when the number of cells is relatively small. This implies that it is efficient for thin cylinder and slowly-varying dielectric distributions, which require a relatively small number of cells. Regarding two-dimensional dielectric distributions, the method is limited, at its present stage of development, by the size of the matrices involved in the calculations. Stable solutions can be obtained, but details in the reconstructions are blurred by the band-limiting effect produced by the pseudoinverse transformation. This bandwidth limitation is controlled by the selection of the number N_i of column vectors of the matrix [T] which are taken as independent. That number is dictated by the degree of ill-conditioning of that matrix and the noise (computational and measurement noise) present in the process. However, the degree of ill-conditioning of the

[1]SAS/GRAPH system.

matrix [T] depends on the detector configuration. Further investigations should be carried out in order to determine an optimum detector configuration pertaining to a given grid (subdivided scatterer cross-section) and a given frequency. However, it has been found that in general, in order to obtain better reconstruction fidelities, the detectors must be placed as close as possible to the scatterer.

The difference in the spatial resolution along different directions indicates that more information could be gained by combining mesurements performed under different irradiation angles. This technique is similar to the one used in X-ray tomography (back-projection method). However, it should be borne in mind that the relationship between the scattered field vector and the unknown dielectric vector is a nonlinear one. In a recent paper [58], attempts to reconstruct thin cylinder dielectric distributions, using measurements at different irradiation angles, were presented. The application of the moment method yielded a system of nonlinear equations which was solved iteratively by using linear approximations. The size of the system was equal to the product of the number of cells times the number of irradiations. The results indicated that no more than two irradiations could be used (even for relatively small scatterers) because of computational problems. This clearly indicates that the combination of measurements at different angles of irradiation is difficult to implement due to the nonlinear nature of the problem.

By considering (2.28) which relates, in a linar manner, the polarization current density vector and the scattered field vector, a possibility resides in solving (2.28) iteratively using different irradiation angles. However, the unknown vector [d] depends on the irradiation angle and N more unknowns are introduced at each iteration.

The technique of using redundant data explored in Section 4.7 seems to be more attractive and generally yields better results. The introduction of redundant data in the algorithm is similar to introducing measurements at different irradiation angles. Although this technique increases the number of rows of the matrix [T] correspondingly to the number of redundant measurements, it has the advantage of not augmenting the number of unknowns.

Some image processing techniques such as inverse filtering [55] can be applied to the reconstructed dielectric distributions. The idea is to assume tha the reconstruction algorithm contains a linear filter blurring the original distributions. The point-spread-function [55] of the algorithm can be evaluated by using the Fourier transform. Then, the inverse filter (deblurring filter) can be deduced and applied to the reconstructed dielectric distributions. This procedure is expected to enhence high spatial frequency component amplitudes, without introducing any significant amount of noise.

Finally, the pseudoinverse transformation turns out to be a formidable tool for ill-conditioned problems but the technique used in this work to compute the smallest least-error solution, cannot prevent the round-off error propagation, even with the use of pivoting. Further investigations are necessary to implement an algorithm which minimizes round-off errors during the computations.

Chapter V

CONCLUSIONS

Long-wave imaging for dielectric cylinders has been proposed. It utilizes the method of moments and the knowledge of the scattered fields at discrete locations close to the scatterer when the latter is irradiated by a known wave. The problem is ill-conditioned and an advanced least-error technique, namely the pseudoinverse transformation, is required to obtain satisfactory results.

The method has some attractive features. Indeed, once an optimum geometry is found, the matrix [C] and $[T]^{\dagger}$ involved in the reconstruction algorithm are computed once and stored. Then, the computation of any dielectric vector requires only matrix multiplications and vector additions. Furthermore, the method does not make use of small perturbation techniques and can be potentially applied to high-contrast distributions. However, the introduction of the pseudoinverse transformation in the algorithm limits the spatial bandwidth capability of the method. This limitation becomes more significant when the level of noise present in the measurements increases. In addition, computational noise plays an important role in the bandwidth limitation of the algorithm and can even be preponderant when the size of the cylinder becomes larger which implies larger matrix sizes.

Computer simulations show that with a realistic level of noise (5 per cent uncertainties in scattered field values), a two-point spatial resolution of 0.5 λ_0 is feasible. However, at its present stage of development, there is a limitation of the method due to the size of the matrices which finally becomes the major factor involved in the bandwidth capability of the algorithm. Consequently, the method is applicable for small structures with slowly-varying dielectric distributions which require a relatively small number of cells. For these cases, satisfactory results can be obtained even with relatively high noise levels present in the measurements.

Appendix A

PSEUDOINVERSE COMPUTATION

A projection method [41] for finding the smallest least-error solution of a system of linear equations given by the matrix equation :

$$[T][d]=[e^{S}]$$

is described in this appendix. It utilizes a Gram-Schmidt orthogonalization which is performed on the column vectors of a matrix before applying the different steps yielding the smallest least-error solution as depicted in Fig. 8 .

It is well known that if two nearly equal quantities are subtracted, the relative error in the difference is far greater than the relative error in the quantities before subtraction. Thus, a sequence of computations can magnify and propagate errors to such an extent that the results are meaningless. The same reasoning applies when two nearly equal vectors are subtracted. In this case, the error is likely to be significant in both magnitude and direction. The Gram-Schmidt orthogonalization procedure applied to nearly dependent vectors invariably results in subtractions of nearly equal vectors.

Assume for instance, that two nearly dependent vectors are to be orthogonalized. The Gram-Schmidt procedure consists of projecting one vector, say $[t_2]$, on the other $[t_1]$. Then this projection is subtracted from $[t_2]$ yielding a vector perpendicular to $[t_1]$. This vector resulting from the orthogalization can be obtained from the following vector expression :

$$[z_2] = [t_2] - \langle t_2, t_1 \rangle / \|[t_1]\|^2 [t_1] \ , \tag{A.1}$$

where $\langle \ , \ \rangle$ denotes the inner scalar product given by :

$$\langle t_2, t_1 \rangle = ([t_1]^*)^T [t_2] \ .$$

The projection of $[t_2]$ on $[t_1]$ are automatically nearly equal if $[t_2]$ and $[t_1]$ are nearly dependent or collinear.

From the above discussion, the application of the Gram-Schmidt procedure on the column vectors of an ill-conditioned matrix (characterized by a presence of nearly dependent column vectors), results in propagation and magnification of errors yielding inconsistent results. Yet the Gram-Schmidt orthogonalization is the primary computational tool for solving practical least-square problems.

A way of handling such problems is to utilize scaling and pivoting in conjunction with double-precision arithmetic. At each stage of the orthogonalization, a vector of small norm is likely to be an inaccurate result of a previous subtraction. Error propagation can be avoided if these vectors are not used until the end of the procedure. The following procedure is recommended in [48] for orthogonalizing a set of vectors $\{t_1, t_2, \ldots, t_N\}$: Begin with the vector of largest norm (the pivot vector), say, $[z_p]=[t_p]$ and make all other vectors orthogonal using (A.1). From the now modified vectors (excluding $[z_p]$), choose the vector of the largest norm (the second pivot vector), say, $[z_q]=[\hat{t}_q]$ and make all other vectors (excluding $[z_p]$) orthogonal using (A.1) :

$$[\hat{t}_i]-\langle t_i, z_q\rangle/\|[z_q]\|^2[z_q] \quad i\neq p,q \ . \tag{A.2}$$

In order to keep a record of the operations on the columns of [T], the same operations given by (A.2) are performed on the columns of an identity matrix [I]. The procedure is continued until, at the (m+1)th stage, the search for $[z_{m+1}]$ finds no vectors whose norm is above a certain threshold. Another criterion to interrupt the procedure is to set the number $m=N_i$ of independent column vectors of the matrix [T]. Then, it is assumed that the remaining $(N-N_i)$ column vectors are [0]. At this stage, the original matrices [T] and [I] have been transformed to two new matrices [B] and [Q] respectively[1] :

$$\left[\begin{array}{c}[T]\\ \hline [I]\end{array}\right] \longrightarrow \left[\begin{array}{c|c} z_1 z_2 \cdots\cdots z_m & 0\ 0 \cdots 0 \\ \hline q_1 q_2 \cdots\cdots q_m & q_{m+1} \cdots q_N \end{array}\right] \tag{A.3}$$

Because [Q] records the operations performed on [T] one has :

$$[T][Q]=[B] . \tag{A.4}$$

Thus, multipying any vector of the set $\{q_{m+1},\ldots.q_N\}$ by [T] yields a zero vector. Consequently, the set of vectors $\{q_{m+1},\ldots.q_N\}$ is a basis for nullspace(T) which is then orthogonalized. In addition, the set of vectors $\{z_1,z_2,\ldots.,z_m\}$ forms an orthogonal basis for range(T). One defines the vector :

$$[w]=[\langle e^s,z_1\rangle/\|[z_1]\|^2,\ldots,\langle e^s,z_m\rangle/\|[z_m]\|^2,0,0..0]^T \tag{A.5}$$

The i-th component of [w] is the orthogonal projection value of the input vector $[e^s]$ on the vector $[z_i]$. Consequently, the projection of the input vector $[e^s]$ onto range(T) can be written as :

---

[1] The sequence of orthogonalization is not necessary from left to right but depends on [T]. For the sake of simplicity, z_i and consequently q_i appear in order in this example.

$$[e^S]_p=[B][w]=[T][Q][w] \quad . \tag{A.6}$$

The vector [w] is easy to compute, and a solution to the equation :

$$[T][d]=[e^S]_p$$

is clearly [d]=[Q][w] by virtue of (A.6).

Only the orthogonal projection of [d] onto range($\tilde{T}$) remains to be carried out. The set of vectors $\{q_{m+1},q_{m+2},\ldots,q_N\}$ constitutes a basis for the orthogonal complement of range($\tilde{T}$) by virtue of the decomposition theorem (3.12). Consequently, the smallest least-error solution is given by :

$$[d]_S=[\hat{d}]-\sum_{i=m+1}^{N}\langle\hat{d},q_i\rangle/\|[q_i]\|^2 q_i \quad . \tag{A.7}$$

The second term of the right-hand-side of (A.7) represents the orthogonal projection of the vector given by (A.6) onto nullspace(T).

The above procedure is easily automated. The matrix [T] needs to be orthogonalized only once for a given problem. This is an advantage since most of the computational time involved in the whole procedure takes place during the Gram-Schmidt orthogonalization. The remaining operations are simple. Note that the adjoint operator need not be determined in this method. If one wants the pseudoinverse explicitly, the input vector $[e^s]$ is replaced by a standard basis vector for C^{Nx1} and the steps from (A.3) to (A.7) are sequentially repeated for the N standard basis vectors yielding each time a column of the pseudoinverse of [T]. The orthogonalization of [T] has to be performed only once.

In conclusion, the procedure described above is, by its simplicity, very attractive. However, even with careful computing, significant errors will result for nearly dependent sets of vectors. To prevent meaningless results, the orthogonalization procedure has to be interrupted when the norm of the remaining column vectors of the matrix [T] to be orthogonalized is too small.

Appendix B

FORTRAN PROGRAMS

The listings of the subroutines PSEUDO and SCAT are given in this appendix. They are written in FORTRAN IV and constitute the major and important part of the subroutines that are utilized in the reconstruction algorithm and in the scattered field computations, respectively. The subroutines which compute the [C] and [T] matrix elements and the reconstructed dielectric vector are not presented.

B.1 SUBROUTINE PSEUDO

The subroutine PSEUDO computes the smallest least-error solution of the matrix equation :

[T][D]=[ES]

An option allows the computation of the pseudoinverse of the matrix T. The system of linear equations defined by the above expression can be over-determined (N0 greater than NC) or under-determined (N0 less than NC), where N0 is the number of observation points and NC is the number of cells.

```
C     CCCCCCCCCCCCCCCCCCCCCCCCCCCCCCCCCCCCCCCCCCCCCCCCCCCC
C
      SUBROUTINE PSEUDO (N0,NC,IORT,T,Q,QN,D,W,ES,RMAG,INDEX
     #                    ,NS,DS,RM,IST,NI)
C
C     CCCCCCCCCCCCCCCCCCCCCCCCCCCCCCCCCCCCCCCCCCCCCCCCCCCC
C
C     INPUTS/OUTPUTS :
C
C     IORT : 1 THE MATRIX T IS ORTHOGONALIZED (FIRST CALL)
C          : 0 FOR SUCCESSIVE CALLS WHEN ONLY THE INPUT ES
C              IS CHANGED (NOT TO BE USED WHEN THE PSEU-
C              DOINVERSE OF T IS WANTED).
C     T(N0,NC) : COMPLEX*16 MATRIX ([T][D]=[ES]).
C                IN ANY CASE T WILL BE DESTROYED.
C     NS=1     : THE COMPLEX*16 VECTOR DS(NC,1) CONTAINS THE
C                SMALLEST LEAST-ERROR SOLUTION OF
C                [T][D]=[ES].
C     NS=N0    : DS(NC,NS) WILL BE THE PSEUDOINVERSE OF T.
C     ES(N0)   : COMPLEX*16 VECTOR CONTAINING THE INPUT.
C                ES IS USED ONLY IF NS=1.
C     RM       : REAL*8 . ALL COLUMN VECTORS OF T AFTER
C                ORTHOGONALIZATION WHOSE MAGNITUDE IS
C                RM TIMES LESS THAN THE BIGGEST T COLUMN-
C                VECTOR MAGNITUDE ARE SET TO [0].
C     IST      : IST COLUMNS OF T HAVE BEEN ORTHOGONALIZED.
C     NI       : NO. OF COLUMNS OF T TO BE ORTHOGONALIZED.
C                (NC-NI) COLUMNS WILL BE CONSIDERED AS [0].
C                THEIR MAGNITUDE ARE RM TIMES LESS THAN THIS
```

```
C                 OF FIRST ORTHOGONALIZED T COLUMN VECTORS.
C
C      OTHER QUANTITIES :
C
C      COMPLEX*16 MATRIX Q(NC,NC)
C      COMPLEX*16 VECTOR D(NC)
C      COMPLEX*16 VECTOR W(NC)
C      COMPLEX*16 MATRIX QN(NC,NC)
C      REAL*8 VECTOR RMAG(NC)
C      INTEGER INDEX(NC)
C
C      AUTHOR : MICHEL NEY MARCH 1982 (REVISED FEB. 1983).
C
C      CCCCCCCCCCCCCCCCCCCCCCCCCCCCCCCCCCCCCCCCCCCCCCCCCCCCCCCCC
C
      COMPLEX*16 T(N0,NC),Q(NC,NC),QN(NC,NC),
     #D(NC),W(NC),ES(N0),DS(NC,NS),CSUM
      REAL*8 RMAG(NC),RM,SUM,BIG,BIGST
      INTEGER INDEX(NC)
      IF (IORT.EQ.0) GO TO 199
      IF (IST.NE.1) GO TO 198
      DO 99 I=1,NC
      DO 99 J=1,NC
 99   Q(I,J)=(0.D0,0.D0)
      DO 1 I=1,NC
      Q(I,I)=(1.D0,0.D0)
      RMAG(I)=0.D0
 1    INDEX(I)=0
C
C     FIND THE BIGGEST MAGNITUDE AMONG T COLUMN VECTORS
C     NOT IN RANGE(T) (PIVOT) :
C
 198  DO 100 K=IST,NI
      DO 2 I=1,NC
      IF (INDEX(I).EQ.1) GO TO 2
      IF0=I
      GO TO 3
 2    CONTINUE
 3    SUM=0.D0
      DO 4 I=1,N0
 4    SUM=SUM+T(I,IF0)*DCONJG(T(I,IF0))
      BIG=SUM
      ITEST=IF0
      IF (ITEST.EQ.NC) GO TO 19
      I0=IF0+1
      DO 10 J=I0,NC
      IF (INDEX(J).EQ.1) GO TO 10
      SUM=0.D0
      DO 11 I=1,N0
 11   SUM=SUM+T(I,J)*DCONJG(T(I,J))
      IF (SUM.LE.BIG) GO TO 10
      BIG=SUM
      ITEST=J
 10   CONTINUE
```

```
 19   IF (K.EQ.1) BIGST=BIG
      INDEX(ITEST)=1
      RMAG(ITEST)=BIG
      RM=DSQRT(BIG/BIGST)
C
C     T COLUMN VECTORS NOT IN RANGE(T) ARE OTHOGONALIZED :
C
      CALL ORTHO (N0,NC,T,Q,INDEX,BIG,ITEST)
 100  CONTINUE
C
C     THE BASIS OF NULLSPACE(T) IS ORTHOGONALIZED :
C
C
C     FIND THE BIGGEST MAGNITUDE OF THE COLUMN VECTORS OF Q
C     SPANNING NULLSPACE(T) (PIVOT) :
C
      NQ=NC-NI
      IF (NQ.EQ.0) GO TO 199
      DO 40 I=1,NC
      IF (INDEX(I).NE.0) GO TO 40
      DO 45 J=1,NC
 45   QN(J,I)=Q(J,I)
 40   CONTINUE
      DO 50 K=1,NQ
      DO 52 I=1,NC
      IF (INDEX(I).NE.0) GO TO 52
      IF0=I
      GO TO 53
 52   CONTINUE
 53   SUM=0.D0
      DO 54 I=1,NC
 54   SUM=SUM+QN(I,IF0)*DCONJG(QN(I,IF0))
      BIG=SUM
      ITEST=IF0
      IF (ITEST.EQ.NC) GO TO 69
      I0=IF0+1
      DO 60 J=I0,NC
      IF (INDEX(J).NE.0) GO TO 60
      SUM=0.D0
      DO 61 I=1,NC
 61   SUM=SUM+QN(I,J)*DCONJG(QN(I,J))
      IF (SUM.LE.BIG) GO TO 60
      BIG=SUM
      ITEST=J
 60   CONTINUE
 69   INDEX(ITEST)=2
      RMAG(ITEST)=BIG
C
C     ORTHOGONALIZATION :
C
      DO 72 J=1,NC
      IF (INDEX(J).NE.0) GO TO 72
      CSUM=(0.D0,0.D0)
      DO 74 I=1,NC
```

```
 74   CSUM=CSUM+QN(I,J)*DCONJG(QN(I,ITEST))
      CSUM=CSUM/BIG
      DO 76 KK=1,NC
 76   QN(KK,J)=QN(KK,J)-QN(KK,ITEST)*CSUM
 72   CONTINUE
 50   CONTINUE
C
C     AT THIS STAGE NI COLUMN VECTORS OF THE MATRIX T ARE
C     ORTHOGONALIZED AND SPAN RANGE(T).
C     NC-NI COLUMN VECTORS OF THE MATRIX Q WHICH SPAN
C     NULLSPACE(T) ARE ORTHOGONALIZED.
C
C     CCCCCCCCCCCCCCCCCCCCCCCCCCCCCCCCCCCCCCCCCCCCCCCCCCCC
C
C
C     PROJECTION OF INPUT VECTOR ES ON RANGE(T) :
C
C
 199  DO 200 K=1,NS
      IF (NS.NE.1) GO TO 250
      DO 202 J=1,NC
      CSUM=(0.D0,0.D0)
      IF (INDEX(J).NE.0) GO TO 204
      W(J)=(0.D0,0.D0)
      GO TO 202
 204  DO 206 I=1,N0
 206  CSUM=CSUM+ES(I)*DCONJG(T(I,J))
      W(J)=CSUM/RMAG(J)
 202  CONTINUE
      GO TO 300
C
C     FOR FULL PSEUDOINVERSION OF T THE INPUT VECTOR ES IS
C     THE COLUMN VECTOR OF THE INDENTITY MATRIX WHICH
C     CORRESPOND TO THE PSEUDOINVERSE COLUMN BEING COMPUTED.
C
 250  DO 252 J=1,NC
      IF (INDEX(J).NE.0) GO TO 254
      W(J)=(0.D0,0.D0)
      GO TO 252
 254  W(J)=DCONJG(T(K,J))/RMAG(J)
 252  CONTINUE
C
C     SOLUTION OF [T][D]=[ESP] WHERE ESP IS THE ORTHOGONAL
C     PROJECTION OF ES ONTO RANGE(A) :
C
 300  DO 302 I=1,NC
      CSUM=(0.D0,0.D0)
      DO 304 J=1,NC
      DS(J,K)=(0.D0,0.D0)
 304  CSUM=CSUM+Q(I,J)*W(J)
 302  D(I)=CSUM
C
C     ORTHOGONAL PROJECTION OF D ONTO RANGE(ADJOINT OF T)
C     GIVES THE SMALLEST LEAST-ERROR SOLUTION OF THE SYSTEM
```

```
C     [T][D]=[ES] OR A COLUMN OF THE PSEUDOINVERSE OF A :
C
      DO 400 J=1,NC
      IF (INDEX(J).NE.2) GO TO 400
      CSUM=(0.D0,0.D0)
      DO 402 I=1,NC
 402  CSUM=CSUM+D(I)*DCONJG(QN(I,J))
      DO 404 I=1,NC
 404  DS(I,K)=DS(I,K)+QN(I,J)*CSUM/RMAG(J)
 400  CONTINUE
      DO 406 I=1,NC
 406  DS(I,K)=D(I)-DS(I,K)
 200  CONTINUE
      IF (IORT.EQ.0) GO TO 599
      DO 500 I=1,NC
      IF (INDEX(I).NE.2) GO TO 500
      INDEX(I)=0
      RMAG(I)=0.D0
 500  CONTINUE
 599  RETURN
      END
C     CCCCCCCCCCCCCCCCCCCCCCCCCCCCCCCCCCCCCCCCCCCCCCCCCCCCCCCCCC
C
      SUBROUTINE ORTHO (N0,NC,T,Q,INDEX,BIG,ITEST)
C
C     CCCCCCCCCCCCCCCCCCCCCCCCCCCCCCCCCCCCCCCCCCCCCCCCCCCCCCCCCC
C
C     THIS ROUTINE SETS ALL REMAINING COLUMN VECTORS OF T
C     WHOSE MAGNITUDE IS SMALLER THAN THIS OF THE COLUMN
C     WITH INDEX=ITEST ORTHOGONAL TO IT.
C
      COMPLEX*16 T(N0,NC),Q(NC,NC),CSUM
      INTEGER INDEX(NC)
      REAL*8 BIG
      DO 2 J=1,NC
      IF (INDEX(J).NE.0) GO TO 2
      CSUM=(0.D0,0.D0)
      DO 4 I=1,N0
 4    CSUM=CSUM+T(I,J)*DCONJG(T(I,ITEST))
      CSUM=CSUM/BIG
      DO 6 K=1,N0
 6    T(K,J)=T(K,J)-T(K,ITEST)*CSUM
      DO 8 K=1,NC
 8    Q(K,J)=Q(K,J)-Q(K,ITEST)*CSUM
 2    CONTINUE
      RETURN
      END
```

B.2 SUBROUTINE SCAT

The subroutine SCAT computes the scattered field produced by an infinite dielectric cylinder with arbitrary cross-section. Various options are available and are described in the program listing. Part of this program was graciously provided by Prof. J. Richmond from the Ohio State University.

```
C     CCCCCCCCCCCCCCCCCCCCCCCCCCCCCCCCCCCCCCCCCCCCCCCCCCCCCC
C
      SUBROUTINE SCAT(E0,FI,T,F,AE,N0,X,Y,NC,XC,YC,CH,NE,EP,
     #                IF,IC,IP,EC,NA,CWA,CWK,ESCA,IE)
C
C     CCCCCCCCCCCCCCCCCCCCCCCCCCCCCCCCCCCCCCCCCCCCCCCCCCCCCC
C
C     INPUT :
C
C     E0 = INCIDENT FIELD AMPLITUDE (TEM WAVE) [V/M]
C     FI = PHASE OF THE INCIDENT FIELD AT THE ORIGINE [DEG].
C     T = ANGLE OF INCIDENT WAVE [DEG].
C     F = FREQUENCY OF THE SIGNAL [HZ].
C
C     THE INCIDENT FIELD IS A PLANE WAVE TRAVELING ALONG
C     THE DIRECTION GIVEN BY THE VECTOR [COS(T),SIN(T)].
C
C     AE = CELL EQUIVALENT RADIUS [M] (AE=SQRT(AREA/PI))
C     N0 = NUMBER OF OBSERVATION POINTS.
C     X,Y = VECTORS (N0) OF THE RECTANGULAR COORDINATES
C           OF THE OBSERVATION POINTS [M].
C     NC =  NUMBER OF CELLS.
C     XC,YC = VECTORS (NC) OF THE RECTANGULAR COORDINATES
C             OF THE CELLS [M].
C     NE = 1 : HOMOGENEOUS DIELECTRIC.
C        =NC : GENERAL CASE.
C     EP = COMPLEX VECTOR (NE) OF DIELECTRIC CONSTANT OF
C          THE CELLS.
C     IF = 1 : FAR FIELD CALCULATION.
C        = 0 : NEAR FIELD CALCULATION.
C     IC = 0 : POLAR COORDINATES OF OBS. POINTS PRINTED OUT.
C        = 1 : RECTANGULAR COORDINATES.
C     IP = 1 : ALL QUANTITIES ARE PRINTED OUT.
C          0 : NO PRINT OUT.
C     IE = 1 : THE TOTAL FIELD INSIDE THE CELLS IS COMPUTED.
C          0 : FOR SUBSEQUENT CALLS WHEN THE TOTAL FIELD IN-
C              SIDE THE CELLS DOES NOT CHANGE .
```

```
C
C     OUTPUT :
C
C     EC = COMPLEX MATRIX (NC,1) OF TOTAL FIELD INSIDE
C          THE CELLS.
C     HC = COMPLEX MATRIX (NC,NC) FOR INTERNAL USE.
C     ESCA(N0) = COMPLEX*16 SCATTERED FIELD VECTOR.
C
C     REMARK :
C
C     ALL REAL AND COMPLEX VARIABLES IN DOUBLE PRECISION !!!
C
C
C     REQUIRED ROUTINES :
C
C     MMBSJ0,MMBSJ1,MMBSYN,LEQ2C (IMSL)
C
C     USING :
C
C     CWA(NA),CWK(NC)  WITH NA=NC*(NC+2)
C
C     AUTHOR : J. RICHMOND (MODIFIED BY M. NEY) JUNE 1981.
C
C     CCCCCCCCCCCCCCCCCCCCCCCCCCCCCCCCCCCCCCCCCCCCCCCCCCCCCCCC
C
      REAL*8 MMBSJ0,MMBSJ1,BY(2),AC,R,ORDER,PI,F,FI,E0,DR,B0
      REAL*8 X(N0),Y(N0),XC(NC),YC(NC),T,XX,YY,AE,ANGLE,R0
     #,AG,BJ
      COMPLEX*16 CH(NC,NC),EC(NC,1),EP(NE),C,CSUM,CA,CE
      COMPLEX*16 CEINC,CWA(NA),CWK(NC),ESCA(N0)
C
C     INCIDENT FIELD :
C
      CEINC(E0,FI,T,B0,XX,YY)=E0*CDEXP((0.D0,-1.D0)*
     #(B0*(XX*DCOS(T*DR)+YY*DSIN(T*DR))-FI*DR))
      ORDER=0.D0
      PI=2.D0*DARSIN(1.D0)
      DR=PI/180.D0
      C=(0.D0,1.D0)
      B0=2.D0*PI*F/3.D8
      AC=B0*AE
      DO 5 I=1,NE
 5    EP(I)=EP(I)-(1.D0,0.D0)
      IF (IP.EQ.0) GO TO 8
      PRINT 1,T,F,AE
      IF (IC.EQ.1) PRINT 2
      IF (IC.EQ.0) PRINT 3
 8    N=2
      CALL MMBSYN (AC,ORDER,N,BY,IER)
      BJ=MMBSJ1(AC,IER)
      CE=PI*AC*(0.D0,0.5D0)*BJ
      IF (NE.EQ.1) CE=CE*EP(1)
      IF (IE.EQ.0) GO TO 40
      CA=(0.D0,0.5D0)*(PI*AC*(BJ-C*BY(2))-(0.D0,2.D0))
```

```
      IF (NE.EQ.1) CA=1.D0+CA*EP(1)
      DO 10 I=1,NC
      IF (NE.EQ.1) GO TO 15
      CH(I,I)=1.D0+EP(I)*CA
      GO TO 10
 15   CH(I,I)=CA
 10   CONTINUE
      N=1
      DO 30 I=1,NC
      EC(I,1)=CEINC(E0,FI,T,B0,XC(I),YC(I))
      DO 30 J=I,NC
      IF (I.EQ.J) GO TO 30
      R=DSQRT((XC(I)-XC(J))**2+(YC(I)-YC(J))**2)*B0
      CALL MMBSYN (R,ORDER,N,BY,IER)
      BJ=MMBSJ0(R,IER)
      CA=CE*(BJ-C*BY(1))
      IF (NE.EQ.1) GO TO 35
      CH(I,J)=CA*EP(J)
      CH(J,I)=CA*EP(I)
      GO TO 30
 35   CH(I,J)=CA
      CH(J,I)=CA
 30   CONTINUE
C
C     L-U DECOMPOSITION OF CH
C
      IJOB=1
      CALL LEQ2C (CH,NC,NC,EC,M,NC,IJOB,CWA,CWK,IER)
C
C     TOTAL FIELD IN EACH CELL (CONTAINED IN EC)
C
      IJOB=2
      M=1
      CALL LEQ2C (CH,NC,NC,EC,M,NC,IJOB,CWA,CWK,IER)
C
C     FIELD CALCULATIONS
C
 40   IF (IF.EQ.1) CE=CE*CDSQRT((0.D0,2.D0)/PI)
      DO 50 K=1,N0
      CSUM=(0.D0,0.D0)
      IF (IF.EQ.0.AND.IC.EQ.1) GO TO 55
      R0=DSQRT(X(K)*X(K)+Y(K)*Y(K))
      AG=ANGLE(X(K),Y(K),DR)
      IF (IF.NE.1) GO TO 55
      R=R0*B0
      CA=CE*CDEXP(-C*R)/DSQRT(R)
 55   DO 60 I=1,NC
      IF (IF.EQ.1) GO TO 100
      R=DSQRT((XC(I)-X(K))**2+(YC(I)-Y(K))**2)*B0
      CALL MMBSYN (R,ORDER,N,BY,IER)
      BJ=MMBSJ0(R,IER)
      CA=CE*(BJ-C*BY(1))
      IF (NE.EQ.1) GO TO 70
      CSUM=CSUM-CA*EP(I)*EC(I,1)
```

```
      GO TO 60
 70   CSUM=CSUM-CA*EC(I,1)
      GO TO 60
 100  IF (NE.EQ.1) GO TO 110
      CSUM=CSUM-CA*EC(I,1)*EP(I)*
     #CEINC(1.D0,0.D0,AG,B0,XC(I),YC(I))
      GO TO 60
 110  CSUM=CSUM-CA*EC(I,1)*
     #CEINC(1.D0,0.D0,AG,B0,XC(I),YC(I))
  60  CONTINUE
      ESCA(K)=CSUM
      IF (IP.EQ.0) GO TO 50
      CA=CSUM+CEINC(E0,FI,T,B0,X(K),Y(K))
      IF (IC.EQ.1) PRINT 200,X(K),Y(K),CA,CSUM
      IF (IC.EQ.0) PRINT 201,R0,AG,CA,CSUM
 50   CONTINUE
      DO 290 I=1,NE
 290  EP(I)=EP(I)+(1.D0,0.D0)
      IF (IP.EQ.0) RETURN
      IF (IF.EQ.1) PRINT 330
      PRINT 300
      DO 310 I=1,NC
      IF (NE.EQ.1) PRINT 200,XC(I),YC(I),EP(1),EC(I,1)
      IF (NE.NE.1) PRINT 200,XC(I),YC(I),EP(I),EC(I,1)
 310  CONTINUE
      RETURN
 1    FORMAT(/' PLANE WAVE INCIDENT AT ',D11.4,' [DEG], F= '
     #,D1.4,' [HZ], EQ. CELL RADIUS= ',D11.4,' [M]')
 2    FORMAT(/' RECTANGULAR COORDINATES',7X,
     #'TOTAL FIELD [V/M]',9X,'SCATTERED FIELD [V/M]'//
     #'     X [M]',6X,'Y [M]'/)
 3    FORMAT(/'       POLAR  COORDINATES',8X,
     #'TOTAL FIELD [V/M]',10X,'SCATTERED FIELD [V/M]'//
     #'     R [M]',4X,'PHI [DEG]'/)
 200  FORMAT(' ',D10.3,1X,D10.3,3X,'(',D11.4,',',D11.4,')(',
     #D14.7,',',D14.7,')')
 201  FORMAT(' ',D10.3,2X,F7.2,4X,'(',D11.4,',',D11.4,')(',
     #D14.7,',',D14.7,')')
 300  FORMAT(/' CELL RECT. COORDINATES ',7X,
     #'REL. DIEL. CONST.',9X,'TOT. INT. FIELD [V/M]'//
     #'   XC [M]',6X,'YC[M]'/)
 330  FORMAT(/' FAR FIELD VALUES  !!'/)
      END
C     CCCCCCCCCCCCCCCCCCCCCCCCCCCC
C
      FUNCTION ANGLE (X,Y,DR)
C
C     CCCCCCCCCCCCCCCCCCCCCCCCCCCC
C
C     ANGLE COMPUTES THE PHASE OF A
C     VECTOR (X,Y) IN DEGRE (0-360)
C     DR=PI/180.D0.
C
C     CCCCCCCCCCCCCCCCCCCCCCCCCCCC
```

```
C
      REAL*8 ANGLE,X,Y,DR
      IF (X.NE.0.D0) GO TO 10
      IF (Y.NE.0.D0) GO TO 5
      ANGLE=0.D0
      RETURN
 5    IF (Y.LT.0.D0) GO TO 6
      ANGLE=90.D0
      RETURN
 6    ANGLE=270.D0
      RETURN
 10   ANGLE=DATAN(Y/X)/DR
      IF (X.LT.0.D0) GO TO 20
      IF (Y.GE.0.D0) RETURN
      ANGLE=ANGLE+360.D0
      RETURN
 20   ANGLE=ANGLE+180.D0
      RETURN
      END
```

REFERENCES

[1] G.N. Hounsfield, "Computerized Transverse Axial Scanning (Tomography) Part 1 : Description of System", British J. of Radiology, Vol. 46, 1973, pp. 1016-1022.

[2] A.C. Kak, "Computerized Tomography with X-Ray, Emission and Ultrasound Sources", Proc. of the IEEE, Vol. 67, No. 9, Sept. 1979, pp. 1245-1272.

[3] K.A. Dines and A.C. Kak, "Ultrasonic Attenuation Tomography of Soft Tissue", Ultrasonic Imaging, Vol. 1, No. 1, 1979, pp. 16-33.

[4] J.F. Greenleaf, S.A. Johnson, W.F. Samayoa and F.A. Duck, "Algebraic Reconstruction of Spacial Distributions of Acoustic Velocities in Tissue from their Time-of-Flight Profiles", Acoustic Holography, Vol. 6,1975, Plenum Press,N. Y., pp. 71-90.

[5] P.L. Carson, T.V. Oughton, W.R. Hendee and A.S. Ahuja, "Imaging Soft Tissue through Bone with Ultrasound Transmission Tomography by Reconstruction", Medical Physics, Vol. 4, No. 4, Jul./Aug. 1977, pp. 320-309.

[6] K.A. Dines and R.J. Lytle, "Computerized Geophysical Tomography", Proc. of the IEEE, Vol. 67, No. 7, Jul. 1979, pp. 1065-1073.

[7] R. Gordon, "A Tutorial on ART", IEEE Trans. on Nuclear Science, Vol. NS-21, June 1974, pp. 78-92.

[8] P. Gilbert, "Iterative Methods for the Three Dimensional Reconstruction of an Object from Projections", J. of Theor. Biol., Vol. 36, 1972, pp. 105-117.

[9] P.M. Forgues, M. Goldberg, A.M. Smith and S.S. Stuchly, "Computer-Controlled Scattering Measurements in a Parallel-Plate Configuration", IEEE Trans. on Instrumentation and Measurement, Vol. IM-30, No. 3, Sept. 1981, pp. 194-198.

[10] R.J. Lytle, O.L. Lager, E.F. Laine and D.T. Davis, "Using Cross-Borehole Electromagnetic Probing to Locate a a Tunnel", Lawrence Livermore Lab report # UCRL-52166, Oct. 1976.

[11] O.C. Yue, E.L. Rope and G. Tricoles, "Two Reconstruction Methods for Microwave Imaging of Buried Dielectric Anomalies", IEEE Trans. on Computers, Vol. C-24, No. 4, Apr. 1975, pp. 381-390.

[12] R.P. Anderson and J.G. Webster, "Impedance Camera for Spatially Specific Measurements of the Thorax", IEEE Trans. on Biomedical Eng., Vol. BME-25, No. 3, May 1878, pp. 250-254.

[13] R.J. Lytle and K.A. Dines, "An Impedance Camera : A System for Determining the Spatial Variation of Electrical Conductivity", Lawrence Livermore Lab report # UCRL-52413, Jan. 1978.

[14] L.R. Price, "Electrical Impedance Computed Tomography (ICT) : A New Imaging Technique", IEEE Trans on Nuclear Science, Vol. NS-26, No. 2, April 1979, pp. 2736-2739.

[15] R.H.T. Bates, G.C. McKinnon and A.D. Seagar," A limitation on Systems for Imaging Electrical Conductivity Distributions", IEEE Trans. on Biomedical Eng., Vol. BME 27, No. 7, July 1980, pp. 418-420.

[16] E.C. Gregg, " Microwave Radiation in Cancer Diagnosis-Transmission", Scientific Exhib. at AAPM Annual Meeting, Atlanta, Georia, Aug. 1979.

[17] I.E. Larsen and J.H. Jacobi, "Microwave Scattering Parameter Imagery of an Isolated Canine Kidney", Medical Physics, Vol. 6, No. 5, 1979, pp. 394-403.

[18] R. Maini, M.F. Iskander and C.H. Durney, "On the Electromagnetic Imaging Using Linear Reconstruction Techniques", Proc. of the IEEE, Vol. 68, No. 12, 1980, pp. 1550-1552.

[19] H. Ermet, G. Fulle and D. Hiller, "Microwave Computerized Tomography", 11th European Microwave Conf., Amsterdam, 1981.

[20] M.F. Iskander, R. Maini and C.H. Durney, "Microwave Imaging : Numerical Simulations and Results", Int. Symp., Los Angeles, June 1981.

[21] R.K. Mueller, M. Kaveh and G. Wade, "Reconstructive Tomography and Applications to Ultrasonics", Proc. of the IEEE, Vol. 67, No. 4, April 1979, pp. 567-587.

[22] M.F. Adams and A.P. Anderson, "Three-Dimensional Image-Reconstruction Technique and its Application to Coherent Microwave Diagnostics", IEE Proc., Vol. 127, Part H, No. 3, June 1980, pp. 138-142.

[23] N.N. Bojarski, "Inverse Scattering Inverse Source Theory", Jour. Math. Phys., Vol. 22, No. 8, Aug. 1981, pp. 1647-1650.

[24] W.R. Stone, "Geophysical Inversion and Remote Probing are Inverse Scattering Problems", 1981 IEEE Digest, Int. Geosci., Remote Sensing Symp., Vol. II, pp. 1334-1339.

[25] A.J. Devaney," Nonuniqueness in the Inverse Scattering Problem", Jour. Math. Phys., Vol. 19, No. 7, July 1978, pp. 1226-1531.

[26] N. Bleistein and J.K. Cohen, " Nonuniqueness in the Inverse Source Problem in Acoustics and Electromagnetics", Jour. of Math. Phys., Vol. 18, No. 2, Feb. 1977.

[27] A.J. Devaney and E. Wolf, "Radiating and Nonradiating Classical Current Distributions and the Fields they Generate", Physical Review D, Vol. 8, No. 4, Aug. 1973, pp. 1044-1047.

[28] R.P. Porter and E. Devaney, "Holography and the Inverse Source Problem", Jour. Opt. Soc. Am., Vol. 72, No. 3, Mar. 1982, pp. 327-330.

[29] A.J. Devaney and G.C. Sherman, "Nonuniqueness in Inverse Source and Scattering Problems", IEEE Trans. on Ant. and Propagation, Vol. AP-30, No. 5, Sept. 1982, pp.1034-1042.

[30] E. Wolf, "Three-Dimensional Structure Determination of Semi-Transparent Objects from Holographic Data", Optic. Communication, Vol. 1, No. 4, 1969, pp. 153-156.

[31] K. Iizuka, "Microwave Holography by Means of Optical Interference Holography", Applied Phys. Letters, Vol. 17, No. 3, pp. 99-101.

[32] L.G. Gregoris and K. Iizuka, "Visualization of Internal Structure by Microwave Holography", Proc. of the IEEE, Vol. 58, No. 5, May 1970, pp. 791-792.

[33] A.J. Tijhuis, "Iterative Determination of Permittivity and Conductivity Profiles of a Dielectric Slab in the Time Domain", IEEE Trans. on Ant. and Propagation, Vol. AP-29, No. 2, March 1981, pp. 239-245.

[34] F.M. Adams and A.P. Anderson, "Synthetic Aperture Tomography (SAT) Imaging for Microwave Diagnostics", IEE Proc., Vol. 129, Pt. H, No. 2, April 1982, pp. 83-88.

[35] J.C. Bolomey, A. Izadnegahdar, L. Jofre, C. Pichot, G. Peronnet and M. Solaimani, " Microwave Diffraction Tomography for Biomedical Applications", IEEE Trans. on Microwave Theory and Tech., Vol. 30, No. 11, Nov. 1982, pp. 1998-2000.

[36] R.F. Harrington," Time-Harmonic Electromagnetic Fields", McGraw-Hill, New-York, 1961, pp. 223-232.

[37] R.F. Harrington, "Field Computation by Moment Method", Roger F. Harrington, Cazenovia, New-York, 1968.

[38] J.H. Richmond, "Scattering by a Dielectric Cylinder of Arbitrary Cross-Section Shape", IEEE Trans. on Ant. and Propagation, Vol. 13, May 1965, pp. 334-341.

[39] M.J. Hagmann, O.P. Gandhi and C.H. Durney, "Upper Bound on Cell Size for Moment-Method Solutions", IEEE Trans. on Microvawe Theory and Tech., Vol. MTT-25, No. 10, Oct. 1977, pp. 831-832.

[40] H.C. Andrew and B.R. Hunt, "Digital Image Restoration", Prentice-Hall, New-Jersay, 1977.

[41] C.N. Dorny, "A vector Space Approach to Models and Optimization", Robert E. Krieger Publishing Company, Huntington, New-York, 1980.

[42] W.K. Pratt, F. Davarian, "Fast Computational Techniques for Pseudoinverse and Wiener Image Restoration", IEEE Trans. on Computers, Vol. C-26, no. 6, June 1977, pp. 571-579.

[43] R. Barakat and G. Newsam, "Numerically Stable Iterative Method for the Inversion of Wave-Front Aberrations from Measured Point-Spread-Function Data", Jour. Opt. Soc. Am., Vol. 70, No. 10, Oct. 1980, pp.1255-1263.

[44] J. Llacer, "Tomographic Image Reconstruction by Eigenvector Decomposition : Its Limitations and Areas of Applicability", IEEE Trans. on Medical Imaging, Vol. MI-1, No. 1, July 1982, pp. 34-42.

[45] K. Tanabe, "Projection Method for Solving a Singular System of Linear Equations and its Applications", Num. Math., Vol. 17, 1971, pp. 203-214.

[46] A. Bjorck and T. Eleving, "Accelerated Projection Methods for Computing Pseudoinverse Solutions of Systems of Linear Equations", BIT, Vol. 19, 1979, pp. 145-163.

[47] W.T. Stalling and T.L. Bouillon, "Computation of Pseudoinverse Matrices using Residue Arithmetic", SIAM Rev., Vol. 14, No. 1, Jan. 1972, pp. 152-163.

[48] E.E. Osborne, "Smallest Least-Square Solutions of Linear Equations", Jour. SIAM Num. Anal., Serie B, Vol. 2, No. 2, 1965, pp. 300-307.

[49] C. Muller, "Electromagnetic Radiation Patterns and Sources", IRE Trans. on Ant. and Propagation, Vol. AP-4, 1956, pp. 224-232.

[50] K. Feher, "Digital Communications : Microwave Application", Prentice-Hall,Englewood Cliffs, N.J., 1981, pp. 31-33.

[51] B.R. Frieden, "Statistical Models for the Image Restoration Problem", Comp. Graphics and Image Proc., Vol. 12, 1980, pp. 40-59.

[52] T.A. Nodes and N.C. Gallagher, "Median Filters : Some Modifications and Their Properties", IEEE Trans. on Acou. Speech and Signal Proc., Vol. ASSP-30, No. 5, Oct. 1982, pp. 739-746.

[53] M.A. Stuchly and S.S. Stuchly, "Dielectric Properties of Biological Substances-Tabulated", Journal of Microwave Power, Vol. 15, No. 1, 1980, pp. 19-26.

[54] D.K. Ghodgaonkar and O.P. Gandhi,"Estimation of Complex Permittivities of Inhomogeneous Biological Bodies", Fourth Bioelectromagnetics Society Meeting, Los Angeles, CA., June-July 1982.

[55] R.C. Gonzalez and P. Wintz, "Digital Image Processing", Addison-Wesley Publishing Company, 1977.

[56] C.C Johnson and A.W. Guy, "Nonionizing Electromagnetic Wave Effects in Biological Materials and Systems", Proc. of the IEEE, Vol. 60, No. 6, June 1972, pp. 692-696.

[57] P.W. Barber, O.P. Gandhi, M.J. Hagmann and I. Chartterjee, "Electromagnetic Absorption in a Multilayered Model of Man", IEEE Trans. on Biomedical Eng., Vol. BME-26, No. 7, July 1979, pp. 400-405.

[58] S.A Johnson, T. Yoon and J. Ra, "Inverse Scattering Solutions of Scalar Helmholtz Wave Equation by a Multiple Source Moment Method", Electronics Letters, Vol. 19, No. 4, Feb. 1983, pp. 130-132.